

USE OF SPATIALLY NON-UNIFORM ELECTRIC FIELDS FOR
CONTACT-FREE ASSEMBLY OF THREE-DIMENSIONAL
STRUCTURES FROM COLLOIDAL PARTICLES

by

JEFFERY A. WOOD

A thesis submitted to the
Department of Chemical Engineering
in conformity with the requirements for
the degree of Ph.D.

Queen's University
Kingston, Ontario, Canada
Submitted Jan. 2012

Copyright © Jeffery A. Wood, 2012

Abstract

The use of spatially non-uniform electric fields for the contact-free assembly of structures from colloidal building blocks is explored in this thesis. Specifically, the use of dielectrophoretic forces (electric field-induced dipole force) and electrohydrodynamic forces (electric field force on a fluid body) for assembling larger structures, with the goal of having both an electric-field defined shape as well as imparting order to the resulting structure. These types of colloidal structures have applications as photonic materials, sensing materials, templates for materials with enhanced functionality such as surface enhanced Raman spectroscopy or tissue engineering scaffolds, etc.

In this thesis, three specific research contributions to the use of non-uniform electric field driven colloidal assembly are described. The first relates to experimental work using dielectrophoretic and electrohydrodynamic forces (electroosmosis) to shape three-dimensional colloidal structures. Formation and stabilization of close-packed three-dimensional structures from colloidal silica was demonstrated, using gelation of pluronic F-127 to preserve medium structure against suspension evaporation. Stabilization of ordered structures was shown to be a significant challenge, with many of the conventional techniques for immobilizing colloidal crystals being ineffective. Secondly, the significance of electrohydrodynamic flows resulting from electric and particle concentration (entropic) gradients during the assembly process was demonstrated using numerical simulations based on a thermodynamic framework. These simulations, as well as experimental validation of assembly and the presence of fluid flows, showed that assuming equilibrium behavior (stationary fluid flow), a common assumption for most modelling work to date in these systems, is inappropriate at all but the most dilute concentration cases. Finally, the relevance of multiparticle effects on electric-field induced phase transitions of dielectric colloids was demonstrated. The effect of multiparticle/multiscattering effects on the suspension permittivity were accounted for using semi-empirical continuum permittivity formulations which have been previously shown

to describe a wide variety of solid packing structures, including face-centered cubic and other colloidal crystal structures. It was shown that multiparticle effects have a significant impact on both the coexistence (slow phase separation) and spinodal (fast phase separation) behavior of dielectric suspensions, which has not been demonstrated to date using a continuum framework.

Statement of Co-Authorship

This thesis contains materials which have been submitted for publication, as well as materials in preparation for publication.

Chapter 4: Wood, J. A. and Docoslis, A. Assembly of Colloidal Structures using AC Electrokinetic Forces from Non-Uniform Electric Fields. Manuscript in preparation for submission.

A version of Chapter 5 has been submitted for publication: Wood, J. A. and Docoslis, A. (2011). AC Electrokinetic Templating of Colloidal Particle Assemblies: Effect of Electrohydrodynamic Flows. Submitted: *Langmuir*, 1a-2011-049019

Chapter 6: Wood, J. A. and Docoslis, A. Electric-Field Induced Phase Transitions of Dielectric Colloids. Manuscript in Preparation for Submission.

All papers were co-authored and reviewed by Aris Docoslis as prepared, with all remaining work and manuscript preparation was carried out by the author of this thesis. Any additional contributions to this research (such as in the form of analytical expertise or materials fabrication for experiments) have been acknowledged in individual manuscripts.

Acknowledgments

Firstly, I would like to thank the seemingly limitless patience, support and guidance from my supervisor, Dr. Aris Docoslis. Through the years that we have pursued what Aris terms the "white whale" of my project, Aris has managed to be a constant source of technical support, scientific feedback and humour even through the most difficult times. I am indebted to him for the time and energy he has expended on this project and hope to live up to the potential that his supervision deserves.

The technical support of Mr. Charlie Cooney and Dr. Xiaohua Yan for SEM work/assistance is gratefully acknowledged. I would like to thank my fellow Docoslis student group members (Matthew, Mark, Eric, Ian and Jie) for all of their contributions of the course of my studies at Queen's, from research feedback to patience during what could be charitably described as slightly over-time group presentations was greatly helpful for my work. In particular, I would like to thank Mr. Mark Hoidas for all of the time he spent thinking about the (many) research questions I posed to him, some of them even related to what research we carry out in our research group. His willingness to read or try to read the volume of material I sent him was truly impressive. I would also like to thank Mr. Ian Swyer for all of the time he spent in the QFAB laboratory fabricating the microelectrodes that drive our research, his efforts were greatly appreciated. During the course of my studies at Queen's, I managed to meet quite a number of people who impacted my research and personal life. My fellow B27 office mates (in no particular order): Lars, Niels, Jordan, Mary, Ula, Nicky, Dan, Timothy, Stanley, Anil, Kevin, Jen, Callista, Jason and Raul (for a little while in that office at least). Other colleagues in the department, Nick, Paul-Philippe, (Little) Eric, Yong, Jonas, Allison, Adam, Mike and too many others to list. Thank you.

Finally, I have to thank the enormous contributions that my family made to help me reach

this goal. My brothers, Chris and Steven, are thanked for their seemingly relentless enthusiasm/optimism towards my work and patience at my various attempts to explain the nature of it. To my parents, Mike and Mary, I don't think words can really express the gratitude that I feel for all of your support during my years in Kingston. I hope that I am able to express that gratitude for years to come because it has made all the difference in the world for getting here successfully.

Contents

Abstract	i
Statement of Co-Authorship	iii
Acknowledgments	iv
Contents	vi
List of Tables	x
List of Figures	xi
List of Symbols	xiv
Chapter 1: Introduction	1
1.1 Research Contributions	3
Chapter 2: Theoretical Background	6
2.1 Electric Fields	6
2.1.1 Conductors and Dielectrics	6
2.1.2 Gauss' Law	7
2.1.3 Ohmic Heating	8
2.2 Dielectrophoretic Forces	8
2.2.1 Effective Dipole Moment Method	10
2.2.2 Effective Multipole Moment Expansion	13
2.2.3 Maxwell Stress Tensor Approach	14
2.2.4 Mutual Dielectrophoretic Forces	15
2.3 Electrohydrodynamics	16
2.3.1 Electroosmotic Flow	16

2.3.2	Electrothermal Flow	18
2.4	Brownian and Gravitational Forces	22
2.4.1	Brownian Forces	22
2.4.2	Gravitational Forces	23
2.5	Colloidal Interactions	24
2.5.1	Lifshitz-van der Waals Forces	24
2.5.2	Acid/Base Forces	26
2.5.3	Electrostatic Forces	29
2.6	Free Energy of Suspension Under Electric Field	33
Chapter 3:	Survey of Existing Literature	37
3.1	Ordered Structures and Colloidal Crystal Applications	37
3.1.1	Recent Colloidal Crystallization Advances	37
3.1.2	Photonic Bandgap Applications	38
3.1.3	Scaffolding Applications	40
3.1.4	SERS Applications	40
3.2	General Electrokinetic Papers	41
3.3	DEP Assembly	41
3.4	EHD Assembly	46
3.5	Current Modeling Work	48
Chapter 4:	Colloidal Assembly with AC Electrokinetics	51
4.1	Introduction	52
4.2	Materials and Methods	53
4.2.1	Colloids and Suspending Liquids	53
4.2.2	Microelectrodes	54
4.2.3	Microscopy	56
4.2.4	Zeta Potential Characterization	56

4.2.5	Stabilization Approaches	57
4.3	Results and discussion	60
4.3.1	DEP Assembly	61
4.3.2	DEP + EO Assembly	66
4.3.3	UV-Crosslinking of Structures	71
4.3.4	Stabilization with Biotin-Streptavidin Linkages	72
4.3.5	Gelation using Pluronic F-127 and PVA	73
4.3.6	Stabilization by Photopolymerization	79
4.4	Conclusions	81
Chapter 5:	AC Electrokinetic Templating of Assemblies	85
5.1	Introduction	86
5.2	Theoretical Background	90
5.3	Materials and Methods	94
5.3.1	Simulation Details	94
5.3.2	Experimental Details	95
5.4	Results and discussion	97
5.5	Conclusions	119
Chapter 6:	Electric Field Induced Phase Transitions	122
6.1	Introduction	123
6.2	Theoretical Background	124
6.3	Results and discussion	129
6.3.1	Suspension Permittivity and Derivatives	129
6.3.2	Critical Point for Silica-DMSO and Silica-iPrOH	133
6.3.3	Coexistence and Spinodal Lines for Silica-DMSO and Silica-iPrOH	139
6.4	Conclusions	142

Chapter 7: Summary and Future Recommendations	145
7.1 Summary	145
7.2 Future Recommendations	147
Bibliography	150
Appendix A: MATLAB Codes	164
A.1 Clausius-Mossotti Factor Calculation	164
A.2 Phase Equilibrium Model for Zero Electric Field	165
A.3 Permittivity and Derivative Fits	166
A.4 Coexistence and Spinodal Calculation with Electric Field	168
Appendix B: Finite Element Method	174

List of Tables

4.1	Particle Zeta Potential Measurements: Conditions	64
4.2	Particle Zeta Potential Measurements: Results	64
6.1	c_{cr} and E_{cr} for Silica-DMSO and Silica-iPrOH	137

List of Figures

2.1	Induced Dipoles	9
2.2	Dipole in a Spatially Non-Uniform Electric Field	11
2.3	AC Electroosmosis Mechanism	17
2.4	Double Layer Schematic	30
4.1	Schematic of Experimental Setup	55
4.2	Microelectrode Images	56
4.3	Surface Functionalization with Cinnamoyl Chloride	58
4.4	UV Crosslinking Mechanism	58
4.5	DEP Assembly of $1.5\mu\text{m}$ Silica in aq. pluronic F-127 (4wt%)	62
4.6	DEP Assembly of $2\mu\text{m}$ Silica in DMSO at 1MHz, $c_0=0.1$ vol.%, $0.5\mu\text{L}$ droplet	63
4.7	DEP Assembly of $2\mu\text{m}$ Silica in DMSO at 1MHz, $c_0=0.1$ vol.%, min. well volume	65
4.8	$1.98\mu\text{m}$ Latex Assembled at 20 V, 1 MHz	66
4.9	DEP Assembly of $2\mu\text{m}$ Silica in DMSO at 100 kHz, $c_0=0.1$ vol.%, $0.5\mu\text{L}$ droplet	68
4.10	DEP Assembly of $2\mu\text{m}$ Silica in DMSO at 100kHz, $c_0=0.1$ vol.%, min. well volume	69
4.11	DEP Assembly of $1.5\mu\text{m}$ PMMA in DMSO at 7V, 1kHz	71
4.12	Representative SEM images of $1.5\mu\text{m}$ cinnamoyl chloride functionalized silica DEP Assembly	72
4.13	SEM images of DEP Assembly of $1.5\mu\text{m}$ Silica in aq. pluronic F-127 (4wt%)	75
4.14	Zoomed SEM images of DEP Assembly of $1.5\mu\text{m}$ Silica in aq. pluronic F-127 (4wt%)	76
4.15	Microstructures for DEP Assembly of $1.5\mu\text{m}$ Silica in aq. pluronic F-127 (4wt%)	76
4.16	DEP Assembly of $1.5\mu\text{m}$ silica in aq. pluronic F-127 at 15V, 1MHz	77

4.17 SEM of DEP Assembly of $1\mu\text{m}$ silica in 95/5 (v/v) DMSO/ETPTA at 20V, 1MHz	81
5.1 Simulation Geometry	95
5.2 Top-Down View of $100\mu\text{m}$ gap spacing hyperbolic microelectrode chip	96
5.3 Visualization Planes for Simulation	98
5.4 Electric Field Strength at $V_{\text{applied}} = 20V$ peak-to-peak at $t=0$	99
5.5 Particle Volume Fractions with and without fluid flow for $d_P = 0.32\mu\text{m}$ in DMSO, $c_0 = 0.1$ vol. %	100
5.6 Particle Volume Fractions with and without fluid flow of $d_P = 0.32\mu\text{m}$ silica in DMSO, $c_0 = 1$ vol. %	101
5.7 Dielectrophoretic and Fluid Velocities (m/s) for $0.32\mu\text{m}$ silica in DMSO at 5V	103
5.8 Particle Volume Fractions with and without fluid flow of $d_P = 2\mu\text{m}$ silica in DMSO, $c_0 = 0.1$ vol.%	105
5.9 Particle Volume Fractions with and without fluid flow of $d_P = 2\mu\text{m}$ silica in DMSO, $c_0 = 1$ vol.%	106
5.10 Dielectrophoretic and Fluid Velocities (m/s) for $2\mu\text{m}$ silica in DMSO at 5V .	107
5.11 DEP and Fluid Velocities (m/s) as a function of Voltage for $0.32\mu\text{m}$ silica in DMSO	110
5.12 DEP and Fluid Velocities (m/s) as a function of Voltage for $2\mu\text{m}$ silica in DMSO	111
5.13 Electric Field Induced Assembly Profiles for $2\mu\text{m}$ silica in DMSO, $c_0 = 0.1$ vol.%	113
5.14 Electric Field Induced Assembly Profiles for $d_P = 1\mu\text{m}$ silica in H_2O , $c_0 = \text{vol.}$ 1%	114
5.15 Particle Volume Fractions, Non-equilibrium Case, for $d_P = 1\mu\text{m}$ silica in H_2O , $c_0 = 1$ vol.%	115
5.16 Electric Field Induced Assembly Profiles for $d_P = 1.5\mu\text{m}$ silica in H_2O - 3.8vol.% Pluronic F-127	116

5.17	SEM Images for $d_p = 1.5\mu\text{m}$ silica in H_2O -3.8vol.% Pluronic F127	117
5.18	Zoomed SEM of $1.5\mu\text{m}$ silica in H_2O with 3.8vol.% Pluronic F-127	118
6.1	Suspension Permittivity versus Volume Fraction for Silica-DMSO	131
6.2	Suspension Permittivity versus Volume Fraction for Silica-iPrOH	131
6.3	First Derivative of Suspension Permittivity with respect to Volume Fraction vs. Volume Fraction for Silica-DMSO	134
6.4	First Derivative of Suspension Permittivity with respect to Volume Fraction vs. Volume Fraction for Silica-iPrOH	134
6.5	Second Derivative of Suspension Permittivity with respect to Volume Fraction vs. Volume Fraction for Silica-DMSO	135
6.6	Second Derivative of Suspension Permittivity with respect to Volume Fraction vs. Volume Fraction for Silica-iPrOH	135
6.7	Third Derivative of Suspension Permittivity with respect to Volume Fraction vs. Volume Fraction for Silica-DMSO	136
6.8	Third Derivative of Suspension Permittivity with respect to Volume Fraction vs. Volume Fraction for Silica-iPrOH	136
6.9	Dimensionless Coexistence and Spinodal Lines for Silica-DMSO	141
6.10	Dimensionless Coexistence and Spinodal Lines for Silica-iPrOH	141

List of Symbols

a	Sihvola-Kong Parameter, [-]	128
A	Area [m^2].....	6
A	Hamaker Constant [J]	24
c	Volume (Packing) Fraction [-]	22
c_{cr}	Critical Volume Fraction for Phase Transition [-]	126
C	Capacitance [F].....	6
C_p	Heat Capacity [$\text{J}/(\text{kg}\cdot\text{K})$]	19
d	Gap Spacing [m].....	6
\vec{d}	Distance Vector [m]	10
d_p	Particle Diameter [m].....	10
D	Diffusion Coefficient [m^2/s]	22
e	Electron Charge [C]	31
E_{cr}	Critical Electric Field Strength for Phase Transition [V/m]	126
\vec{E}	Electric Field [V/m]	7
f	Henry's Function Correction Factor, [-]	57
f_0	Entropic Contributions for Hard Sphere Suspension, [-]	90
f_{cm}	Clausius-Mossotti Factor [-].....	12
F	Helmholtz Free Energy, [J]	125
\vec{F}_{DEP}	Dielectrophoretic Force [N]	11
\vec{g}	Acceleration due to Gravity Vector [m/s^2]	23
I	Electrical Current [A].....	6
k	Thermal Conductivity [$\text{W}/(\text{m}\cdot\text{K})$]	19
k_B	Boltzmann Constant [J/K]	22
K_e	Real Part of Clausius-Mossotti Factor [-]	35
n_b	Number of Ions in Bulk Solution [m^{-3}]	31
n^k	Surface Ion Density of kth Species [m^{-2}]	31

n^{th}	nth Generalized Multipole Moment [-]	13
p	Pressure [Pa]	21
\vec{p}	Dipole Moment Vector [C·m]	10
\vec{P}	Polarization Vector [C/m ²].....	7
r_p	Particle Radius [m]	12
Q	Electrical Charge [C]	6
T	Temperature [K]	19
\mathbf{T}	Maxwell Stress Tensor, MST [Pa].....	14
\vec{u}	Velocity Vector [m/s]	19
U_{slip}	Slip Velocity [m/s]	17
W	Electrical Energy Density, [J/m ³]	8
$\langle X \rangle$	Time-Averaged Value of X [-]	11
z^k	Valence of kth ionic species [-]	31
Z	Compressibility Factor [-]	22
α	Dimensionless Partial Derivative of ε with T [K ⁻¹]	20
β	Dimensionless Partial Derivative of σ with T [K ⁻¹]	20
γ	Interfacial Tension [J/m ²]	24
ε	Permittivity [F/m].....	6
ζ	Zeta Potential [V]	57
η	Viscosity [Pa·s]	22
κ	Debye Parameter [m ⁻¹]	32
λ	Characteristic Decay Length [m ⁻¹]	28
Λ	Stern Layer Factor [-]	17
μ	Viscosity [Pa·s]	17
μ_p	Chemical Potential [J/m ³]	34
$\vec{\xi}$	Gaussian-distributed random normal vector [-]	22

Π_p	Osmotic Pressure [Pa]	34
ρ	Electrical Charge Density [C/m ³]	7
ρ_m	Medium Density [kg/m ³]	19
σ	Electrical Conductivity [S/m]	6
τ	Characteristic Diffusion Time [s]	22
ϕ	Potential [V]	7
ψ	Volume Fraction of High Solids Phase [-]	36
Ψ	Surface Potential [V]	32
ω	Angular Frequency [Hz]	19
ℓ	Characteristic Thickness [m]	6
ℓ_c	Characteristic Field Length [m]	10
ΔG	Gibbs Free Energy of Interaction [J/m ²]	24
ΔV	Applied Electrical Potential [V]	6

Chapter 1: Introduction

The assembly of colloidal particles into ordered structures of larger characteristic dimensions (for example, on micron or larger scale) is a promising route for the creation of novel materials or imparting enhanced functionality to existing materials. These ordered materials are analogous in lattice structure to atomic crystals but are on a vastly larger scale, giving rise to very different properties. Applications of colloidal crystals range from as photonic materials (PBG), sensors, microelectronics, dye sensitized solar cells, scaffolds for tissue engineering applications to templates for surface-enhanced Raman spectroscopy [1–9]. Numerous techniques exist in order to facilitate the creation of ordered colloidal structures, ranging from self-assembly, template-assisted assembly (topological/geometric assisted assembly) and external field assisted assembly (gravitational, electric or magnetic fields) [10–14]. These techniques vary in complexity and in scale of assembly, that is in the final characteristic dimension of the useable device/material.

Self-assembled monolayers can be used in order to direct the placement of colloidal and other micro/nanoscale materials to specific substrate locations, such as carbon nanotubes or gold nanoparticles [12]. Template-assisted assembly can be considered as complementary to all the other listed techniques. For example, self-assembly of colloidal structures can be achieved by providing physical confinement for colloidal particles in order to force the particles to form an ordered structure within the confining geometry. The templated structures can then be used as templates to create larger structures, for example the formation of three-dimensional porous structures based on a 2d colloidal crystal array [1]. Sedimentation/gravitational control is highly sensitive to the size of particles, as the buoyancy force is proportional to particle volume, which scales poorly with size [15] and can take weeks to accomplish complete sedimentation of submicron particles [1]. However, the technique is often used to create 3d structures of larger colloidal particles ($> 0.5\mu\text{m}$) which have a high density difference between solid and medium (ex. silica-water), although there is little control of

the surface morphology or number of particle layers [1]. Electric and magnetic fields offer more control forces versus relying primarily on gravity, however, magnetic fields require very strong magnets/electromagnets as well as the use of magnetic materials which limits their application. For electric fields, high electric field intensities possible using microfabrication techniques (i.e. small characteristic dimensions) and application requires only a difference between particle and medium electrical properties [16].

Electric-field assisted techniques are quite useful for the rapid assembly of materials with characteristic dimensions many orders of magnitude larger than the dimensions of the assembly blocks (i.e particles). This technique is controllable through many parameters, including applied voltage, frequency (AC fields), electrode geometry and medium physical properties (dielectric constant, viscosity, conductivity, etc.) [16–18]. The use of electric fields for control forces is also complementary with gravitational or geometric templating of structures. Application of an electric field on a colloidal suspension will induce an electrical dipole (and higher order moments) around particles as long as the medium electrical properties vary from that of the suspended particle. A non-uniform electric field will then give rise to a net translational force on particles, arising from action of the electric field on this induced dipole. This phenomena is known as dielectrophoresis. Similarly, a non-uniform electric field will impose a volume force on the suspending medium which can give rise to fluid flows. These types of fluid flows are referred to as electrohydrodynamic flows. These two types of phenomena are examples of a larger class of control forces, known as electrokinetic forces. AC electrokinetic forces have been widely used to construct structures of varying size, order and geometry from colloidal building blocks, ranging from two-dimensional colloidal crystals to larger three dimensional close packed structures [19, 20]. To date, there has been limited progress towards electric-field assembled three-dimensional ordered colloidal structures, that is structures with a distinct shape, size and order arising from an applied electric field.

It was the goal of this thesis research to examine the use of electric-field assisted assembly for creation of materials with novel properties and potential anisotropies. The focus is on studying the use of AC electrokinetic forces (dielectrophoresis and electroosmosis) resulting from non-uniform electric fields for constructing structures of varying size, order and geometry from colloidal building blocks. This was accomplished experimentally, through using non-uniform electric fields for assembling various colloidal suspensions into larger structures, as well as theoretically, through the use of simulations of the assembly process. The contributions to the existing knowledge on non-uniform electric field driven colloidal assembly are summarized in the next section.

1.1 Research Contributions

Three major contributions to this research area are outlined in this thesis, found in Chapters 4, 5 and 6 respectively.

Chapter 4: Assembly of Colloidal Structures using AC Electrokinetic Forces from Non-Uniform Electric Fields

The first contribution relates to experimental work using spatially non-uniform electric fields generated with quadrupolar planar microelectrodes for assembling colloidal particles in suspension into larger structures. A number of particle-medium combinations were studied for different properties, and a large amount of shapes and sizes of structures were possible using a single microelectrode geometry. Near-refractive index matching of suspensions was found to encourage ordered-type structures. It was also found that medium evaporation was highly destructive to any formed assembly and consequently a stabilization method was required. Out of the methods studied, gelation using pluronic F-127 was found to be the most effective at preserving the overall shape and size of an assembly but also inhibited formation of any

kind of ordered structure. This experimental work also demonstrated that a number of conventional techniques for immobilizing colloidal crystal arrays were ineffective for preserving assemblies of this nature.

Chapter 5: AC Electrokinetic Templating of Colloidal Particle Assemblies: Effect of Electrohydrodynamic Flows

The second is simulation work based on a thermodynamic framework for describing non-uniform electric field driven assembly of structures from colloidal particles. In this work the-called “equilibrium” case, where fluid flow is stationary ($\vec{u}_f = 0$), was compared to the “non-equilibrium” case, where the fluid is non-stationary ($\vec{u}_f \neq 0$). The equilibrium state is often employed when describing assembly processes but its validity outside of the very dilute particle case has not been explored. Simulations for colloids of varying size and initial concentration over a range of voltages showed that excepting the most dilute cases, the steady-state equilibrium solution deviates significantly from the non-equilibrium solution for particle volume fraction. This occurred due to the large impact of fluid flows arising from electrical and entropic forces. For all but the largest particles at the most dilute particle concentrations, the dielectrophoretic force was dominated by the electrohydrodynamic flows in the system. Predictions of particle volume fraction based on a 2d approximation were shown to be in qualitative agreement with experimental results. These types of fluid flows have been experimentally demonstrated previously, but to date had not been explained satisfactorily. This work clearly illustrates the importance of accounting for the fluid flows which will result for colloidal suspensions under non-uniform electric fields.

Chapter 6: Electric-Field Induced Phase Transitions of Dielectric Colloids

The third contribution was in examining the influence of multiscattering effects on electric

field induced phase transitions of dielectric colloids. These effects were accounted for using effective permittivity models which were capable of describing different solid packings (RCP, FCC, BCC) and high concentration region effects on permittivity. These effective permittivity models are continuum based, allowing for straightforward comparison to results from assuming Maxwell-Garnett permittivity. Model suspensions of silica-DMSO and silica-iPrOH were used as test cases to examine the effect of changing medium permittivity as well as particle-medium contrast. It was found that for larger dielectric contrast between medium and particle accounting for multiscattering effects had a larger impact and caused a significant shift in the phase diagrams. The effect on the phase diagrams also depended on the curvature of permittivity vs. volume fraction. This work represents a preliminary accounting for multiscattering effects, the case of conductive/lossy suspensions needs to be explored but clearly indicated that severe deviations from Maxwell-Garnett type behavior exist for both coexistence and the spinodal lines of suspension under an electric field. This has large and potentially useful implications in systems of physical interest, such as electrorheological fluids and structures of assemblies resulting from non-uniform electric fields.

Chapter 2: Theoretical Background

2.1 Electric Fields

2.1.1 Conductors and Dielectrics

The response of materials to electrical potentials/fields can be broken into two categories: conductors and dielectrics. Conductors are materials with an excess of free charge, which can move throughout the material freely under the influence of an external applied potential. In metals, free charge is the result of electrons with high mobility, and in aqueous electrolytes, the free charge is the caused by motion of dissociated ions. The flow of free charge is referred to as current and the process is known as electrical conduction. The degree of flow is determined by the electrical conductivity/resistivity of the material. Low conductivity (high resistivity) means the material is a poor conductor, high conductivity (low resistivity) means it is a good conductor. The relationship between the applied potential, ΔV and the current flow, I , through a material with a linear response for conductivity, σ , and thickness ℓ is given by Ohm's Law [21]:

$$\Delta V = \frac{I}{\sigma \ell} \quad (2.1)$$

Dielectrics (or insulators) are materials which are either devoid of free charges or contain charges with limited mobility. Charges within the material are able to reposition at the atomic/molecular scale, allowing dipoles to re-orient under the influence of an applied potential (polarize). The ability of a dielectric to accumulate charges at the outer surface is termed capacitance, C and this is related to the permittivity of the material, ε , by the relationship $C = \varepsilon A/d$ where A is the area and d is distance over which the potential is applied, so that the relationship between the applied potential and the charges, Q , which accumulate on the dielectric surfaces is [21]:

$$\Delta V = \frac{Q}{C} = \frac{Q}{\varepsilon A/d} \quad (2.2)$$

2.1.2 Gauss' Law

For an inhomogeneous dielectric there is a non-zero volume charge density arising from the polarization of the medium. Starting from Gauss' Law we can derive a final expression which determines the potential profile within the medium, with no external charges¹ [22]:

$$\nabla \cdot \vec{E} = \rho \quad (2.3)$$

$$\rho = -\nabla \cdot \vec{P} \quad (2.4)$$

$$\vec{P} = \varepsilon_0(\varepsilon_m - 1)\vec{E} \quad (2.5)$$

where \vec{E} is the electric field, ρ is the charge density, \vec{P} is the polarization vector of the medium, ε_m is the relative permittivity of the medium and ε_0 is the permittivity of vacuum.

Simplifying by making use of divergence identities for gradients², one obtains the final simplified form of Gauss' law:

$$\nabla \cdot (\varepsilon_m \vec{E}) = 0 \quad (2.6)$$

The electric field can also be defined in terms of the gradient of a scalar quantity, the potential ϕ , as follows [22]:

$$\vec{E} = -\nabla \phi \quad (2.7)$$

Substituting in eqn. 2.7 into eqn. 2.6, one obtains a final form for calculating the electric potential profile within a spatially inhomogeneous dielectric with a linear electric induction³

¹ There are induced charges from the polarization of the medium, which is what ρ refers to, but the equation is generally re-written in terms of permittivity so that this term is not explicitly calculated [22]

² $\nabla \cdot a\vec{b} = \nabla a \cdot \vec{b} + a\nabla \cdot \vec{b}$ [23]

³ strictly speaking, \vec{D} , the electric induction, and \vec{E} do not vanish simultaneously when the medium has spatially inhomogeneous properties. This was the assumption implicit in the derivation of the final form of Gauss' law. However, the effect of the inhomogeneous terms is negligible. See [22] for details

[22]:

$$\nabla \cdot (\varepsilon_m \nabla \phi) = 0 \quad (2.8)$$

This equation reduces to Laplace's equation for a spatially homogeneous dielectric (constant ε_m).

2.1.3 Ohmic Heating

The application of an electric field to a conducting medium will cause current to flow, with Ohm's law being a linear response between current and electric field. This current will also cause a temperature rise in the medium. If the field is spatially non-uniform, this will mean that a temperature gradient will also arise. This temperature gradient is significant in that it will cause gradients in electrical properties and give rise to additional forces on the medium, as will be seen in section 2.3.2 [16].

The power density, W , from application of the electric field (for a conductor that follows Ohm's law) is given by:

$$W = \sigma |\vec{E}|^2 \quad (2.9)$$

Organic materials and distilled/deionized water have negligible temperature rises from Ohmic heating due to low conductivity, however, aqueous electrolytes can have significant temperature rises.

2.2 Dielectrophoretic Forces

In the presence of an electric field, a polarizable particle will experience an induced dipole. In a non-uniform field, this will result in a net translational force on the particle as the force on either side of the pole is not equal. The resulting force on the particle is termed the *dielectrophoretic force* and the motion due to this force is known as *dielectrophoresis* [24].

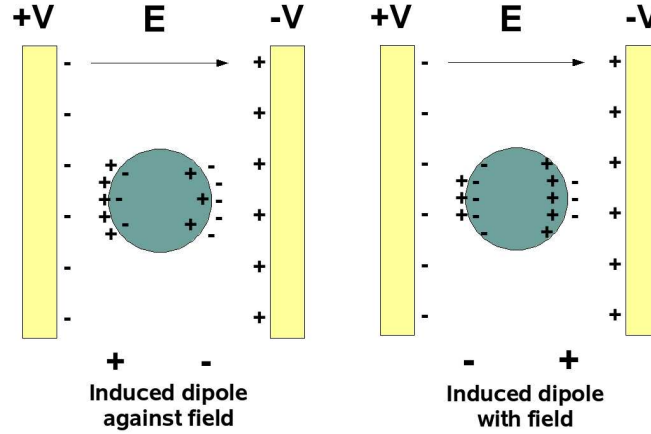


Figure 2.1: Induced Dipoles

a) $\varepsilon_p < \varepsilon_m$, b) $\varepsilon_p > \varepsilon_m$ Adapted from [16]

The application of an electric field will cause charges to accumulate at either side of the interface between a particle and a medium. The degree of charge building up depends on the polarizability of the medium, which is a measure of both the ability of a material to respond to a field (conductive response) and the ability to produce charges at an interface (dielectric response). If a particle has a much lower polarizability than the suspending medium, there will be a larger amount of charges on the medium side of the particle-medium interface, as is the case in Fig. 2.1a). This gives rise to an induced dipole across the particle, which is aligned opposite to the electric field. If the particle has a much larger polarizability than the medium suspending it, there will be a larger amount of charges on the particle side of the particle-medium interface, as is the case in Fig. 2.1b). This gives rise to an induced dipole across the particle, which is aligned with the electric field. If the particle and medium are equally polarizable, there will be no induced dipole [16].

For a particle with an induced dipole, if the applied electric field is uniform there will be an equal and opposing force on each pole and there will be no net motion of the particle. If the

field is non-uniform one side of the particle will experience a larger force than the other and there will be a net translational motion. This motion is termed dielectrophoresis (DEP), the *di* corresponding to dipole. DEP can exist for both DC and AC electric fields, the only requirement is spatially non-uniform electric fields [16].

If the particle is less polarizable than the medium, the electric field within the particle is high, the external field lines will bend around the particle as if it was an insulator and the particle will move towards regions of electric field minima. This case, which corresponds to Fig. 2.1a), is known as negative dielectrophoresis (negative DEP). If a particle is much more polarizable than the medium, than the electric field within the particle is nearly zero, the external field lines will bend towards the particle and the particle will move towards regions of electric field maxima (i.e. electrode edges). This case, which corresponds to Fig. 2.1b), is known as positive dielectrophoresis (positive DEP). The dielectrophoretic force is proportional to particle volume, meaning that for colloidal particles ($d_p < 1\mu\text{m}$) a characteristic field strength on the order of 10^6 V/m or larger is needed to move them [16]. This is achieved using reasonably low voltages by making use of electrodes with characteristic gap spacings on the order of microns or smaller.

2.2.1 Effective Dipole Moment Method

The dipole moment of a particle can be written as the magnitude of charge at the pole (or effective magnitude) (Q) multiplied by distance vector between the poles (\vec{d}), resulting in $\vec{p} = Q\vec{d}$. A schematic of a dipole in a spatially non-uniform electric field is given in Fig. 2.2 [25]. As long as $\vec{E}(\vec{r} + \vec{d}) \neq \vec{E}(\vec{r})$, there will be a net Coulombic force on the particle.

In order to develop the expression for the dielectrophoretic force on a spherical particle one can use a Taylor series expansion on the Coulomb force acting on the dipole shown in Fig. 2.2. After neglecting higher order terms (valid if $|\vec{d}| \ll \ell_c$), the final expression for the DEP

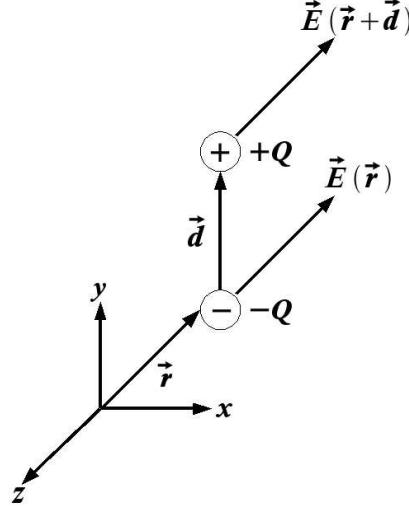


Figure 2.2: Dipole in a Spatially Non-Uniform Electric Field

Adapted from [25]

force is derived as⁴ [25]:

$$\vec{F}_{DEP} = (\vec{p} \cdot \nabla) \vec{E} \quad (2.10)$$

From this expression, it is clear there is only a net force on the particle if there is a spatially varying electric field (non-uniform). For spherical particles, the effective dipole moment can be written as [25]:

$$\vec{p} = 4\pi\epsilon_m \left(\frac{\tilde{\epsilon}_p - \tilde{\epsilon}_m}{\tilde{\epsilon}_p + 2\tilde{\epsilon}_m} \right) r_p^3 \vec{E} \quad (2.11)$$

In eqn. 2.11, $\tilde{\epsilon}$ refers to the complex permittivity of either the particle (p) or medium (m). The complex permittivity of a material is defined as $\tilde{\epsilon} = \epsilon - i\sigma/\omega$, and is a measure of the “effective” capacitance of a lossy dielectric. Substituting eqn. 2.11) into eqn. 2.10) and time-averaging, one arrives at:

$$\langle \vec{F}_{DEP} \rangle = 2\pi\epsilon_m r_p^3 \text{Re} \left[\frac{\tilde{\epsilon}_p - \tilde{\epsilon}_m}{\tilde{\epsilon}_p + 2\tilde{\epsilon}_m} \right] \nabla |\vec{E}_{rms}|^2 \quad (2.12)$$

⁴ See [25] for details

The expression $\frac{\tilde{\epsilon}_p - \tilde{\epsilon}_m}{\tilde{\epsilon}_p + 2\tilde{\epsilon}_m}$ is known as the Clausius-Mossotti factor, f_{cm} . This factor describes the frequency dependent behaviour of polarization. At low frequencies polarization depends solely on conductivity and at high frequencies polarization depends solely on permittivity. This frequency-tunable response leads to the ability to shift from positive DEP to negative DEP and vice versa or change the intensity of the DEP force purely by changing the frequency of the applied electric field. An equivalent Clausius-Mossotti expression for ellipsoids, which is of relevance when considering nanotubes or other cylindrical shapes, is also available [16, 25]. For nanocolloids the validity of using the Clausius-Mossotti expression has been debated as the ratio of surface to bulk atoms is such that the material properties may not be continuous but in the absence of an alternative approach, the Clausius-Mossotti approach remains the best way to deal with the polarizability of a material within a medium [26].

For spherical particles with a characteristic dimension much less than that of the characteristic dimension of the electric field ($d_p \ll \ell_c$), the dipole approximation works well. This is to be expected from the nature of developing a first order Taylor series in order to describe the dielectrophoretic force. For rod shape particles (particular when close to electrodes) or spheres close in size to the characteristic field dimension, then the effective multipole method or Maxwell Stress Tensor approach should be used as the dipole approximation has been shown to give inaccurate force predictions [27]. In most cases for this research, the characteristic field dimension will be on the order of 100 μm , meaning that the $d_p \ll \ell_c$ and for spherical colloids the dipole approximation will be suitable to estimate the DEP force on an isolated particle.

2.2.2 Effective Multipole Moment Expansion

Calculation of the force can also be accomplished using higher order moments than just the dipole, this approach was explored in depth by Jones and Washizu (1996) [28]. The multipole moments were formulated in terms of dyadic tensors and expanded into generalized equations for each order of moment (dipole, quadrupole, octupole, etc.). Simplified expressions in terms of vector indices are provided as well, which are easier to implement for calculations. The generalized multipole moment expression for the force on the n^{th} moment gives the following equation [28, 29]:

$$\vec{F}^{(n)} = \frac{\mathbf{p}^{(n)}[\cdot]^{(n)}(\nabla)^{(n)}\vec{E}}{n!} \quad (2.13)$$

The n^{th} moment induced on a spherical particle from a sinusoidal AC field is given by:

$$\mathbf{p}^{(n)} = \frac{4\pi\epsilon_m R^{2n+1}n}{(2n-1)!!} \tilde{K}^{(n)}(\nabla)^{(n-1)}\vec{E}e^{i\omega t} \quad (2.14)$$

with $\tilde{K}^{(n)}$ being the n^{th} equivalent Clausius-Mossotti factor, calculated as:

$$\tilde{K}^{(n)} = \frac{\tilde{\epsilon}_p - \tilde{\epsilon}_m}{n\tilde{\epsilon}_p + (n+1)\tilde{\epsilon}_m} \quad (2.15)$$

Substitution of equation 2.14 into 2.13 and time-averaging results in the expressions for each component of the total DEP force⁵:

$$\langle \vec{F}^{(n)} \rangle = \frac{2\pi\epsilon_m r_p^{2n+1}}{(n-1)!(2n-1)!!} \text{Re} \left[\tilde{K}^{(n)}(\nabla)^{(n-1)}\vec{E}_{rms}[\cdot]^{(n)}(\nabla)^{(n)}\vec{E}_{rms}^* \right] \quad (2.16)$$

This equation is the general expression for the calculation of the electric field force on the particle from the n^{th} moment (similar expressions exist for the torque and can also be found in [28]). Simpler expressions that reduce the calculations to vector indices (easier to implement calculations) can also be obtained. For a spherical particle, the expressions for the dipole

⁵ $(2n-1)!! = (2n-1)(2n-3)(2n-5)\cdots(5)(3)(1)$ [29]

(n=1), quadrupole (n=2) and octupole (n=3) contributions to the DEP force⁶ are:

$$\langle \vec{F}^{(1)} \rangle = 2\pi\epsilon_m r_p^3 \text{Re} \left[\tilde{K}^{(1)} E_{m,rms} \frac{\partial}{\partial x_m} E_{i,rms}^* \right] \quad (2.17)$$

$$\langle \vec{F}^{(2)} \rangle = \frac{2}{3}\pi\epsilon_m r_p^5 \text{Re} \left[\tilde{K}^{(2)} \frac{\partial E_{n,rms}}{\partial x_m} \frac{\partial^2 E_{i,rms}^*}{\partial x_n \partial x_m} \right] \quad (2.18)$$

$$\langle \vec{F}^{(3)} \rangle = \frac{1}{15}\pi\epsilon_m r_p^7 \text{Re} \left[\tilde{K}^{(3)} \frac{\partial^2 E_{n,rms}}{\partial x_l \partial x_m} \frac{\partial^3 E_{i,rms}^*}{\partial x_n \partial x_m \partial x_l} \right] \quad (2.19)$$

The equation form for higher order moments can be deduced from these expressions, with increasing order of sums⁷.

2.2.3 Maxwell Stress Tensor Approach

The force acting on a body suspended in a dielectric medium can also be evaluated using the Maxwell Stress Tensor (MST). The MST, \mathbf{T} , for a body within a dielectric medium is given by [21]:

$$\mathbf{T} = \epsilon \vec{E} \vec{E} - \frac{1}{2} \epsilon (\vec{E} \cdot \vec{E}) \mathbf{I} \quad (2.20)$$

The force is determined by integrating the stress-tensor over the surface area of the body (or divergence over the volume):

$$\vec{F}_{MST} = \int_V (\nabla \cdot \mathbf{T}) dV = \int_S (\vec{n} \cdot \mathbf{T}) dS = \int_S (\mathbf{T} \cdot \vec{n}) dS \quad (2.21)$$

⁶ The *di-* in dielectrophoretic force technically refers to the force from the dipole but often in papers the force of all moments accounted for or calculated by the MST method is referred to as the DEP force

⁷ All terms are expressed according to the Einstein summation convention, meaning that sums are taken over repeated indices [28]

Switching the order of the normal and tensor in eqn. 2.21 is possible as the stress tensor is symmetric. Now, substituting in eqn. 2.20 and time-averaging, we arrive at a final time-averaged value of the electric field force:

$$\langle \vec{F}_{MST} \rangle = \int_S \left(\left[\epsilon \vec{E}_{rms} \vec{E}_{rms} - \frac{1}{2} \epsilon (\vec{E}_{rms} \cdot \vec{E}_{rms}) \mathbf{I} \right] \cdot \vec{n} \right) dS \quad (2.22)$$

The Maxwell Stress Tensor approach is the most rigorous approach to calculate the electric force on a suspended body in a dielectric/conducting medium. This rigour comes with increased complexity in numerical evaluation as the electric field profile accounting for the particle perturbation must be solved but for the case of non-spherical particles, it has been shown to be necessary to obtain accurate results in many cases [27].

2.2.4 Mutual Dielectrophoretic Forces

The induced dipole on a particle from the presence of an electric field can be acted upon by the external electric field and if this field is spatially non-uniform the resulting particle motion is termed dielectrophoresis. An induced dipole can also interact with another induced dipole and this interaction force is termed mutual dielectrophoresis (mutual DEP).

The following expression for the mutual DEP force between two dipoles can be derived using the point dipole approximation [30]:

$$\vec{F}_{mutual\ DEP} = \frac{1}{4\pi\epsilon_m} \frac{3}{r^5} [\vec{r}_{ij}(\vec{p}_i \cdot \vec{p}_j) + (\vec{r}_{ij} \cdot \vec{p}_j)\vec{p}_i - \frac{5}{r^2} \vec{r}_{ij}(\vec{p}_i \cdot \vec{r}_{ij})(\vec{p}_j \cdot \vec{r}_{ij})] \quad (2.23)$$

In eqn. 2.23 \vec{r}_{ij} is the relative distance vector between particle i and j ($\vec{r}_{ij} = \vec{r}_i - \vec{r}_j$) where \vec{r} represents the position vector. \vec{p}_i is the dipole moment vector of particle i , given by

equation 2.11 in section 2.2.1 for a spherical particle under the point dipole approximation⁸. This expression has been put to use in a number of DEP applications involving chaining of particles together by the mutual DEP force [30–32]. The inverse proportionality to distance between two particles is of the 4th power, indicating that the mutual DEP effect is negligible beyond a few particle diameters but can be quite large for small intraparticle distances. Jones (1995) determined that for calculations of mutual DEP forces between particle chains and clusters, the $N = 2$ (i.e. two-particle interaction) case deviated by at most a factor of 2 from the experimentally determined value [25]. This is an indication of why this simplified approach to describe the mutual DEP effect has been successful in previously performed studies.

2.3 Electrohydrodynamics

Electrohydrodynamics is the study of fluid behaviour under the influence of electric fields. In terms of AC electric fields there are two effects of interest, electroosmotic flow and electrothermal flow. Both of these effects can be used to manipulate colloidal-size particles and in the case of nanometer scale particles the flow effects can be significantly stronger than that of DEP.

2.3.1 Electroosmotic Flow

AC electroosmotic flow is the flow induced by the action of the electric field on the ionic double layer within the medium, which forms above the electrodes⁹ [24]. The charge of the ions above the electrodes will flip with the applied field, meaning that there will still be a

⁸ Although the mutual DEP expression in eqn. 2.23 is derived for a point dipole approximation, the dipole moment vector can be calculated using the effective multipole moment if a higher degree of accuracy is desired

⁹ This varies from DC electroosmosis where the primary response is due to surface charges from the substrate

net time-averaged force. More details on the double layer are provided in section 2.5.3. The mechanism behind AC electroosmosis is illustrated in Figure 2.3 [17]

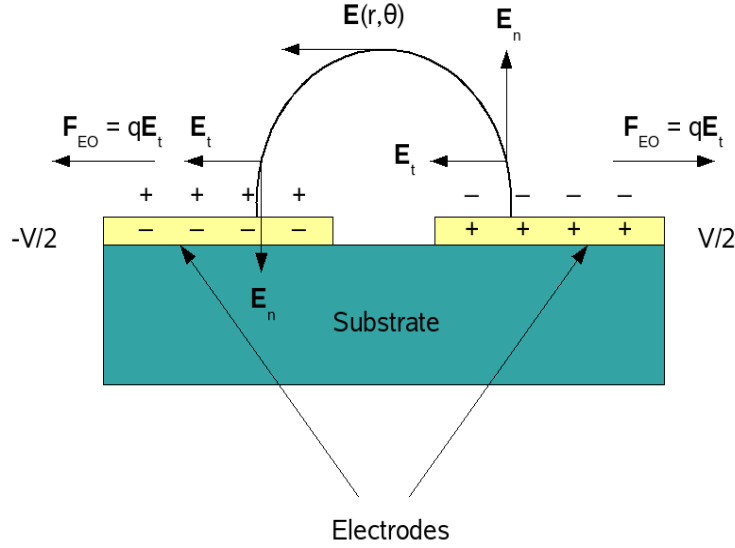


Figure 2.3: AC Electroosmosis Mechanism
Adapted from [17]

Ordinarily at a boundary, the velocity will be zero (no-slip condition) however, in the case with a double layer the application of an electric field will cause the charges in the double layer to move and pull the fluid along tangentially [16]. An expression for the time-averaged electroosmotic velocity can be given by [18]:

$$\langle U_{slip} \rangle = -\frac{1}{4} \frac{\varepsilon_m}{\mu} \Lambda \frac{\partial}{\partial l} |\Delta \phi_{DL}|^2 \quad (2.24)$$

In eqn. 2.24, μ is the viscosity, Λ is a factor relating to the Stern layer (see section 2.5.3) which is generally agreed upon as being $1/4$ and $\Delta \phi_{DL}$ is the potential drop across the double layer. In order to solve this equation, an expression for $|\Delta \phi_{DL}|^2$ is required. The double layer can be modelled as a distributed capacitor, with $\phi_{DL} - \frac{\sigma}{i\omega C} \frac{\partial \phi_{DL}}{\partial n}$ [18]. For very low frequencies, the applied voltage drops primarily across the double layer, the electric field outside of the

double layer is very small and there is then a very small electroosmotic slip velocity. For very high frequencies, the applied voltage is dropped primarily across the electrolyte and the surface charge of the double layer is small, resulting in a very small or negligible electroosmotic velocity [33]. The effective result is that AC electroosmosis is a relevant effect in a frequency range between 10 Hz and 100 kHz and becomes negligible outside of this frequency range [16]

Using eqn. 2.24 to determine the electroosmotic velocity eliminates the need to thoroughly model the double layer effects. The alternative to this approach is to solve the Poisson-Boltzmann equation (eqn. 2.52 in section 2.5.3) in order to determine the free charge density. Then determining the electric field force on the fluid due to this free charge density in the double layer, one can determine the electroosmotic velocity profile [21]. This adds a great deal to the complexity of equations being solved and may not be practical for more complicated simulations involving MD approaches or suspension free energy but a comparison of the electroosmotic velocity calculated using eqn. 2.24 and this approach for a particle free system will be carried out to determine if there is sufficient cause to use it when dealing with EO phenomena in multi-particle simulations.

AC electroosmosis is a very useful technique for microfluidic applications. It is the most common choice for pumping of materials in microfluidic devices, since it involves no moving parts [34]. Velocities on the order of mm/s can be achieved using this technique, which is quite significant considering the μm scale of these devices, and numerous practical examples exist within the literature [35–38].

2.3.2 Electrothermal Flow

The application of an electric potential across a conducting medium will cause the generation of heat due to flow of current (Ohmic heating) (see section 2.1.3). In the case of non-uniform electric fields, this heating causes a temperature gradient. Since the physical properties of

the medium are generally temperature dependent, this means gradient will arise in these properties as well. Using microelectrodes means that the gradients generated can be quite large and the impact of these gradients is profound. Temperature gradients will cause gradients in permittivity and conductivity of the fluid medium. Gradients in these parameters will cause variations in the charge density throughout the medium, resulting in an electric force on the fluid. To derive the equation for the electric force due to ohmic heating, an energy balance for the medium is the first step. Writing the energy balance for an incompressible liquid [23]:

$$\rho_m C_p \frac{\partial T}{\partial t} + \rho_m C_p \vec{u} \cdot \nabla T = \nabla(k \cdot \nabla T) + \sigma |\vec{E}|^2 \quad (2.25)$$

Based on order of magnitude analysis, the convective component of heat transfer is generally negligible, since for typical dimensions/velocities $\frac{\rho_m C_p u \ell}{k} \ll 1$. In addition, due to the identity $\frac{\partial}{\partial t} = i\omega$, at frequencies greater than 1 kHz the medium will essentially be in instantaneous equilibrium with the field (i.e. steady-state operation) [17].

This simplifies the equation to:

$$\nabla(k \cdot \nabla T) + \sigma |\vec{E}|^2 = 0$$

which can be converted to a time-averaged value for temperature based on a sinusoidal applied potential¹⁰:

$$\nabla(k \cdot \nabla T) + \sigma |\vec{E}_{rms}|^2 = 0 \quad (2.26)$$

With the temperature and potential spatial profile known, the electrothermal force can be

¹⁰ In [17] and many other references for calculating temperature rise in DEP/EHD systems the thermal conductivity is taken as a constant and removed from the gradient operator, which is only valid for small temperature rises generally as gradients in thermal conductivity can be significant

calculated. The electrical body force generally on a medium is given by [17]:

$$\vec{f}_{elec} = \rho \vec{E} - \frac{1}{2} |\vec{E}|^2 \nabla \varepsilon + \frac{1}{2} \nabla \left(\rho_m \left(\frac{\partial \varepsilon}{\partial \rho_m} \right)_T |\vec{E}|^2 \right) \quad (2.27)$$

The first term is the Coulomb force, the second is the dielectric force and the last term is the electrorestriction pressure. For incompressible fluids, the contribution of electrorestriction pressure is zero. The expression for this force can be developed using the perturbation of the electric field due to the gradients of permittivity and conductivity, $\vec{E} = \vec{E}_0 + \vec{E}_1$ with \vec{E}_1 being the perturbation field and $|\vec{E}_1| \ll |\vec{E}_0|$. Starting with Gauss' Law (see equation 2.6 in section 2.1.2) for an inhomogeneous medium^{11, 12}, and noting that $\nabla \cdot \vec{E}_0 \simeq 0$ [17] an expression for the charge density, ρ , in terms of the divergence of the perturbation field and gradients of permittivity and conductivity can be developed. In order to eliminate the perturbation field term in the charge density in favour of quantities in permittivity and conductivity, the charge conservation equation can be used and much as for the energy balance the convection current is neglected and conduction (from Ohm's law) dominates. After numerous substitutions and simplifications (see [23] for details) the time-averaged electric body force on the fluid is arrived at as [23]:

$$\langle \vec{f}_{elec} \rangle = \text{Re} \left[\left(\frac{(\sigma \nabla \varepsilon - \varepsilon \nabla \sigma) \cdot \vec{E}_{0,rms}}{\sigma + i\omega \varepsilon} \right) \vec{E}_{0,rms}^* - \frac{1}{2} |\vec{E}_{0,rms}|^2 \nabla \varepsilon \right] \quad (2.28)$$

Finally, if the change of conductivity and permittivity with temperature is known, the entire equation can be posed in terms of temperature gradients by re-writing gradients in permittivity and conductivity as gradients in temperature $\nabla \varepsilon = \alpha \nabla T$ and $\nabla \sigma = \beta \nabla T$, with $\alpha = \frac{1}{\varepsilon} \frac{\partial \varepsilon}{\partial T}$ and $\beta = \frac{1}{\sigma} \frac{\partial \sigma}{\partial T}$. This results in the final equation for the electric body force due to

¹¹ $\nabla \cdot a\vec{b} = \nabla a \cdot \vec{b} + a \nabla \cdot \vec{b}$ and $\nabla \cdot (\vec{a} + \vec{b}) = \nabla \cdot \vec{a} + \nabla \cdot \vec{b}$ [23]

¹² Note that ρ is taken as non-zero here as we are interested in calculating the induced charge density due to the perturbation, if the equation is written for \vec{E}_0 then the form will be identical to eqn. 2.6)

thermal effects [24]:

$$\langle \vec{f}_{elec} \rangle = \text{Re} \left[\frac{(\alpha - \beta)}{\sigma + i\omega\varepsilon} (\nabla T \cdot \vec{E}_{0,rms}) \vec{E}_{0,rms}^* - \frac{1}{2} \varepsilon \alpha |\vec{E}_{0,rms}|^2 \nabla T \right] \quad (2.29)$$

The first term of the electrothermal force equation is the Coulomb force, which dominates at low frequencies, and the second term is the dielectric force, which dominates at high frequencies. These forces are generally in opposite directions, with the low frequency limit of the Coulomb force being approximately 10 times larger than the high frequency limit of the dielectric force [24]. AC electrothermal flow becomes the dominant electrohydrodynamic flow at frequencies above 100 kHz, at frequencies below this AC electroosmosis is dominant [16].

With the known electrothermal force (volumetric force), a momentum balance can be performed on the fluid in order to solve for the velocity and pressure profile. The effect of temperature on the mass density of the medium is generally negligible but on viscosity the effect can be quite profound so the variation of viscosity with temperature generally must be accounted for in systems with significant electrothermal flow. Similar to the heat balance, based on frequency the velocity essentially reaches instantaneous steady-state. Writing the momentum balance for an incompressible fluid at steady-state, the following equation is arrived at:

$$-\nabla p + \nabla \mu \cdot (\nabla \vec{u} + \nabla \vec{u}^\dagger) + \vec{f}_{elec} = \vec{u} \cdot \nabla \vec{u} \quad (2.30)$$

$$\nabla \cdot \vec{u} = 0 \quad (2.31)$$

Based on order of magnitude analysis, the inertial term in the Navier-Stokes equation (eqn. 2.30) can often be neglected and the momentum balance reduces to Stokes' equation.

2.4 Brownian and Gravitational Forces

2.4.1 Brownian Forces

Particles in suspension will experience a random force due to the thermal energy of the molecules in the suspension. For a single colloidal particle in a dilute suspension, the diffusion coefficient D is given by:

$$D_0 = \frac{k_B T}{6\pi\eta_f r_p} \quad (2.32)$$

where k_B is the Boltzmann constant, T is the temperature, η_f is the viscosity of the suspending fluid and r_p is the radius of suspended particles. For a concentrated suspension of hard spheres with volume fraction c , the diffusion coefficient (D) is given by [39]:

$$D = (1 - c)^2 \frac{k_B T}{6\pi\eta_s r_p} \frac{d(cZ)}{dc} \quad (2.33)$$

where D_0 is the diffusion coefficient of a single, isolated particle (eqn. 2.32), η_s is the suspension viscosity and Z is the compressibility factor of the suspension. The force on an isolated Brownian particle can be described by [40]:

$$\vec{F}_{brownian} = \left(\frac{2k_B T f}{\tau} \right)^{1/2} \vec{\xi} \quad (2.34)$$

In eqn. 2.34, the characteristic time, τ , is generally taken as the time-step for integration and ξ is a gaussian-distributed random normal vector. The magnitude of the brownian force is proportional to particle size to the power of 1/2, arising from the appearance of the friction factor in eqn. 2.34. Since the volume of a particle is generally speaking proportional to the cube of particle size and most of the other forces involve scale either with volume (DEP) or directly with particle size (viscous drag), this means that the relative effect of brownian motion increases as particle size decreases (also evident from examining the diffusion coefficient, which is inversely proportional to particle size). For micron-sized particles undergoing DEP

or EHD, the effect of brownian motion can generally be neglected but for submicron-sized particles the effects can be quite significant, depending on the relative intensities of the DEP and EHD effects.

2.4.2 Gravitational Forces

The gravitational force on colloidal particles is generally negligible compared to other forces in electrokinetic systems, although it becomes more relevant for larger particles and for weaker electric field strengths. The buoyancy force experienced by a spherical particle is given by:

$$\vec{F}_{buoyancy,p} = \frac{4}{3}\pi r_p^3(\rho_{m,p} - \rho_{m,m})\vec{g} \quad (2.35)$$

For the fluid, due to the localized heating effect (Joule heating), there is a change in mass density¹³. This change in fluid density will result in natural convection of the fluid, with hotter (i.e. lighter) fluid elements rising and colder (i.e. heavier) fluid elements sinking. This buoyancy force on the fluid is described by:

$$\vec{f}_{buoyancy,m} = \Delta\rho_m\vec{g} \quad (2.36)$$

Typically the buoyancy force is insignificant compared to electrical forces in the area near the electrodes, although given the dependence of electrical forces on frequency there can be cases where this is not true. Depending on the characteristic length of the system, buoyancy can start to play a larger role. Castellanos et al. (2003) found that in a system they studied, a characteristic system length larger than 300 μm resulted in the buoyancy force exceeding the electrothermal flow force [18]. For concentrated suspensions, this gravitational (sedimentation) effect can also be quite significant.

¹³ Generally, this change is fairly insignificant and is ignored, with the fluid assumed to be incompressible

2.5 Colloidal Interactions

2.5.1 Lifshitz-van der Waals Forces

van der Waals or Lifshitz-van der Waals (LW) forces are composed of three closely related but different phenomena: i. randomly orienting dipole-dipole interactions (orientation interactions), ii. randomly orienting dipole-induced dipole interactions (induction interactions) and iii. fluctuating dipole-induced dipole interactions (dispersion interactions). For macroscopic bodies in condensed systems only dispersion interactions are relevant but all of these forces can be described by the same basic set of equations [39, 41].

Hamaker developed an approach for calculating the interaction between two materials in a vacuum at short distances relying on the calculation of a constant A , known as the Hamaker constant. The Hamaker constant of a material interacting with the same material, A_{ii} , can be used to calculate the constant of a material interacting with a different material, A_{ij} , as $A_{ij} = \sqrt{A_{ii}A_{jj}}$. The combining rule for 3 body interactions is $A_{132} = A_{12} + A_{33} - A_{13} - A_{23}$ ¹⁴.

The relationship between the Gibbs free energy of interaction of a material with itself at a distance ℓ and the Hamaker constant A_{ii} can be expressed as:

$$\Delta G_{ii}(\ell) = -\frac{A_{ii}}{12\pi\ell^2} \quad (2.37)$$

The surface tension (LW component) can be found through the Hamaker constant by the final definition :

$$\gamma_i^{LW} = -\frac{\Delta G_{ii}}{2} = -\frac{A_{ii}}{24\pi\ell^2} \quad (2.38)$$

¹⁴ This follows from the following “reaction” scheme for the material, namely $\textcircled{1}\textcircled{3} + \textcircled{2}\textcircled{3} \longleftrightarrow \textcircled{1}\textcircled{2} + \textcircled{3}\textcircled{3}$

For the interaction energy between two materials, the following combining rule (Good-Girifalco-Fowkes) applies:

$$\gamma_{ij}^{LW} = (\sqrt{\gamma_i^{LW}} - \sqrt{\gamma_j^{LW}})^2 \quad (2.39)$$

The Gibbs free energy of interaction (*in vacuo*) can also be determined, based on eqn. 2.38 (the resulting equation is referred to as the Dupré equation):

$$\Delta G_{ij}^{LW} = \gamma_{ij}^{LW} - \gamma_i^{LW} - \gamma_j^{LW} \quad (2.40)$$

The interaction between one material, i , immersed in a second material, j , is (as a consequence of the Hamaker combining rule):

$$\Delta G_{iji}^{LW} = -2\gamma_{ij}^{LW} \quad (2.41)$$

For the purpose of this research, most experiments are done using spherical particles so flat plate-sphere (particle-substrate) and sphere-sphere (particle-particle) interactions are the most relevant. The interaction energies (and related forces) vs. distance (ℓ) for the relevant configurations are [41]:

$$\Delta G_{\ell}^{LW} = \begin{cases} \frac{2\pi\ell_0^2 R \Delta G_{\ell_0}^{LW}}{\ell} & \text{sphere of radius } R \text{ and a semi-infinite flat plate} \\ \frac{\pi\ell_0^2 R \Delta G_{\ell_0}^{LW}}{\ell} & \text{two spheres of radius } R \end{cases} \quad (2.42)$$

$$F_{\ell}^{LW} = \begin{cases} -\frac{2\pi\ell_0^2 R \Delta G_{\ell_0}^{LW}}{\ell^2} & \text{sphere of radius } R \text{ and a semi-infinite flat plate} \\ -\frac{\pi\ell_0^2 R \Delta G_{\ell_0}^{LW}}{\ell^2} & \text{two spheres of radius } R \end{cases} \quad (2.43)$$

In equations 2.42 and 2.43 ℓ_0 represents the minimum equilibrium distance. This value is not strictly speaking equal for all materials but the deviation is generally quite low compared to the average value of 1.57 Å (standard deviation is 0.09 Å). This spacing is also not strictly speaking the “true” equilibrium spacing but rather determined from using a known relationship for Hamaker constants in terms of ℓ_0 , with the Hamaker constants independently determined from spectroscopy or permittivity data, meaning that the relationship can be considered to be semi-empirical [41].

These expressions are valid for unretarded Lifshitz-van der Waals forces. In the time it takes the electric field of one atom to reach another and for the induced dipole to return to the first atom, the configuration of electrons will have changed to a significant degree and the dipoles will have a smaller attractive force. At distances approaching 100 Å the value of the Hamaker constant can be a great deal smaller than half of the unretarded value. Fortunately, due to the presence of other forces (DEP, EHD, etc.) being much larger than the LW force at these larger distances, the relevance of this retardation is debateable for simulation purposes [41].

2.5.2 Acid/Base Forces

The Lifshitz-van der Waals forces are apolar interactions, which can be treated in the manner described in section (2.5.1) All other interactions, excluding electrostatic (see section (2.5.3)) and metallic, are considered to be “polar”. This methodology was worked in to a framework by van Oss, Chaudhury and Good [42, 43] who treat all polar interactions under a unified “acid-base” formalism. Specifically, polar interactions are defined as electron acceptor and electron donor interactions (Lewis acid-base) and considered to be an additive component of overall interfacial interaction energy, hence they are denoted by the superscript AB .

The overall form of the AB interactions are taken as an asymmetric relationship, allowing for

the fact that the electron donator and acceptor properties of a substance are not equal and that the effect of one parameter will not be felt unless the materials can interact reciprocally (i.e. acceptor of i and donator of j or donator of i and acceptor of j). The following relationship was proposed, on the basis of previous work done with electrostatic interactions between two different materials [41]:

$$\Delta G_{ij}^{AB} = -2\sqrt{\gamma_i^{\oplus}\gamma_j^{\ominus}} - 2\sqrt{\gamma_i^{\ominus}\gamma_j^{\oplus}} \quad (2.44)$$

where in eqn. 2.44 γ_i^{\oplus} represents the electron acceptor (Lewis Acid) and γ_i^{\ominus} the electron donor (Lewis Base) interfacial tension component of species i . Based on the definition of interfacial tension, which is independent of what the type of interaction is, the AB interfacial tension can be defined as:

$$\gamma_i^{AB} = 2\sqrt{\gamma_i^{\oplus}\gamma_i^{\ominus}} \quad (2.45)$$

Writing the Dupré equation, eqn. 2.40, for these types of interactions and substituting in eqn. 2.44 the following relationship is achieved:

$$\gamma_{ij}^{AB} = 2(\sqrt{\gamma_i^{\oplus}} - \sqrt{\gamma_j^{\ominus}})(\sqrt{\gamma_i^{\ominus}} - \sqrt{\gamma_j^{\oplus}}) \quad (2.46)$$

This relationship is significant since it allows for the AB interfacial tension to be negative, that is for a positive acid-base Gibbs free energy of interaction. The overall meaning of this is that for a material immersed in a medium, it is now possible to achieve an overall repulsive interaction, i.e. for a material to be suspended. Without this asymmetry between the electron donor and electron acceptor, there would be by necessity a positive interfacial tension component and a negative Gibbs free energy (always attractive) [41].

In terms of rate of decay with distance of interaction energy/force, the following relationships

have been proposed for the geometries most of interest to this work [41]:

$$\Delta G_{\ell}^{AB} = \begin{cases} 2\pi R\lambda\Delta G_{\ell_0}^{AB} \exp\left[\frac{\ell_0 - \ell}{\lambda}\right] & \text{sphere of radius } R \text{ and a semi-infinite flat plate} \\ \pi R\lambda\Delta G_{\ell_0}^{AB} \exp\left[\frac{\ell_0 - \ell}{\lambda}\right] & \text{two spheres of radius } R \end{cases} \quad (2.47)$$

$$F_{\ell}^{AB} = \begin{cases} -2\pi R\Delta G_{\ell_0}^{AB} \exp\left[\frac{\ell_0 - \ell}{\lambda}\right] & \text{sphere of radius } R \text{ and a semi-infinite flat plate} \\ -\pi R\Delta G_{\ell_0}^{AB} \exp\left[\frac{\ell_0 - \ell}{\lambda}\right] & \text{two spheres of radius } R \end{cases} \quad (2.48)$$

In equations 2.47 and 2.48 ℓ_0 is the minimum equilibrium distance, which is also used in eqn. 2.42 and λ is the decay or correlation length of molecules within the liquid medium. λ for pure water has been determined at 0.2 nm but in practice tends to be closer to 1 nm due to clustering of molecules and can even be much higher in certain cases [41].

One limitation of this approach is that to date there has been no ability to independently determine $\gamma_i^{\oplus}/\gamma_i^{\ominus}$ and all current tabulated values are in fact based on a ratio with an assumed value for water. Calculation of the LW component of interfacial tension for water at 20°C (based on dielectric permittivity relationships available in [41]) gives a value of 21.8 mJ/m², while water has an overall interfacial tension of 72.8 mJ/m². This implies that the AB interfacial tension component of water at 20°C is 51 mJ/m². The ratio of the electron acceptor to electron donor components of water was chosen as unity¹⁵ and from eqn. 2.45 the values for water can be determined as $\gamma_{H_2O}^{\oplus} = \gamma_{H_2O}^{\ominus} = 25.5$ mJ/m².

¹⁵ for simplicity of calculation and since a relative scale system versus water yields the same results independent of the choice of ratio [41–43]

Another limitation of this approach is that the value of λ is treated as independent of the material interacting with the medium, which is almost certainly not universally true, and as the relationship is exponential this factor is exceedingly important in determining the magnitude of interactions. For systems other than water, this factor is not well characterized either and the entire approach of treating all polar interactions as being described by a decaying exponential relationship with a single decay parameter is semi-empirical at best [44]. However, the approach is fairly robust, particularly in terms of dealing with aqueous media and as this will be the predominant choice (at least initially) in this work, the van Oss framework is well suited to this research.

2.5.3 Electrostatic Forces

Electrostatic interactions (EL) comprise the remainder of the classic colloidal interactions, along with LW and AB interactions. Interfaces between solids and solutions acquire charges by one of the following mechanisms [39]:

1. Differences in electron affinities between the two phases
2. Differences in ionic affinities between the two phases
3. Ionization of surface groups of one phase
4. Entrapment of ions in a lattice where substitution of one ion for another confers a charge

In order to maintain electroneutrality the fluid near this solid will contain opposing charges. The surface charge is maintained in a region known as the Stern layer where ions are immobile and the opposing charges are contained in the diffuse layer, where they are free to move under the influence of electrical and thermal forces. The application of an electric field

tangential to the double layer gives rise to electroosmotic flow, from the motion of the ions in the diffuse portion of the double layer (see section 2.3.1). The Stern layer is hypothesized to be the size of one hydrated ion radius, while the diffuse layer is generally taken as being equal to the Debye length. The two layers, Stern and diffuse, compromise the electrical double layer [21, 39]. A schematic of the double layer is provided in Fig. (2.4).

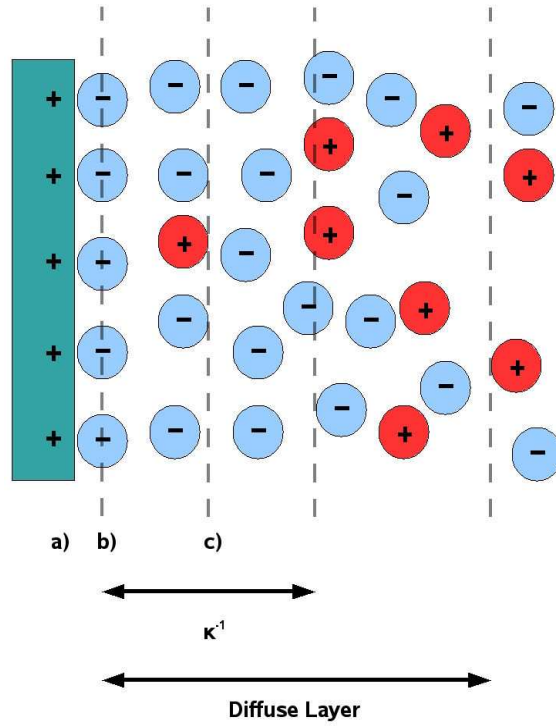


Figure 2.4: Double Layer Schematic
a) *Charged Surface*, b) *Stern Plane*, c) *Shear Plane*
Adapted from [21]

The electrostatic potential must satisfy Poisson's relationship:

$$\varepsilon \nabla^2 \phi = -\rho_f \quad (2.49)$$

The free charge density arising from the charges in solution is determined by recognizing that the diffuse region is in equilibrium so that the gradient of chemical potential must vanish, resulting in the Boltzmann distribution for ions in solution[39]:

$$n^k = n_b^k \exp \left[\frac{-ez^k\phi}{k_B T} \right] \quad (2.50)$$

The free charge density from the ionic species is then [39]:

$$\rho^f = \sum_1^N ez^k n^k \quad (2.51)$$

Combining equations 2.49, 2.50 and 2.51 gives rise to the Poisson-Boltzmann equation for electrostatic potential [39]:

$$\varepsilon \nabla^2 \phi = -e \sum_1^N z^k n_b^k \exp \left[\frac{-ez^k\phi}{k_B T} \right] \quad (2.52)$$

This equation is the core of the Poisson-Boltzmann model for the diffuse double layer. The primary assumptions are the electrolyte being an ideal solution with uniform dielectric properties¹⁶, ions are point charges and the ionic distribution is governed by the Boltzmann relationship [39].

All expressions for determining electrostatic interactions depend on using the Poisson-Boltzmann model in some manner, whether through analytical simplifications (such as linearization) or numerical simulations. van Oss (2006) provides analytical expressions for a symmetric 1:1 electrolyte, derived using the Derjaguin approximation but these are valid only at very low

¹⁶ Even in the case of temperature rise due to ohmic heating, there is unlikely to be a significant effect over the region defined by the double layer so that temperature may be safely assumed to be a constant value

surface potential ($< 25\text{-}50$ mV depending on double layer thickness)¹⁷ [41]. The expressions will be provided here for the sake of completeness but they will not be used unless zeta potential measurements show that the approximations are appropriate.

$$\Delta G_\ell^{EL} = \begin{cases} \varepsilon R \Psi_0^2 \log \left[1 + \exp(-\kappa \ell) \right] & \text{sphere of radius } R \text{ and a semi-infinite flat plate} \\ \frac{1}{2} \varepsilon R \Psi_0^2 \log \left[1 + \exp(-\kappa \ell) \right] & \text{two spheres of radius } R \end{cases} \quad (2.53)$$

$$F_\ell^{EL} = \begin{cases} -\varepsilon(\kappa R) \Psi_0^2 \frac{\exp(-\kappa \ell)}{1 + \exp(-\kappa \ell)} & \text{sphere of radius } R \text{ and a semi-infinite flat plate} \\ -\frac{1}{2} \varepsilon(\kappa R) \Psi_0^2 \frac{\exp(-\kappa \ell)}{1 + \exp(-\kappa \ell)} & \text{two spheres of radius } R \end{cases} \quad (2.54)$$

In equations 2.53 and 2.54 κ refers to the Debye parameter and Ψ_0 to the surface (or zeta) potential, where for two different materials A and B the value is calculated as $\Psi_0 = \sqrt{\Psi_0^A \Psi_0^B}$. The inverse of the Debye parameter is κ^{-1} and this is the Debye length, which is the effective thickness of the diffuse double layer [41]. The zeta potential is defined as the potential at which the no-slip condition is assumed to apply, which is one-half of the Debye length away from the Stern layer. The “true” surface potential, that at the Stern layer, is approximately the same as the zeta potential and is generally indistinguishable experimentally so zeta potential measurements are used to determine Ψ_0 [21, 41]. The Debye length can be calculated for a symmetric electrolyte in water as [21]:

$$\kappa^{-1} = \sqrt{\frac{\varepsilon k_B T}{2e^2 z^2 n_b}} \quad (2.55)$$

¹⁷ The given force expression in van Oss (2006) is not correct, as can be plainly seen from differentiating the energy expression w.r.t. distance. The corrected version is used here and matches that of Russel et al. (1989), except in sign convention [39]

For the case of non-aqueous media, the Debye length can be calculated as [45]:

$$\kappa^{-1} = \sqrt{\frac{\varepsilon k_B T}{2e^2 n}} \quad (2.56)$$

where the ionic concentration, n , is estimated as $n = \frac{\sigma F}{e\Lambda_0}$, with σ being the liquid conductivity, F is Faraday's constant and Λ_0 the equivalent conductance of the suspension which is determined by Walden's law, $\Lambda_{0,aq}\mu_{aq} = \Lambda_{0,non-aq}\mu_{non-aq}$ [45]. In the case where the zeta potential is not low ($e\zeta/k_B T > 2$), but the double layer is thin ($\kappa r_p \gg 1$) the following expression can be used to evaluate electrostatic interaction between particles [39]:

$$F_\ell^{EL} = -32\pi\varepsilon \left(\frac{k_B T}{ze} \right)^2 \kappa r_p \tanh\left(\frac{1}{4}\Psi_0\right) \exp(-\kappa\ell) \quad (2.57)$$

Construction of a total force (or energy) vs. distance plot using all three types of interactions (LW, AB and EL) is helpful in determining the existence of maxima (or minima in the case of energy), indicating that particles will no longer be suspended in the medium but aggregate together if they are brought to a certain distance. However, this is limited in that it does not consider interactions of more than 2 particles or even the summation of interactions over all particle pairs. To extend to this effect, more complicated approaches are required and one such approach is described in the next section.

2.6 Free Energy of Suspension Under Electric Field

To describe the phase separation of a colloidal suspension under the influence of non-uniform electric field effects, Kumar et al. (2007) developed an expression suitable for high concentration suspensions which required no fitting parameters [46]. This approach consisted of a thermodynamic approach to describing the colloidal suspension, modified from previous work by Khusid and Acrivos (1995, 1996, 1999), which allowed for calculation of osmotic pressure and chemical potential and then used equilibrium conditions in order to elucidate

where phase separation took place and the effect of colloidal flux on the fluid [47–49]. In this approach, colloidal interactions are treated using a hard-sphere approach (Carnahan-Starling compressibility factor), as the electric field effects are presumed to dominate at larger intra-particle distances (DEP/mutual DEP effects). Consequently, this model will likely work well for colloidal systems where the hard-sphere approach is well suited (colloidal latex in water for example) but may possibly break down for more complicated systems. In this research to date, colloidal latex/silica in water have been used as the model systems and consequently the hard-sphere approximation has been suitable as a first attempt at describing assemblies.

The time-averaged chemical potential and osmotic pressure of a colloidal suspension undergoing negative dielectrophoresis are given by eqn. 2.58 and 2.59 respectively [46]:

$$\mu_p = \frac{k_B T}{v_p} \frac{df_0}{dc} - \left(\frac{\partial \varepsilon_s}{\partial c} \right)_{\omega t_c} |\vec{E}_{rms}|^2 \quad \text{where} \quad f_0 = c \ln \frac{c}{e} + c \int_0^c \frac{Z(c) - 1}{c} dc \quad (2.58)$$

$$\Pi_p = \frac{k_B T}{v_p} cZ + \left[\varepsilon_s - c \left(\frac{\partial \varepsilon_s}{\partial c} \right)_{\omega t_c} \right] |\vec{E}_{rms}|^2 \quad (2.59)$$

where $k_B T$ is thermal energy, c is particle volume fraction, Z is suspension compressibility factor, ε_s is the real part of suspension permittivity and $\left(\frac{\partial \varepsilon_s}{\partial c} \right)_{\omega t_c}$ is the derivative of the real part of the suspension permittivity with respect to particle volume fraction. The suspension compressibility factor can be calculated using the Carnahan-Starling equation (eqn. 2.60) and the suspension permittivity from the Maxwell-Wagner expression (eqn. 2.61) [46]:

$$Z = \begin{cases} \frac{1 + c + c^2 - c^3}{(1 - c)^3} & 0 < c \leq 0.5 \\ \frac{2.34}{0.68 - c} & 0.5 < c \leq 0.68 \end{cases} \quad (2.60)$$

$$\tilde{\epsilon}_s = \tilde{\epsilon}_m \frac{1 + 2c\tilde{K}_e}{1 - c\tilde{K}_e} \quad (2.61)$$

where in eqn. 2.61 $\tilde{\epsilon}_i$ is the complex permittivity of the suspension and medium (subscript s and m respectively) and \tilde{K}_e is the Clausius-Mossotti factor defined in section 2.2.1.

Along the coexistence curve for the single phase region of the suspension vs. a two-phase region induced by the electric field effects, the value of chemical potential and osmotic pressure of each phase are equal. The volume fraction of particles in each phase is denoted by c_1 and c_2 where 1 refers to the low solids concentration phase and 2 to the high solids concentration phase respectively [46]:

$$\mu_p(c_1) = \mu_p(c_2) \quad \text{and} \quad \Pi_p(c_1) = \Pi_p(c_2) \quad (2.62)$$

The electric field profile of the suspension can be determined using Gauss' law with the permittivity described by eqn. 2.61 [46]:

$$\nabla \cdot [\epsilon_s(c) \nabla \phi] = 0 \quad \text{and} \quad \vec{E} = -\nabla \phi \quad (2.63)$$

The electrohydrodynamics are governed by the Navier-Stokes (or Stokes equation if the inertial term is shown to be negligible by order of magnitude analysis) with a volume force due to the motion of colloidal particles¹⁸ [46]:

$$\rho(c) \left(\frac{\partial \vec{u}}{\partial t} + \vec{u} \cdot \nabla \vec{u} \right) = -\nabla p + \nabla \cdot [\eta_s(c) (\nabla \vec{u} + \nabla \vec{u}^\dagger)] + c(\rho_p - \rho_f) \vec{g} - c \nabla \mu_p \quad \text{and} \quad \nabla \cdot \vec{u} = 0 \quad (2.64)$$

The momentum balance is no longer taken at steady-state since the volume force due to the motion of the colloidal particles has a much slower response time vs. that of the electric field, hence it is not necessarily appropriate to use the steady-state approximation used in

¹⁸ electroosmotic or electrothermal flow effects can be treated by adding either a slip-velocity boundary condition or an additional volume force as described in sections 2.3.1 and 2.3.2 respectively

section 2.3. The particle concentration is determined using a continuity equation, eqn. 2.65. In the original model of Kumar et al. (2007), the effect of diffusion was either ignored or treated as the dilute particle case, but this is not necessarily appropriate given the particle sizes and concentrations used for assembling structures.

$$\frac{\partial c}{\partial t} + \nabla \cdot (-D\nabla c + c\vec{u} + \vec{j}_p) = 0 \quad \text{where} \quad \vec{j}_p = \frac{c(1-c)^2 v_p}{6\pi r_p \eta(c)} [-\nabla \mu_p + (\rho_p - \rho_f)\vec{g}] \quad (2.65)$$

in equations 2.64 and 2.65 $\eta(c)$ is the suspension viscosity, which is determined by the relationship $\eta(c) = \eta_m(1 - c/0.68)^{-2}$ for hard spheres. The suspension is treated as Newtonian with a concentration dependent viscosity, ignoring the possible formation of a yield stress (electrorheological effects) due to permittivity of medium and applied frequency [46, 50]. In eqn. 2.64 $\rho(c)$ is the suspension density which can be roughly estimated by volume averaging as $\rho(c) = c\rho_p + (1 - c)\rho_m$. D is the diffusion coefficient, accounting for particle effects, which can be determined by eqn. 2.33 for a concentrated suspension of hard spheres. The effects of sedimentation are captured by the terms $c(\rho_p - \rho_f)\vec{g}$ in the momentum balance and $(\rho_p - \rho_f)\vec{g}$ in the particle flux equation. The volume fraction of the high solids phase (ψ) can be determined by the lever rule $c_2\psi + c_1(1 - \psi) = c$ where c is the total particle concentration. As an approximation, the viscosity and permittivity may be determined using the bulk concentration c [46], based on assuming phase separation happens on a much faster scale compared to the hydrodynamics.

Chapter 3: Survey of Existing Literature

3.1 Ordered Structures and Colloidal Crystal Applications

3.1.1 Recent Colloidal Crystallization Advances

A number of popular techniques for forming 3d ordered, crystalline structures from colloidal particles exist. These colloidal crystals are on a much larger scale compared with atomic crystals but can form similar types of lattice structures, for example face-centered-cubic (FCC), body centered cubic (BCC), etc. Sedimentation is one option for forming ordered colloidal structures, with the process being governed by a complicated interplay between gravitational, brownian and nucleation forces and tending to form FCC type lattices [1]. However, this approach yields poor control over the topology of the surface layer and on the overall number of layers deposited as well as taking a large amount of time to completely settle (between weeks and months for submicron sized particles) [1]. Minimizing electrostatic repulsion, which can be controlled by changing the colloid volume fraction or the Debye length of the medium, can lead to a change from a disordered suspension to an ordered crystalline phase [39]. This method is, however, very sensitive to temperature, monodispersity of particles, surface charge density and counterion density in the medium. The use of shear flow to induce a translational ordering over large distances is generally needed [1]. Self-assembly under geometric confinement is another possibility for formation of a 3d crystalline structure from colloidal particles. In this approach, packing cells are constructed and used to form 3d crystalline structures, generally with a cubic close-packed (ccp) lattice structure, requiring continuous sonication of the cell in order to achieve a crystalline lattice. This approach is quick and suitable for large scale templating but is limited in that packing cells are fragile and are generally suitable for a single-use only [51].

Another potential route for obtaining colloidal crystals is through solvent evaporation. This approach has been used recently by Fernández-Nieves to construct 3d arrays of liquid crystal drops and Kuncicky and Velev who used substrates of controlled contact angle to manipulate the air-water interface of a droplet to allow the creation of 3d crystalline structures of various geometries during evaporation [52, 53]. These types of structures, as mentioned previously, have numerous applications, ranging from templating the formation of other structures, such as photonics, scaffolds, membranes or sensors [54–56, 56].

3.1.2 Photonic Bandgap Applications

Mayers et al. used replica moulding in order to produce a cell for the formation of 3d colloidal structures which displayed opalescence [51]. This method was able to produce photonic lattices of the cm^2 scale area using monodisperse latex (polystyrene) spheres ($d_p = 255 \text{ nm}$ and 467 nm). The crystals had two troughs in the transmittance spectra, one at 614 nm which corresponded to the bandgap of the crystal (first-order Bragg diffraction) and one at 300 nm which was attributed to a combination of second-order Bragg diffraction and absorption. The technique of using replica molding (physical confinement) was able to provide a large degree of control over the number of monolayers but was limited in that the packing cells had low durability and were suitable for one use only [51].

In order to create crystals that have a bandgap of $1.3 \mu\text{m}$ or $1.5 \mu\text{m}$, which are two of the more technically useful wavelengths for optoelectronic applications, a particle diameter of $\sim 0.8 \mu\text{m}$ is required [57, 58]. Vlasov et al. describe the creation of a 3d crystalline silica structure (FCC lattice) which is suitable for templating an inverse photonic crystal that has a bandgap of $1.3 \mu\text{m}$ [58]. Using sedimentation solely to crystallize silica was described as ineffective due to a large number of defects in the crystal which fill in the bandgap, so an evaporating meniscus effect was used in order to provide convective control of the crystallization process. This approach was able to yield crystals up to 20 layers thick that coated a

cm² area, with an FCC structure that was believed to be due to shear forces from the evaporating meniscus [58]. The prepared crystals were then used as templates for the formation of inverse opals, with silicon used as the infiltration medium ($n_{\text{refractive}} = 3.5$, which is higher than the necessary value of 2.85 needed to form a complete bandgap). Silicon was deposited by using a low-pressure chemical vapour deposition process at 550°C followed by annealing at 600°C for 8 hours in order to convert amorphous Si into polycrystalline Si. This process was characterized by a very low number of point defects and stacking faults, which fill the bandgap, compared with using sedimentation alone [58].

Waterhouse and Waterland used sedimentation, centrifugation and a flow-controlled deposition process to facilitate the self-assembly of latex (PMMA) spheres between 280 and 415 nm in diameter into 3d photonic crystals and used silica, titania or ceria to form inverse opals [59]. They observed no discernable difference in crystal quality between methods, somewhat contradicting the results of Vlasov et al. who found that sedimentation was more prone to defects. One possible explanation of this discrepancy is that the work of Waterhouse and Waterland focused on the creation of pseudo photonic crystals, as the materials used (silica, titania, ceria) do not possess a sufficiently high refractive index in order to form a complete bandgap, so that the frequency of light allowed to propagate through the crystal would vary with the angle of incidence of the directed light. Therefore, the characteristic faults/defects in the crystal present in sedimentation may have had a lesser effect compared to the work of Vlasov et al., who were focused on constructing crystals with a complete bandgap (no dependence of bandgap on incident angle). These photonic crystals were found to have pseudo bandgaps in the visible and near-IR regions of the light spectrum, with possible applications as solar cells [59].

Another potential application of electric field templated ordered structures is as microdevices. For example, microgears are often fabricated using lithographic techniques (formation

of micromoulds for example). [60, 61]. These structures can be used as components in larger microsystem devices, such as micropumps [62, 63]. The formation of an optically controlled microgear suitable for use in micropumps has been demonstrated. This device achieved rotation via the transfer of spin momentum from the light to the gear as a result of optical birefringence, which was due to a 1d photonic lattice embedded in the gear [63]. As an alternative, electric field effects (DEP/EHD) could be used in order to assemble a 3d microgear-type geometric structure which possibly, depending on the conditions of the assembly, would be a photonic bandgap material and thus suitable for optically controlled rotation.

3.1.3 Scaffolding Applications

3d colloidal crystals have also been used for templating inverse macroporous structures for use as tissue engineering scaffolds, using polystyrene latex to form the crystal and sodium silicate sol to form the inverse material, which is a gel (sol-gel process) [64]. Optimal growth of carcinoma and human bone marrow cell cultures was achieved using a $75\text{ }\mu\text{m}$ spherical latex particles to template the inverse scaffold. The scaffolds had a larger degree of internal order than is generally used in tissue engineering studies and were suitable for use in studies of cell interactions and motility during the growth phase. This is another example of a potential application of the colloidal crystals formed during the course of this work, as our group is interested in development of electrokinetically assembled scaffolding materials and have demonstrated the use of DEP to assemble aligned MWCNT surfaces for growth of tissues [65].

3.1.4 SERS Applications

Surface enhanced Raman spectroscopy is the enhancement of a Raman signal found when a metallic thin film (generally, gold or silver) is used as the substrate for the material being

studied by Raman spectroscopy [9]. This enhancement is generally attributed to two mechanisms: i) electromagnetic enhancement, due to high localized fields from the generation of a surface plasmon resonance (SPR) and ii) chemical enhancement due to a resonance interaction between substrate and absorbate [66]. Specifically, 2d and 3d crystalline structures or ordered films (inverse structures) of gold or silver are very useful for enhancement of the Raman signal and a number of demonstrations of this has been provided in the literature [9, 67, 68]. Lu et al. (2005) demonstrated the use of a multilayer polyelectrolyte crystalline structure which is gold coated and used for SERS applications [68]. .

3.2 General Electrokinetic Papers

A variety of general review papers to various electrokinetic phenomena exist. A comprehensive review of the behaviour of the forces in AC electrokinetic systems was performed by Ramos et al. and Green et al., dealing primarily with forces on the medium and on colloidal particles respectively [17, 24]. In terms of dealing with electrohydrodynamic effects, a number of general reviews exist on the effects of voltage, frequency, ionic conductivity, etc. on observed experimental systems and numerical simulations [33, 35, 69, 70]. Castellanos et al. derived a general scaling law for EHD behaviour in microsystems, which is useful for estimating magnitudes of electrothermal and electroosmotic velocities, as well as the frequencies and conductivities where they are relevant [18].

3.3 DEP Assembly

A comprehensive review of the use of dielectrophoresis for colloidal assembly was written by Velev and Bhatt [71]. Dielectrophoresis has been employed to create 1d, 2d and 3d colloidal assemblies from a variety of materials, including carbon black, carbon nanotubes, silica and gold. Hermanson et al. achieved the first demonstrated microwire from colloidal particles

using dielectrophoresis [72]. In this work, the authors used gold nanoparticles ranging in size between 15 and 30 nm and achieved wires as long as 5 mm. The pattern of the formed wires was highly sensitive to applied voltage, frequency and particle size, with a fractal-type branching pattern observed during wire formation [72]. This work was followed up in by Tang et al. who created 1d nanotube wires using single-walled carbon nanotubes and by Lumsdon and Scott who achieved a similar microwire, this time grown from carbon black nanoparticles ($d_p = 30$ nm) and carbon nanotubes of diameter between 15 to 50 nm [73, 74]. The authors of the latter noted the same branching-growth pattern and achieved wires of a comparable length to the work of Hermanson et al. (3 mm vs. 5 mm).

Evoy et al. used DEP assembled rhodium nanorods as nanosensors based on integration with CMOS circuitry [75]. Li et al. used AC dielectrophoresis to selectively position single wall carbon nanotubes for field effect transistors, achieving a relatively high degree of success in forming functional transistors ($\sim 60\%$ success rate) [76]. Sun et al. report the chaining of gold/polymeric aniline particles into 1d nanostructures, demonstrating that inhomogeneous particle pairs can be assembled into chains under dielectrophoresis [77]. Seo et al. constructed bundles of single-walled carbon nanotubes using dielectrophoresis and were able to achieve controlled positioning of the nanotubes by designing the microelectrode system used for alignment [78]. More recently, Papadakis et al. used dielectrophoresis to control the formation of metallic nanowires of silver and gold nanoparticles, being able to achieve the formation of vertically aligned nanowire arrays which are suitable for integration with CMOS and MEMS devices [79]. Ranjan et al. constructed 1d palladium nanowires using dielectrophoretic effects in an aqueous palladium salt solution, achieving wires with a thickness of 5 - 10 nm [80]. They observed that the DEP directed assembly follows the universal pattern of diffusion-limited aggregation, as has been observed by other authors in this area (branching pattern growth) [80, 81]. Barsotti et al. achieved the assembly of gold nanoparticles into nanowires (consisting of as few as 10 particles), $d_p = 20$ nm, using

dielectrophoresis with planar nanoelectrodes having a gap spacing ranging from 15 to 150 nm [82].

The use of continuous flow systems which utilize DEP effects in order to pattern colloidal particles into defined positions has also been demonstrated [83, 84]. Dürr et al. used a microdevice with 3d arrays of microelectrodes in order to provide DEP trapping of polystyrene latex particles between 250 nm and 12 μm in aqueous buffer solutions (PBS). The authors were primarily interested in the behaviour of particles and electrodes, in particular the impedance of the electrodes. No attempts were made to model the effects of the EHD flows which were certainly generated under these conditions (conductivity in some experiments was 170 mS/m) [83]. In a more recent article a peristaltic pump (rather than EHD effects) were used to provide fluid motion for a continuous flow device with a DEP trap. A DEP trap was established and latex beads could be trapped in defined positions within an agarose gel. The proposed application of the device is to use with living cells and create tissue-like materials (with mammalian cells) or for example use bacteria and create a biofilm, with a defined particle structure [84]. One interesting aspect of this work is that the medium conductivity effect was mentioned in terms of simulations done on the device performance, in terms of the effect on the Clausius-Mossotti factor, but not in terms of the possibly electrothermal flow effects arising from Ohmic heating of a conducting medium. This may play a very significant role, particularly in the bioapplications proposed by the authors, and was also the case in the work of Dürr et al., indicating that this particular branch of DEP based traps is in a preliminary state of model development [83].

In terms of two-dimensional assemblies with dielectrophoresis, the field is considerably less developed. Lumsdon et al. described the assembly of 2d photonic crystals from colloidal latex and silica [85]. The crystals achieved an area of up to $\sim 25\text{mm}^2$ in a template-free environment. Lattice spacing could be controlled by modulating electrostatic repulsion through

the addition of electrolytic salts to the medium, which increases the screening effect of the electrical double layer (double layer decreases in size but is more substantial in mitigating electrostatic interactions) [41, 85]. The effect of viscosity was examined as well, and was determined to play a significant role in determining if crystal formation would occur. This work was followed up by the same group and it was postulated that the viscosity may play a role in inhibiting particle growth by suppressing counterion mobility, thereby altering DEP and mutual DEP effects [86]. In this work, colloidal latex and silica (d_p between 0.7 and 1.4 μm) were assembled using coplanar electrodes under the influence of an AC field. In addition to dipole-field interactions (dielectrophoresis) there were dipole-dipole interactions between particles (mutual dielectrophoresis). The electrode gap spacing was adjustable between 2 and 10mm and the applied voltage ranged from 40 to 100 V and frequency from 0.2 to 20 kHz. The combination of these two effects led to the rapid assembly of one-dimensional chains (2 seconds) and two-dimensional crystals (within 4 seconds) for latex.

A possible mechanism for this assembly process was outlined after examining diffraction patterns observed during the assembly. Particles will form 1d chains due to the mutual DEP force while the DEP force from the electrodes will drive these chains towards the electrode surface. The chains will then crystallize to form hexagonally packed crystals (under the conditions studied here), aligned by the influence of the external field. An optical shift was observed depending on the state of the crystalline lattice, specifically for the one-dimensional chains if light is applied perpendicular to the field then there would be no observed colour but if applied parallel, a bright colour pattern was observed. In the case of the two-dimensional crystal, this pattern was observed no matter what direction light was applied [86].

For three-dimensional assemblies using dielectrophoresis alone, there are even fewer examples demonstrated in the literature. Docoslis and Alexandridis demonstrated the first use of dielectrophoresis to generate three-dimensional structures using a quadrupolar electrode set

with silica and latex particles [87]. In this paper, latex particles ($4.4\ \mu\text{m}$), silica particles ($2.1\ \mu\text{m}$) and graphite particles ($5\ \mu\text{m}$) in water were assembled into 1d, 2d and 3d structures using a hyperbolic electrode set with a gap spacing of $300\ \mu\text{m}$. Pyramid-type structures with a width of close to $270\ \mu\text{m}$ and a height between 75 to $100\ \mu\text{m}$ were created with silica particles. The structure assembled within a few minutes but would collapse almost immediately upon cancellation of the electric field. In order to maintain the structure for imaging after experiments, pluronic F-105 was added to water in order to cause gelation upon evaporation of the water. Pluronic is a tri-block copolymer of poly(ethylene oxide) and poly(propylene oxide) and will undergo transition to a gel state above the critical micellization concentration. The gel was then removed in the area of interest by burning using an electron beam before SEM was performed [88]. An alternative and possibly more practical method is to first dry the gel in an oven and then use UV/Ozone to degrade the pluronic. This technique has been used to remove pluronic gels from surfactant-templated thin films [89, 90].

The technique of using hyperbolic electrodes for collection and assembly of multilayer structures was repeated by Abe et al. who used 2 , 5 and $10\ \mu\text{m}$ latex particles (polystyrene) with a set of electrodes having a $400\ \mu\text{m}$ gap spacing, achieving a similar structure to the work of Docoslis and Alexandridis, as observed under optical microscopy [91]. This paper was not concerned with maintaining or investigating the structure under SEM, so no attempts were made at physical stabilization (cross-linking or gelation). This work was successful in achieving a colloidal aggregate but no crystalline phase was demonstrated, possibly due to disruption of the structure during medium evaporation or to the use of distilled water as opposed to an ionic solution which mitigates electrostatic repulsion via the diffuse double layer. They observed that upon lowering the frequency of the applied field to $100\ \text{kHz}$ any formed structure would be disrupted but did not attribute any cause to this. One strong possibility is that the onset of electroosmotic flows, which becomes relevant at frequencies of approximately $100\ \text{kHz}$, caused the disruption of the DEP trap at the center of the electrodes

and broke up the assembled structure [16].

Khanduja et al. reported the construction of a three-dimensional gold nanoparticle bridge between two microelectrodes [92]. The particle size is 50 nm, which is quite small when using DEP only, however, the characteristic gap spacing between the electrodes was $0.7\ \mu\text{m}$. The methodology in this technique is to deposit the electrodes in a such a manner that the gap between them is in fact in the vertical direction. A thin layer of gold is applied to a silicon dioxide layer on a wafer, then a layer of parylene is added and another layer of gold is placed on top of the parylene (incomplete coverage). The parylene not covered in gold is then etched using plasma and a set of microelectrodes with a thin gap ($0.7\ \mu\text{m}$) is created. By using only applied voltages up to 2 V, they were able to bridge the gap between electrodes and have an average resistance of $40\ \sim\ \Omega$ [92]. However, this technique is limited to causing significant growth in one-direction (vertical in this case), with a small growth in the radial direction.

3.4 EHD Assembly

The study of the effects of an electric field on a fluid medium is known as electrohydrodynamics. This is primarily broken down into two areas for electric field induced flow, known as electroosmosis (action of tangential component of electric field on electrical double layer causing flow) or electrothermal flow (gradient in permittivity and conductivity due to temperature gradients causing flow). The description of these effects and analysis of each is provided in numerous references, for example Ramos et al. and Gonzalez et al. [33, 35]. Electrohydrodynamic (EHD) effects have been used by numerous authors for to create colloidal assemblies or assist dielectrophoretic driven assembly, as reviewed in Velez and Bhatt [71].

Trau et al. used electrohydrodynamic flow to assemble electrophoretically deposited colloidal polystyrene particles into 2-dimensional crystals. Flows are induced due to particle deposition near the electrodes altering the electric field profile, leading to charge imbalances and a net fluid flow. These flows induce lateral attractions between colloidal particles and lead to a transition from a suspended state to a 2d crystal [93]. This work was followed up later with a detailed mathematical model determining the flow induced by perturbation of the field due to the presence of particles was used in order to justify the hypothesis that lateral attractions between particles were in fact the work of electrohydrodynamic flows [94]. This flow is similar in nature to electroosmotic flow, explaining the dependence on frequency (i.e. at high frequencies, flow becomes negligible). Gong et al. used an applied electric field between two parallel plates to incite crystallization of polystyrene using a similar manner to that described by Trau et al. [95]. The difference being in this work the gap spacing was $12.5\ \mu\text{m}$ compared to the $200\ \mu\text{m}$ used by Trau et al. for their work. Three dimensional polycrystallite structures from polystyrene were achieved under the influence of dipole-dipole interactions and electrohydrodynamic flows induced by the presence of colloidal particles.

Ristenpart et al. developed a scaling law to describe the aggregation of colloidal particles under the influence of electrohydrodynamic effects. The basic methodology was to determine a balance between the electric and viscous stresses on an isolated particle, determine the electric field perturbation due to the dipole of this particle and using the Helmholtz-Smoluchowski expression for EO velocity determine an expression for the rate of aggregation of particles [96]. The overall expression was proportional to the square of the applied potential and to the Debye length of the medium and inversely proportional to the applied frequency and medium viscosity. This shows the strong dependence on the double layer of the assembly process (debye length and frequency effect). This result may help to explain the behaviour noted by Lumsdon et al. (discussed in sec. 3.3) with regards to lateral flows inducing 2d crystal formation and the relevance of viscosity and frequency to this process [86].

Electroosmotic flow has been coupled with DEP in order to assemble rod-shaped multiwall carbon nanotubes (MWCNTs) into 1d nanowires [97]. Due to the small size of the particles, the DEP force from electrodes only becomes significant when the particles are within a few microns of the electrodes. In order to compensate for this effect, a DC bias was combined with an AC signal to provide both electroosmotic flow (DC) and dielectrophoretic effects (AC). The end result was that MWCNTs could bridge an electrode array in an aligned manner with $\sim 90\%$ yield, with the array consisting of 100 electrode gaps. The electroosmotic flow was used to guide the initial deposition on the device and DEP was used in order to align and direct the final bridging between electrode gaps. The process is desirable in that it is straightforward to use to create large scale devices [97].

3.5 Current Modeling Work

For modeling of DEP/EHD systems, most work to date has focused on particle free or dilute particle cases. That is, most authors focus on solving the electric field, temperature and velocity profile (as needed) of the medium, unperturbed by the presence of particles, and then calculate the dielectrophoretic force on an isolated particle and compare this in magnitude to drag force or calculate the overall particle velocity and determine particle trajectory in the area near the electrodes in regards to the effectiveness of a DEP trap (force described by eq. 2.12, sec. 2.2.2) [98–103].

In terms of dealing with systems with particles, a few innovative approaches have been demonstrated recently. Lin (2006) used a molecular dynamics (MD) type approach to describe the motion of yeast cells under the influence of DEP force. This approach is fairly simple to implement, with the interaction force between particles described using the point dipole approximation and brownian forces can be added as necessary. The disadvantages are

two-fold: i) the computational intensity scales poorly with number of particles, as an $D \times N$ ODEs are needed to describe the motion of N particles in D dimensions ($2 \times D \times N$ if velocity needs to be explicitly solved for in the time-integration scheme) and ii) evaluating the effect of the particles on the electric field is also difficult numerically, with the usual approach being to ignore this effect. Kadaksham et al. demonstrated the use of a distributed Lagrange multiplier (DLM) method in order to treat the motion of a group colloidal particles (down to nanoscale) suspended in a medium [31, 104]. In this approach, hydrodynamic forces are accounted for using a distributed Lagrange multiplier and the solid is solved within the fluid-solid domain with motion inside the particle forced to be that of a rigid body based on the lagrange multiplier. The motion of 100 nanoparticles undergoing negative dielectrophoresis was modelled successfully using this technique but it becomes computationally prohibitive for larger numbers of particles as it amounts to having to solve the motion of each individual particle, as in the MD-type approach [104]. This approach is essentially the same as that of a MD-type approach with the additional complication of having to solve the hydrodynamic equation for the fluid and not treating the particle as a point dipole for the purposes of flow.

In terms of modeling the suspension as a continuum, there has been interesting work done in treating the system in terms of phase separation kinetics. Johnson et al. [105] treat the phase separation of a colloidal particle suspension as being governed by the thermodynamics, where the free energy is calculated as function of the applied field and particle concentration. This approach used a Cahn-Hilliard type equation to govern the evolution of an electric field induced pattern. The effects of the particle on the dielectric constant of the suspension were treated in an empirical manner and the effects of fluid flow were ignored. Similarly, Kumar et al. developed a model for the electric field, velocity and particle concentration profiles, based on a driving force derived from chemical potential (described in sec. 2.6). This approach is also similar in form to a Cahn-Hilliard type equation, meaning it inherits the numerical instabilities associated with attempting to solve for the time-evolution of

concentration [46, 106]. As such, the authors have mostly limited solution to steady-state cases, with a stationary fluid and used a simplified geometry to describe the electric field profile analytically, choosing to focus on the phase diagram of particles under the influence of the electric field [46].

Chapter 4: Assembly of Colloidal Structures using AC Electrokinetic Forces from Non-Uniform Electric Fields

Abstract

The use of AC electrokinetic forces from spatially non-uniform electric fields for the assembly of colloidal structures is considered. Spatially non-uniform electric fields are generated using $100\mu\text{m}$ gap quadrupolar planar microelectrodes. The application of these electric fields gives rise to dielectrophoretic (DEP) and electroosmotic (EO) forces which can be used to manipulate individual colloids into larger structures in a contact-free manner. A number of different particle and medium combinations were explored, silica-water, silica-DMSO, PMMA-water, etc. It was found that near-refractive index matching of suspensions encouraged ordered-type structures, as was evident from aligned groups of particle chains visible under optical microscopy. All assemblies showed significant distortion and damage upon medium evaporation, leading to the investigation of various stabilization techniques to maintain structures. Out of the methods studied, medium gelation using pluronic F-127 was found to be the most effective at preserving the overall shape and size of an assembly but use of a surfactant inhibited the disorder-order transition. Use of pluronic F-127 allowed for preserving structures which shifted significantly with voltage, from an “inverse” four hole structure corresponding to the minimum gap spacing between electrodes to a large “diamond” type structure at higher voltages. More conventional polymer immobilization techniques for colloidal crystals, such as using PEGMA/PEGDMA or ETPTA, were ineffective for the assemblies in this work.

4.1 Introduction

Colloidal crystals and ordered colloidal structures have recently found many applications in emerging research fields. Applications of colloidal crystals range from use as photonic materials (PBG), sensors, microelectronics, dye sensitized solar cells, scaffolds for tissue engineering applications to templates for surface-enhanced Raman spectroscopy [1–9]. Numerous techniques are available for fabricating these types of structures, including self-assembly, template-assisted assembly and assembly driven by an external field such as gravitational, electrical or magnetic [10–14]. Electric fields in particular offer a number of advantages, they provide a large number of control parameters (voltage, medium and particle electrical properties) and can be scaled to very large intensities at low power by reducing the characteristic gap between electrodes, while not being restricted to ferromaterials as magnetic fields are. Additionally, the action of an applied electric field can lead to fluid motion, further adding to potential control forces for assembly. The collective action of direct electrical forces and induced fluid forces for an AC electric field are known as AC electrokinetics.

AC electrokinetics has been widely used to construct structures of varying size, order and geometry from colloids. Docoslis and Alexandridis demonstrated the first use of dielectrophoresis for the assembly of three-dimensional colloidal structures, using $100\mu\text{m}$ gap quadrupolar planar microelectrodes to assemble silica and latex colloids [20]. Abe et al. utilized a $400\mu\text{m}$ gap hyperbolic electrode set for assembly of polystyrene (PS) colloids ($2\text{--}10\mu\text{m}$) and were able to achieve single or multiple layer structures by using a combination of AC and DC fields [107]. Lumsdon and Scott formed 2d colloidal crystals from polystyrene colloids using applied electric fields which were field reversible [19, 74]. Reversible 2d colloidal crystals have been demonstrated by many additional works [93, 108–110]. Large-scale colloidal crystals $200\mu\text{m}$ in size have been formed without significant grain-boundaries by successive application and relaxation of an applied electric field in a hexapolar electrode system [111]. Three-dimensional structures of varying complexity has been demonstrated

using a combination of dielectrophoresis and induced-charge electroosmotic flows [112]. For a comprehensive overview of the use of AC electrokinetic forces for colloidal assembly, and for colloidal assembly in general, see the articles of Velez and Bhatt and Velez and Gupta [71, 113].

To date, there exists a dearth of experimental work aimed directly at forming three-dimensional colloidal crystals which have an ordered structure as well as an overall geometry structure determined by spatially non-uniform electric fields. The work of Docoslis and Alexandridis (2002) and Abe et al. (2004) represents the current state of the art as to using AC electrokinetic forces arising from non-uniform electric fields for controlling the shape, size and structure of assemblies of colloidal particles. To that end, in this work we exploit the following AC electrokinetic forces to attempt to control colloidal assembly. Dielectrophoresis, the force on a particle due to the action of a non-uniform electric field on an induced dipole, and electroosmotic flow, the fluid flow that arise from electric field action on the ionic double layer which will form between electrodes and fluid [16]. In addition to direct assembly under these forces, the use of various stabilization/immobilization techniques is considered for preserving assembled structures for further analysis and manipulation.

4.2 Materials and Methods

4.2.1 Colloids and Suspending Liquids

Silica colloids of various diameter ($0.32\mu\text{m}$ to $2\mu\text{m}$) were obtained from Bangs Laboratories (Fisher, IN, USA). Hydrophilic silica ($-\text{OH}$ surface functionality) was used for the bulk of this work, with amino ($-\text{NH}_2$) functionalized silica particles used for certain specific chemistries in attempts at stabilizing assemblies. Similarly, polystyrene (PS) and polymethyl methacrylate (PMMA) colloids ($0.2\mu\text{m}$ to $2\mu\text{m}$ diameter) were also purchased from Bangs Laboratories for use in experiments. All colloids were obtained in the form of aqueous suspensions, with

a volume fraction of approximately 10wt% solids in water. PS and PMMA suspensions contained small amounts of surfactant to stabilize aqueous suspensions. Suspensions were either used directly as concentrated stocks to be diluted, or centrifuged and repeatedly washed as required. Dowex beads (Sigma Aldrich) were used as ion exchange media for deionizing suspensions by removing impurity ions. Ion exchange could take place by placing a desired amount of resin in a microfuge tube and adding the liquid suspension to be deionized. Bead size was sufficiently large (\sim mm) so that separation was possible by decanting the liquid suspension using a micropipette. Deionized (DI) water was obtained using a Millipore process ($18\text{M}\Omega\cdot\text{m}$), while dimethyl sulphoxide (DMSO) and dimethylformamide (DMF) were obtained from Sigma Aldrich (Mississauga, ON, Canada). DMSO is a near index matching fluid for both silica and PMMA, allowing for suppression of van der Waals forces and potentially aiding crystallization.

4.2.2 Microelectrodes

Non-uniform AC electric fields were generated by using gold microelectrodes (200nm thick) fabricated via photolithography on a SiO_2 surface ($0.5\text{ }\mu\text{m}$ thick) deposited on top of a silicon wafer ($500\mu\text{m}$ thick). The microelectrode geometry most utilized in this work is a $100\mu\text{m}$ maximum-gap spacing set of four quadrupolar electrodes. For spreading liquids (such as DMSO on silica), a simple circular cross-sectioned well was constructed on top of the microchips using a double-sided press to seal adhesive film with a covering of parafilm. Well cross-sections were fabricated by attaching the double-sided adhesive to a strip of parafilm, followed by punching a circular hole using a $1/8''$ (3.177mm) hole punch. The well acts to provide a barrier beyond which a spreading liquid cannot pass. Complete coverage of the well could be achieved using liquid volumes of approximately $0.25\mu\text{L}$. Similar cross-section liquid wells were constructed out of 5mm thick polyisoprene sheet, with the well adhered to the chip surface again using a double-sided adhesive film. Electrical connections were made by using 4 brass connectors, held in place with screws, which were placed in contact

with each of the 4 quadrupolar microelectrodes. Alligator clips could then be attached to the brass connectors, connecting the microelectrode set to the function generator. Electrical resistance when the connectors are in good contact with the pads was on the order of 2-3 Ω . Power to the microelectrodes was supplied by a signal generator (BK Precision 4040A). The microelectrodes were connected to the source in an alternating fashion (180° phase difference between adjacent electrodes). The value of the applied voltage (V , peak-to-peak) and applied frequency (f), were monitored by an oscilloscope (Tektronix 1002B). A schematic of the experimental setup is provided in Figure 4.1, with a zoomed in optical microscopy image of microelectrode set shown in Figure 4.2 and an illustrative digital camera capture of this microelectrode set with well in Figure 4.2b).

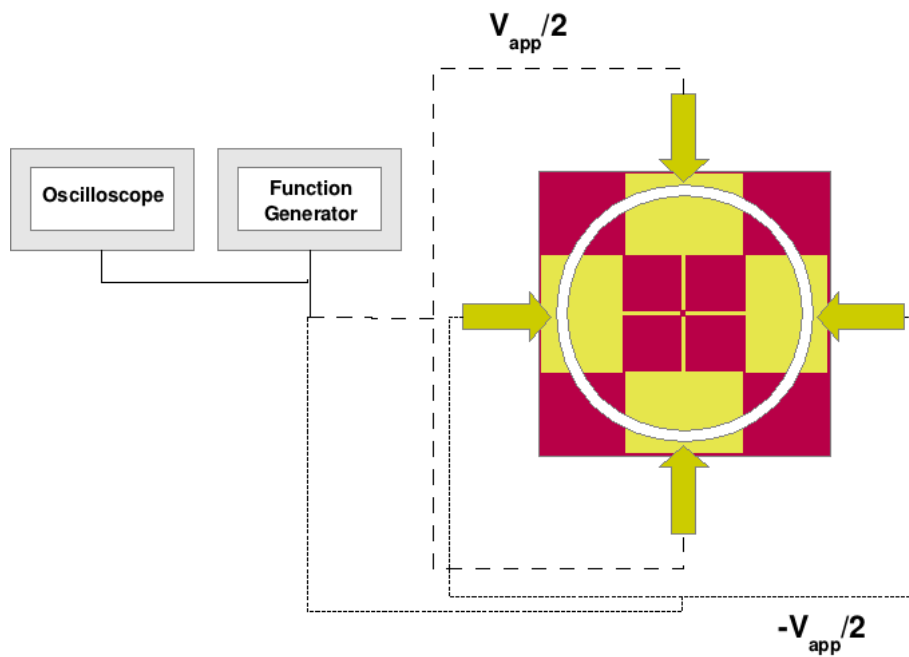


Figure 4.1: Schematic of Experimental Setup

Microchip + microwell shown connected to 4-brass connectors with an applied AC signal from a function generator applied 180° out of phase across each opposing pair of electrode pads, with voltage and frequency monitored via an attached oscilloscope

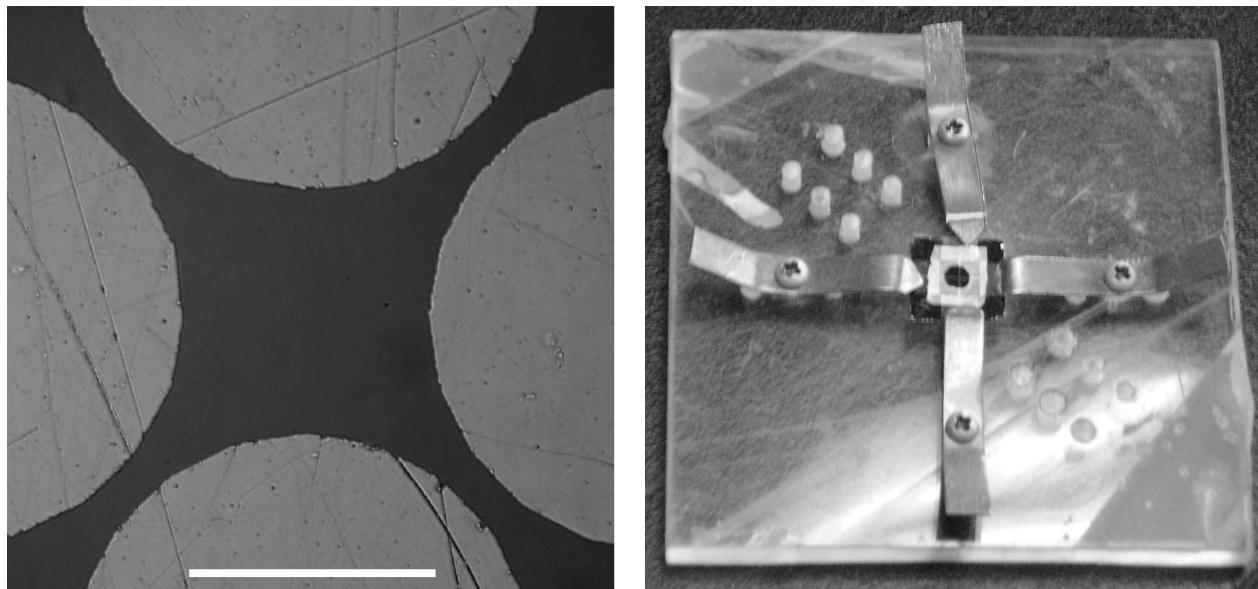


Figure 4.2: Microelectrode Images

a) Optical Microscopy image of Microelectrode Set [Scalebar is $100\mu\text{m}$], b) Microelectrodes with well on electrode stage

4.2.3 Microscopy

Observations of the assemblies in a droplet and after evaporation were performed using an Olympus BHM Microscope, with a Sony DSC-S650 Cyber-shot for digital capture of images. For SEM images of assemblies after medium evaporation, a JEOL JSM-6400 SEM system and a Hitachi S-2300 SEM system were used at various times. Samples were sufficiently conductive to obtain clear images without gold coating.

4.2.4 Zeta Potential Characterization

Zeta potential was measured using the Malvern Zetasizer Nano ZS system (Malvern Instruments Ltd.), which uses laser Doppler velocimetry and phase angle light scattering in order to determine the electrophoretic mobility of colloidal particles in suspension. From the acquired mobility data, the zeta potential (ζ) of particles in suspension can be determined.

$$\zeta = \left[\frac{3\mu_m}{2\varepsilon_m} \right] \left(\frac{U_{electrophoretic}}{E_\infty} \right) \frac{1}{f(\kappa r_p)} \quad (4.1)$$

where in eqn. 4.1, $U_{electrophoretic}$ is the electrophoretic velocity of the particle, E_∞ is the magnitude of the external electric field, ε_m is the medium permittivity, μ_m is the medium viscosity, κ is the inverse Debye length and r_p is the particle radius. f is Henry's function/correction factor, shown in eqn. 4.2, which reduces to the asymptotic values of 1 and 3/2 for the Hückel ($\kappa r_p \ll 1$) and Smoluchowski ($\kappa r_p \gg 1$) regions respectively.

$$f(\kappa r_p) = \frac{3}{2} - \frac{1}{2[1 + 0.072(\kappa r_p)^{1.13}]} \quad (4.2)$$

4.2.5 Stabilization Approaches

Cinnamoyl Chloride Linkages

Functionalized silica particles suitable for UV-crosslinking based on radical linking with cinnamoyl chloride were produced. Silica spheres, $d_p=1\mu\text{m}$, from Bangs Laboratories (Fisher, IN, USA) in water were centrifuged out at 2,500 g for 3 minutes, and re-dispersed in water, centrifuged out again. The procedure was repeated three times to remove as much of the surfactant the supplier uses to suspend particles with as possible. The sample was dried at 60°C under vacuum over night. Pyridine was refluxed with CaH_2 over night to remove any residual moisture content. The silica spheres were dispersed in freshly distilled dry pyridine. The reaction was shown as the Figure 4.3. The surface modified silica spheres were subsequently settled down by centrifugation and the sample was purified by repeated dispersed in DMF and centrifugation. Finally, the sample can be either dried under vacuum or kept in DMF. The photocrosslinking mechanism for this functionalization is shown in Figure 4.4,

with the UV source being a Jvon Horiba LabRAM system.

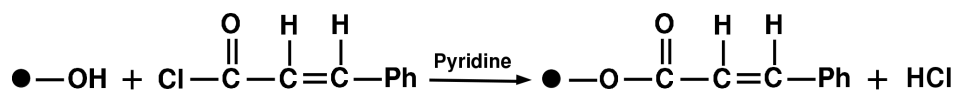


Figure 4.3: Surface Functionalization with Cinnamoyl Chloride

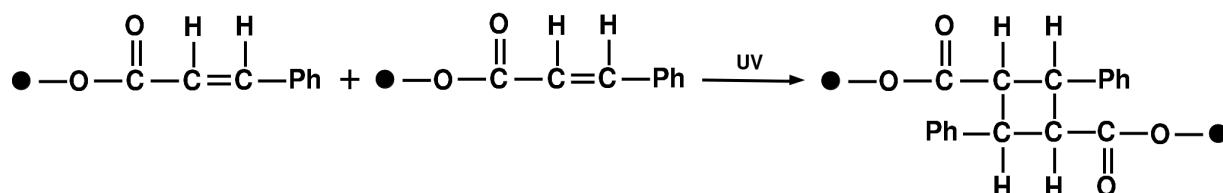


Figure 4.4: UV Crosslinking Mechanism

Streptavidin-Biotin Linkages

Functionalized silica with biotin, for use in a streptavidin-biotin linkage reaction, was synthesized. 1 μm diameter amino functionalized silica particles were obtained from Bangs (Fisher, IN, USA) and were biotin-functionalized through reaction with biotin N-hydroxysuccinimide ester in DMF (2x excess), along the lines of the procedure of Costanzo et al. (2006) [114]. The reaction was carried out for 24 hours before particles were washed twice in DMF through centrifugation (3000 RPM for 15 minutes) and decanting of the supernatant. A concentrated solution of streptavidin (8.7 $\text{mg}/\mu\text{L}$) was prepared by dissolving streptavidin powder (Sigma Aldrich Canada) in DI (millipore) water for use in linkage experiments.

Pluronic F-127 and PVA Gelation

Stock solutions of Pluronic F-127 in DMSO and DI water (10 to 20 wt%) and DMSO-water mixtures were prepared for thermal and concentration-driven gelation experiments. Solid

F-127 was obtained by donation from the BASF Corporation and dissolved in DMSO and water through use of a ultrasonicated bath at room temperature for 1 hour, followed by refrigeration (-4°C). As pluronic has temperature inverse solubility in water and DMSO (triblock co-polymer of PEO-PPO-PEO), placing the solution under refrigeration increases the solubility of F127 and facilitates dissolution of the material in the case of water. For DMSO, refrigeration was impractical as DMSO has a freezing point just below room temperature and DMSO-pluronic mixtures would similarly freeze upon sufficient cooling. Solid suspensions of particles at desired volume fractions of particles and pluronic could then be achieved through dilution of stock pluronic solutions and stock solids as required. For aqueous suspensions, sodium hydroxide NaOH was used to alter pH and adsorption properties of pluronic on silica. Gelation at room temperature takes place when pluronic concentration is approximately 30% (v/v), and can therefore be driven by medium evaporation [115].

Stock solutions of poly(vinyl alcohol) in DMSO and DI water (10 to 20 wt%) were prepared for thermal and concentration-driven gelation experiments. PVA was obtained from Sigma Aldrich and dissolved in DMSO and water through use of a ultrasonicated bath at 70°C for 12 hours. Solid suspensions of particles at desired volume fractions of particles and PVA could then be achieved through dilution of stock PVA solutions and stock solids as required. Refractive index matching solutions of DMSO-water were not suitable for PVA, as it has been demonstrated to have cononsolvency in water-DMSO mixtures but is soluble in each individual liquid [116, 117].

Photopolymerization with ETPTA and PEGMA/PEGDMA

Ethoxylated trimethylolpropane triacrylate (ETPTA) monomer with $M_N=428$ was purchased from Sigma Aldrich, Mississauga, ON, Canada along with the photoinitiator 2-hydroxy-2-methylpropiophenone (HMPP). ETPTA was added to silica-water and silica-DMSO suspensions and then the entire suspension re-sonicated for mixing. HMPP was added immediately prior to experimentation to limit the degree of photopolymerization from

ambient light.

Poly(ethylene glycol) methacrylate (PEGMA) with $M_N=360$ and poly(ethylene glycol) dimethacrylate (PEGDMA) with $M_N=550$ were purchased from Sigma Aldrich, Mississauga, ON, Canada along with the photoinitiator 2,2-diethoxyacetophenone (DEAP). Mixtures of PEGMA and PEGDMA in desired monomer (PEGMA) to crosslinker (PEGDMA) ratios and then added to stock colloidal suspensions (silica-DMSO, silica-water, PMMA-DMSO and PMMA-water) and then sonicated in an ultrasonication bath for mixing. DEAP was added immediately prior to experimentation to limit the degree of photopolymerization from ambient light.

4.3 Results and discussion

DEP assembly of particles was carried out under a variety of conditions, exploring the role of various parameters on the assembly. As expected from the Clausius-Mossotti factor calculations, for all frequencies of interest during experiments (0.1 to 2 MHz), the particles experienced negative dielectrophoresis (assembled at local electric field minima). Depending on the particle and electrolyte concentration, particle formation would be either electric field reversible (complete destruction of structure upon cancellation of field) or electric field irreversible (structure remains intact upon field cancellation). A key problem for DEP experiments was in maintaining the assembled structure upon evaporation of the medium, as the convective forces of the meniscus drying were sufficient to disrupt the assembled structures to a large degree, even if the structure would maintain upon cancellation of the electric field (irreversible formation). Consequently, a number of approaches were attempted in order to overcome this difficulty. Specifically, UV-crosslinking of cinnamoyl chloride functionalized silica, avidin-biotin linkages between biotin functionalized silica, gelation of silica colloids in pluronic F-127 and PVA, photopolymerization of PEGMA and TMPTA for immobilizing silica and chemical crosslinking of PMMA-co-AA colloids were all examined.

4.3.1 DEP Assembly

The assembly of colloidal silica in water was considered first. Building on previous work done at lower concentrations with similar sized silica in water, $1.5\mu\text{m}$ diameter silica spheres were suspended in water at relatively high concentrations (8.6wt% solids) and low (0.06wt% solids) and assembled using dielectrophoretic forces. Interestingly, it was found that the addition of a moderate amount of the polymeric surfactant pluronic F-127 did not appear to have an impact on the overall shape or size of the resulting assemblies. In Figure 4.5, the resulting images of structures for these particles are shown as a function of various voltages. As can be seen, very large assemblies can be achieved; on the order of the electrode gap spacing ($100\mu\text{m}$). For 5V, 8.6wt% solids, Figure 4.5 a), the structure formed is of an “inverse” nature. Particles are pushed away from the electrode edges only at the minimum gap spacing between electrodes, creating four symmetric “wells”. These types of structures could be used as templates or stamps for replicating patterns. As voltage increases, more particles are collected in the center between electrodes forming a more rounded shape at 10V, Figure 4.5 b), and becoming a more “diamond” like pattern at 20V, Figure 4.5 c). Assembly time was on the order of minutes, which allowed for sufficient assembly time as a 2 - 5 μL droplet at room temperature evaporated in approximately 1 hour. Upon evaporation, the assembled structure would collapse.

As an explanation as to why colloidal assemblies are so vulnerable to evaporation, consider the following. The elastic constant of colloidal crystals is on the order of 10 dyne cm^{-2} compared with atomic crystals where it is on the order of $10^{10}\text{ dyne cm}^{-2}$, meaning colloidal crystals are typically 10^9 times softer than atomic crystals [118]. This means colloidal crystals are more easily susceptible to defects and distortions, but also explains why the force of the evaporating medium coupled with loss of dielectrophoretic force leads to destruction of an assembled structure.

The use of refractive index matching, or near refractive index matching, for crystallization is well known. By matching refractive indices of particle and medium, van der Waals forces

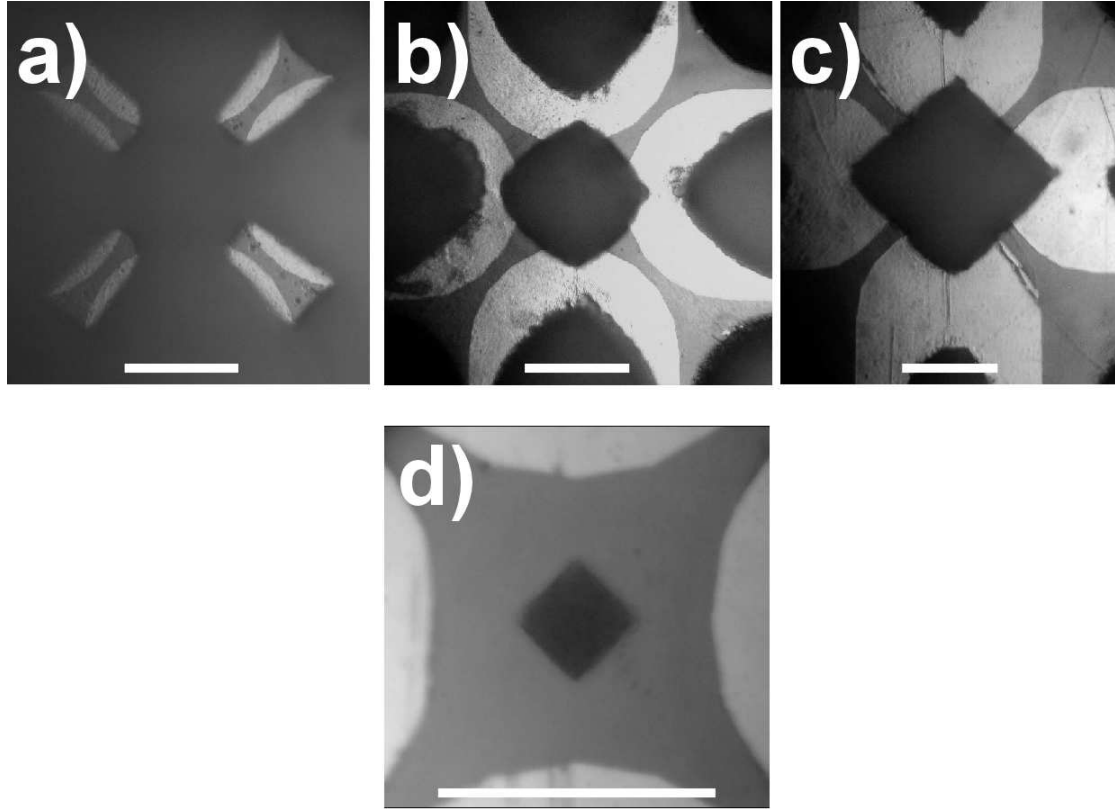


Figure 4.5: DEP Assembly of $1.5\mu\text{m}$ Silica in aq. pluronic F-127 (4wt%)
a) 5V, 8.6wt% solids b) 10V, 8.6wt% solids c) 20V, 8.6wt% solids and d) 20V, 0.06wt% solids [scalebar is $100\mu\text{m}$]

are suppressed. This methodology is well known for producing colloidal crystals in other methods and has been applied to the colloidal crystallization by electric fields generated by parallel electrodes [119]. Silica and DMSO are near index matched materials, with sufficient contrast between particle and medium to still allow for visualization by optical microscopy. The results for the DEP assembly 0.1vol% silica in DMSO are shown in Figure 4.6.

As can be seen, changing the voltage leads to a large change in the assembly shape and size. Shifting from 2.5V to 20V yields shapes ranging from “square”-like, rounded inwards along the edges, to a rounded “diamond” like structure. Beyond 2.5V, all structures formed were multilayered, which makes direct determination of the structure outside of the assembly

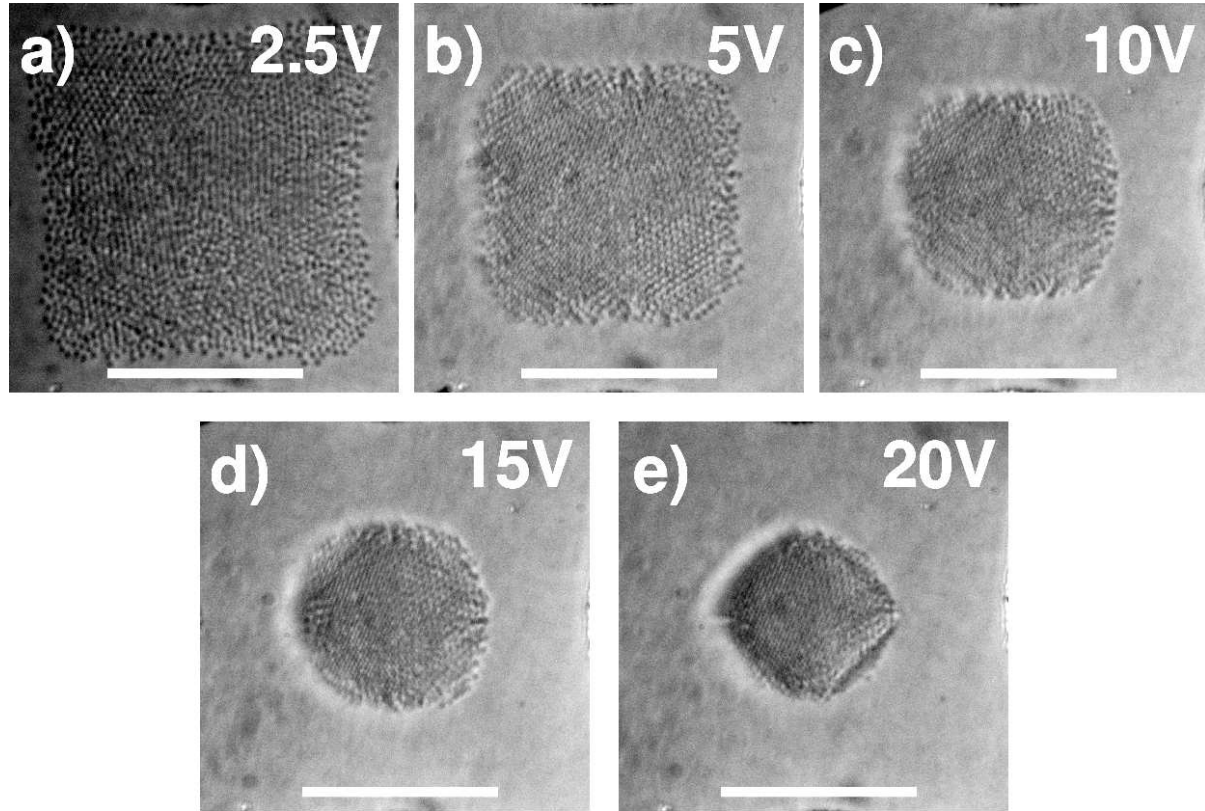


Figure 4.6: DEP Assembly of $2\mu\text{m}$ Silica in DMSO at 1MHz, $c_0=0.1$ vol.%, $0.5\mu\text{L}$ droplet
a) 2.5V, b) 5V, c) 10V, d) 15V and e) 20V [scalebar is $50\mu\text{m}$]

edges difficult. From examining the assembly edges it is clear that the particles have chained and these chains have aligned themselves into groups as part of the overall structure. The chaining force arises from induced dipole-induced dipole interactions, with the translational force being dielectrophoresis. The effect of solids content was also examined by reducing the volume of pipetted droplet. This was done by pipetting a thin layer to cover the well area, through pipetting a $0.5\mu\text{L}$ droplet and then re-uptaking material so that only a thin film of liquid remained behind. As can be seen from comparing Figure 4.6 to Figure 4.7, there is a shift in the shape and size behavior at different voltages. For the smaller droplet volume, the structures formed are more rounded compared with the results from larger droplets (at the same voltage). Additionally there are fewer particle layers which result, although they are

still multilayered structures. Visualizing structures in the smaller volume case, Figure 4.7, is also more difficult and was not possible at voltages less than 5V. Reproducing the liquid level for these experiments was challenging, but not impossible. Structures again show evidence of being composed of 1d chains of particles which have combined under the influence of induced dipole-induced dipole forces (mutual DEP) and been shaped by induced dipole-electric field forces (DEP), although optical microscopy images at the edges of structures to examine this are less clear for the larger droplet case due to the presence of additional particle layers.

Based on zeta potential measurements of silica and polystyrene spheres in water, with the conditions shown in Table 4.1 and results in Table 4.2, the coexistence line for disorder-ordered transition without an applied electric field was calculated as per the hard-sphere perturbation method described in Russel et al. (1991) at different salt concentrations [39] (code for this methodology is provided in Appendix 1).

Run	d_p (μm)	ϕ	c_{KCl} (M)	wt.%F-127	κ^{-1} (nm)	f_{Henry}
Silica A	1.5	3.0×10^{-3}	0	0	1000	1.05
Latex A	1.98	3.4×10^{-3}	1×10^{-5}	0	96.5	1.25
Latex B	1.98	3.4×10^{-3}	1×10^{-5}	10^{-3}	96.5	1.25
Latex C	1.98	3.4×10^{-2}	5×10^{-5}	10^{-2}	43.2	1.36

Table 4.1: Particle Zeta Potential Measurements: Conditions

Run	η_{elec} ($\frac{\mu\text{m} \cdot \text{cm}}{\text{Vs}}$)	ζ (mV)
Silica A	-2.97 ± 0.05	-62.3 ± 0.9
Latex A	-3.51 ± 0.30	-59.2 ± 5.0
Latex B	-1.65 ± 0.07	-27.9 ± 1.1
Latex C	-1.2 ± 0.1	-18.6 ± 0.7

Table 4.2: Particle Zeta Potential Measurements: Results

For $1.98 \mu\text{m}$ PS beads at $5 \times 10^{-7} \text{M}$ KCl, the critical volume fraction of transition was 1.7×10^{-3} and for $1 \times 10^{-6} \text{M}$ was 5.3×10^{-2} . Suspensions at these salt concentrations and volume fractions were then prepared so that even without the presence of an electric field, the system

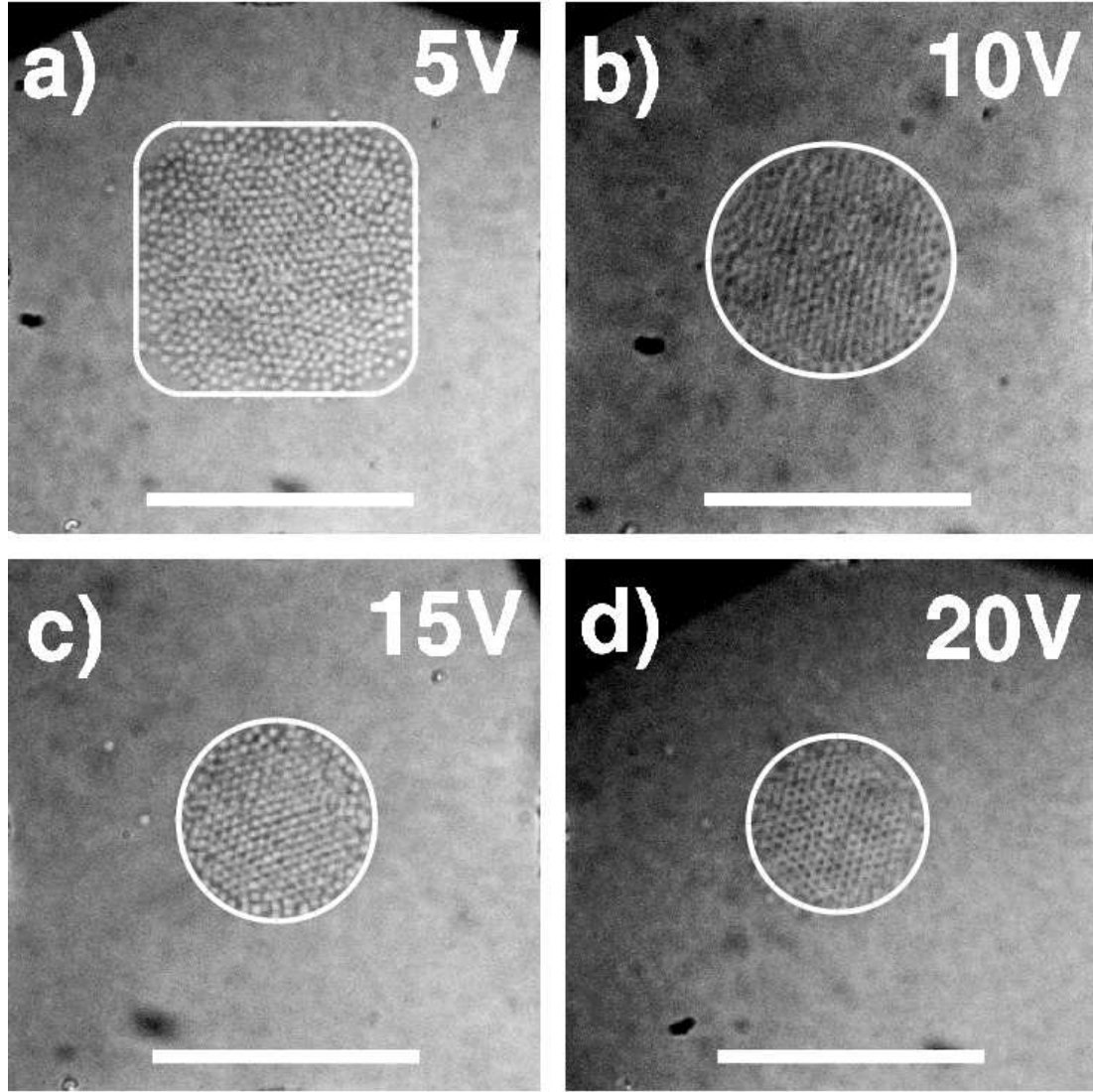


Figure 4.7: DEP Assembly of $2\mu\text{m}$ Silica in DMSO at 1MHz , $c_0=0.1\text{ vol.}\%$, min. well volume
 a) 2.5V , b) 5V , c) 10V , d) 15V and e) 20V [scalebar is $50\mu\text{m}$]
 (a white outline around the structure is provided for visualization purposes)

would be on the verge of a phase transition/two-phase equilibrium. Salt concentrations were chosen at very dilute values to attempt to mitigate the influence of electrothermal flows on assembly structure. The results from PS experiments are shown as representative results of all tests done based on choosing the initial volume fraction at the onset of a phase transition.

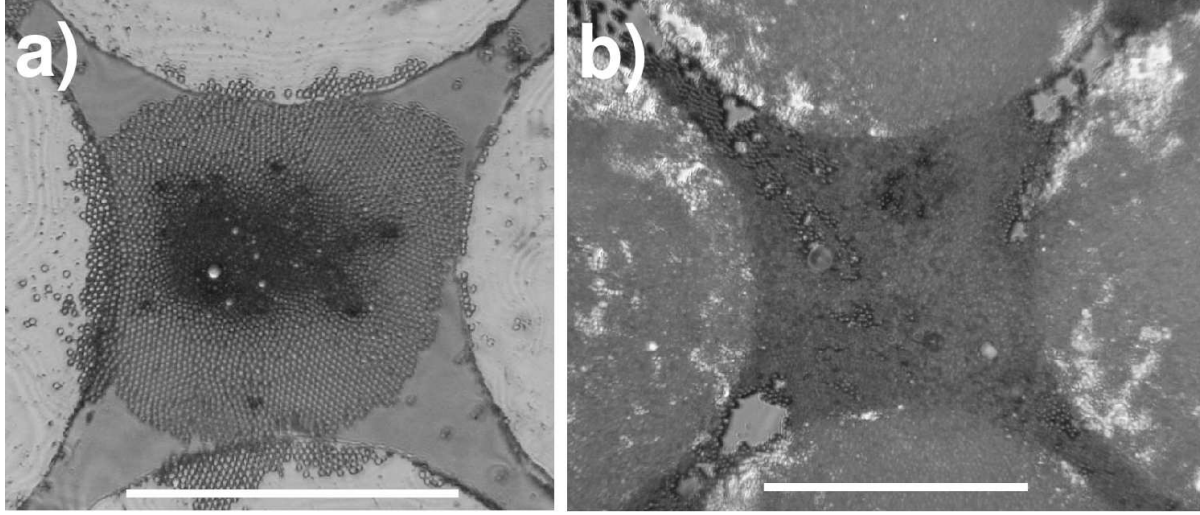


Figure 4.8: 1.98 μm Latex Assembled at 20 V, 1 MHz
 a) $5 \times 10^{-7}\text{M}$ KCl, 0.17 vol.% solids b) $1 \times 10^{-6}\text{M}$, 5.3 vol.% solids [scalebar is $100\mu\text{m}$]

In Figure 4.8 the results for both low salt, low solid, and higher salt, higher solid, cases are shown after medium evaporation. In both cases, even the small concentration of salt did lead to some degree of electrothermal flows based on observation of particles moving in fluid rolls near electrode edges. The structure maintained a large degree of stability after field cancellation but after contact with the meniscus the structure was shattered and spread out into the resulting collapsed structure shown in Figure 4.8. Work with smaller particles (320nm) yielded similar results in terms of stability of assemblies, with the additional result of red-shifting of incident white light from the microscope due to the colloid size and ordering before and after evaporation. Based on these results, the need for immobilizing the structure through either “freezing” the medium or linking assembled particles is clear.

4.3.2 DEP + EO Assembly

The influence of tuning frequency on the assembly shape and size was examined by reducing applied frequency from 1MHz to 100kHz. This has a negligible impact on the dielectrophoretic forces based on analysis of the Clausius-Mossotti factor (dipole coefficient) but

does introduce the electroosmotic flows to the system. Examining at analogous conditions to DEP-only driven assembly cases in silica-DMSO, the results are shown for a $0.5\mu\text{L}$ droplet and the “min” volume case in Figures 4.9 and 4.10 respectively, the influence of electroosmotic flows is clear. For both droplet sizes, the presence of electroosmotic flows causes assembled structures to be more “diamond” like at earlier voltages, with the effect becoming more pronounced as voltage is increased. For dielectrophoretic assembly at 10V (1MHz case), the assemblies formed are circular/rounded shapes as seen in Figures 4.6c) and 4.7c). For dielectrophoretic and electroosmotic assembly at 10V (100kHz case), the assemblies are clearly “diamond” shaped for both volumes as can be seen in Figures 4.9 and 4.10c). Even for the 5V case, b) in all representative figures, the 100kHz cases shown evidence that flows are causing the structure to “bow” inwards, beginning to show formation of the more diamond-like structures, compared to the more rounded structures found at 1MHz. For all cases, the presence of chained particles is clear from examining the edges of assembled structures. The mechanism of electric-field induced assembly is well known to begin with particles chaining together under the influence of induced dipole-induced dipole forces, with chains then being attracted to each other and forming larger structures. In this case, chains are attracted to each other through electric field-induced dipole interaction forces (dielectrophoresis) and electroosmotic flows driving the chains towards the electrode center, where they form the larger structures shown in Figures 4.9 and 4.10.

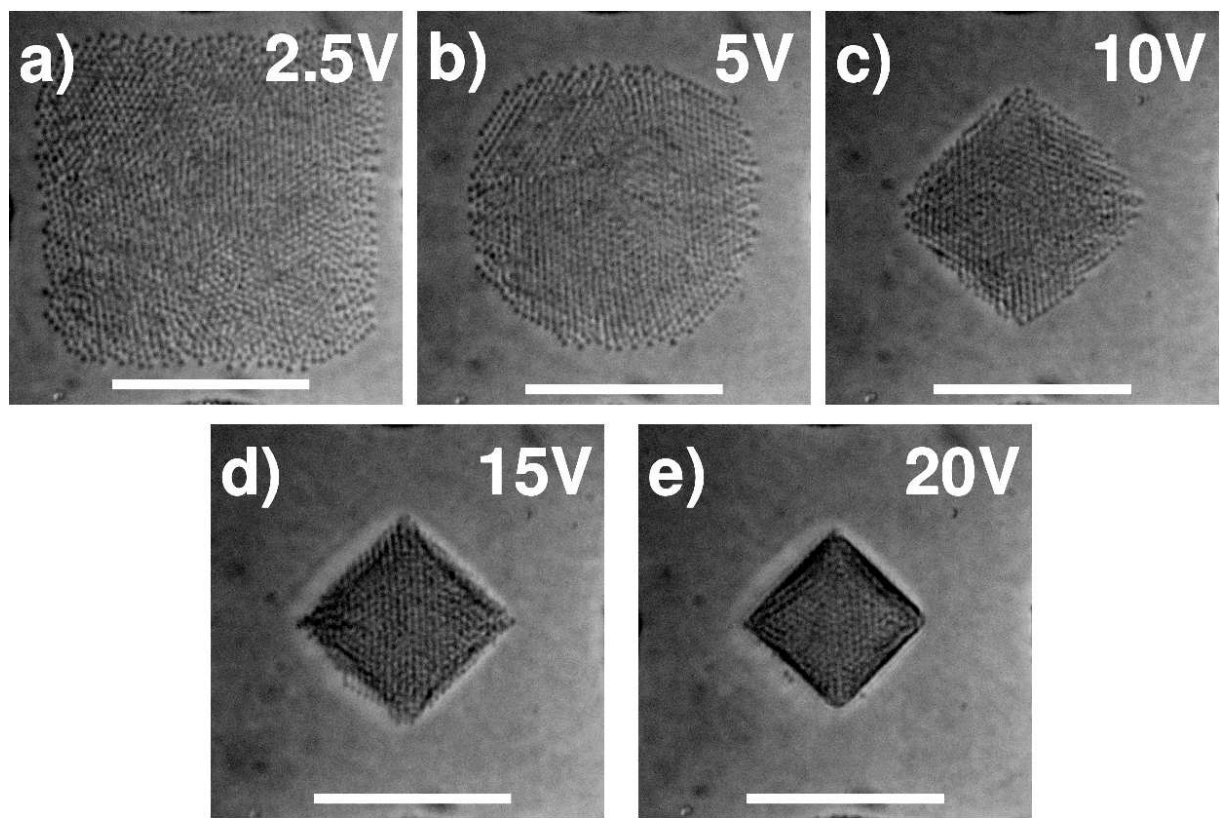


Figure 4.9: DEP Assembly of $2\mu\text{m}$ Silica in DMSO at 100 kHz, $c_0=0.1$ vol.%, $0.5\mu\text{L}$ droplet
a) 2.5V, b) 5V, c) 10V, d) 15V and e) 20V [scalebar is $50\mu\text{m}$]

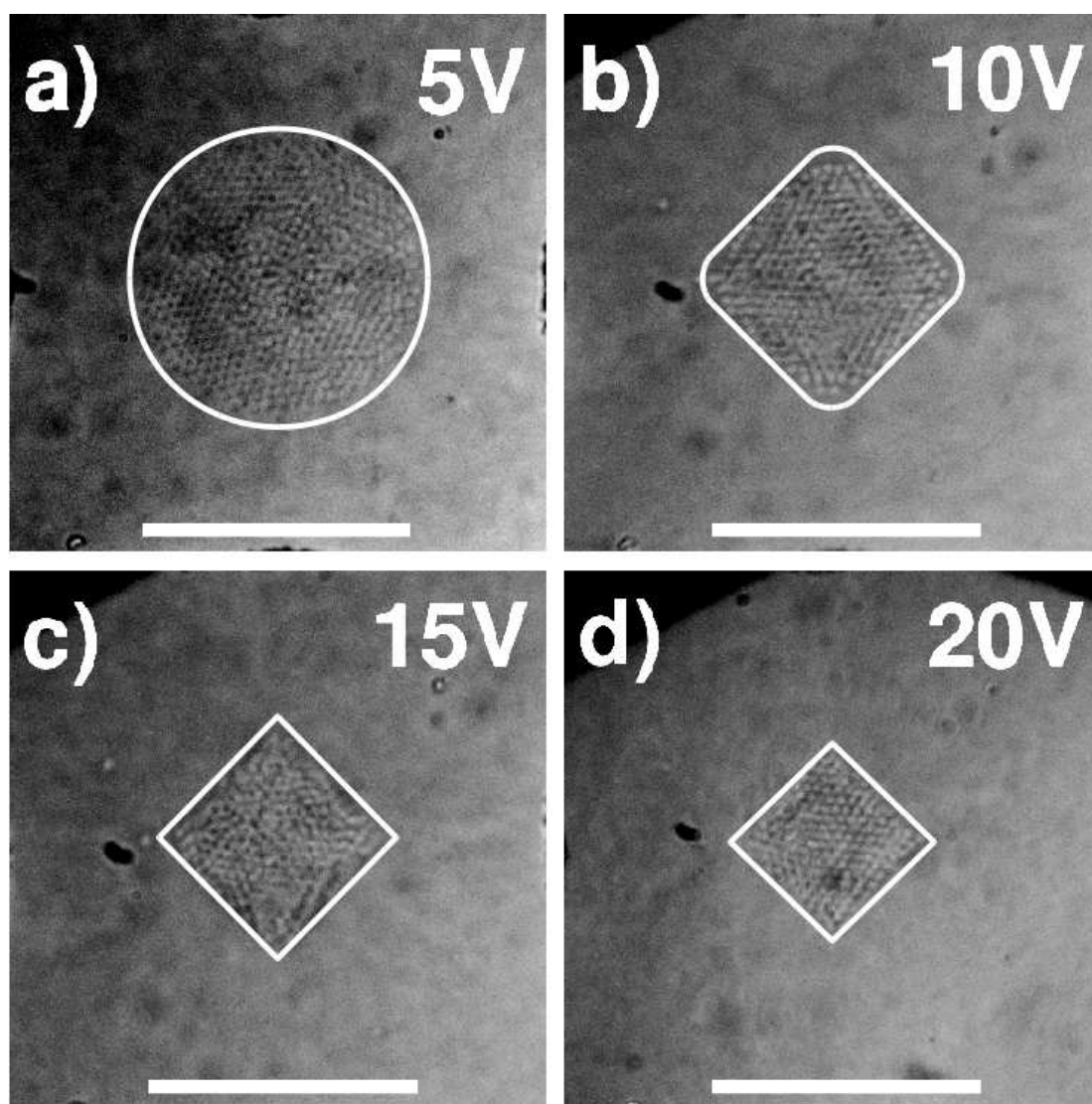


Figure 4.10: DEP Assembly of $2\mu\text{m}$ Silica in DMSO at 100kHz , $c_0=0.1\text{ vol.}\%$, min. well volume

a) 2.5V, b) 5V, c) 10V, d) 15V and e) 20V [scalebar is $50\mu\text{m}$]
(a white outline around the structure is provided for visualization purposes)

Use of lower frequencies also allows more direct visualization of the formation of particle chains as they travel toward the dielectrophoretic trapping center, although chains of particles are still visible on the edges of the previously shown assembled structures. As an illustration of this, the assembly of $1.5\mu\text{m}$ PMMA colloids in DMSO at 7V and 1kHz is shown in Figure 4.11. The presence of chains transitioning into a larger structure is quite clear from examining this figure. This is possible as fluid flows help to induce chain formation at locations farther away from the center of the electrode system compared to using dielectrophoresis alone. Although the chaining phenomena is itself a result of induced dipole-induced dipole interactions between particles (so-called mutual dielectrophoresis), electroosmotic flows tend to transport particles in a manner to promote formation of these chains at a greater distance from the electrode center. Formation of chains and these chains integrating into larger structures (2d crystals or 3d aggregates) is a well known phenomena of electric-field induced assembly of colloids into structures and has been observed previously in the assembly of colloidal aggregates, 2d colloidal crystals, electrorheological fluids and magnetorheological fluids [13, 31, 40, 86, 96, 110, 120–125]. These cases mainly involve parallel spaced planar electrodes (or magnetic equivalents) but the underlying physics is identical.

Similar to the results of using pure dielectrophoresis for assembly, without some additional modification of the system (salt or DC bias for example), all assemblies were electric field reversible. That is, upon cancellation of the field structures would break apart via diffusion, although depending on how concentrated the assembly was this could be a slow process. Similar to the 1MHz case, upon contact with the meniscus during medium evaporation, any resulting structures would be destroyed. As such the use of various stabilization techniques to maintain structures upon medium evaporation for further manipulation and analysis, by SEM for example, was considered.

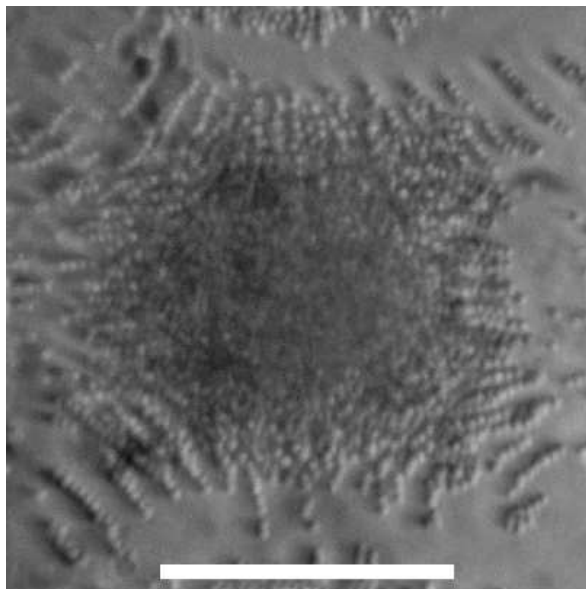


Figure 4.11: DEP Assembly of $1.5\mu\text{m}$ PMMA in DMSO at 7V, 1kHz
[scalebar is $50\mu\text{m}$]

4.3.3 UV-Crosslinking of Structures

DEP assembly of cinnamoyl chloride functionalized silica particles was attempted at a variety of voltages (2 to 20 V) and frequencies (0.1 to 1 MHz) for particles suspended in DMF and in water. In the case of DMF, assemblies would not hold upon cancellation of the field irrespective of the UV exposure time. After subsequent analysis, it was found that DMF absorbs UV in the range of interest for this reaction (230 - 290 nm). For water, the structure was roughly retained upon removal of the field, but with a distinct degree of collapse. Dispersion of the functionalized silica particles in water was difficult, suspensions would begin to aggregate rapidly although experiments could be run over the time-scale of dielectrophoretic assembly (minutes). DMSO/water and THF/water mixtures were also tried as suspending liquids (at 50/50 v/v ratios) and in both cases the particles dispersed well based on optical microscopy observations but showed no significant crosslinking or retention of the structure after medium evaporation. Some representative SEM images of the remaining

structures are shown in Figure 4.12.

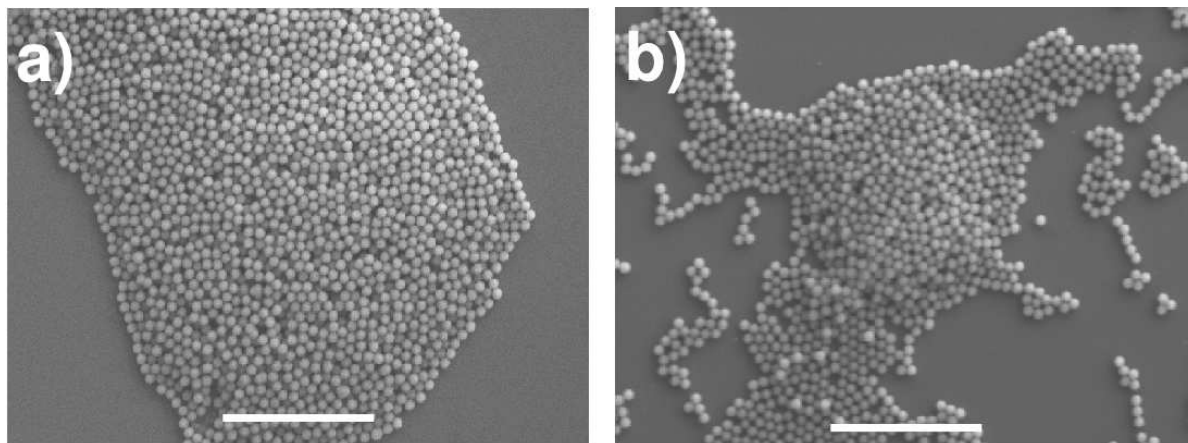


Figure 4.12: Representative SEM images of $1.5\mu\text{m}$ cinnamoyl chloride functionalized silica DEP Assembly

[scalebar is $20\mu\text{m}$]

It is postulated that UV light can only really penetrate to the surface layer of particles, and this proved insufficient for maintaining any formed structures as is evident from examination of SEM images for $1.5\mu\text{m}$ silica assembled using DEP at 20V, 1 MHz and 0.06 wt% solids concentration in distilled water. Even for these assemblies which are at most 3 or 4 particle layers thick at reaching steady-state after applying the electric field, UV direct crosslinking of particles using particles functionalized with cinnamoyl chloride was not successful for stabilizing any structures in this work.

4.3.4 Stabilization with Biotin-Streptavidin Linkages

As a control test, the biotin functionalized silica particles were assembled using the $100\mu\text{m}$ quadrupolar microelectrodes shown previously at 20 V (peak-to-peak) and frequencies ranging from 0.1 to 1 MHz. At 100 kHz, the particles formed a structure which would retain at least partial coherence after cancellation of the electric field, indicating that the particles had at least aggregated. After the evaporation of the medium, the structure broke apart and

was not retained so merely functionalizing with biotin would not be effective for stabilizing a structure. No structure was formed at higher frequencies, indicating that the effect of electroosmosis (EO) dominated versus dielectrophoresis since 100 kHz is the cutoff frequency below which EO flow becomes significant. As another control, the effect of different ways of adding streptavidin to the particle suspension was investigated (no electric field effects). Two different types of approaches were attempted for avidin addition: i) mixing streptavidin solution and particle suspension and then applying an electric field to assemble particles; and ii) allowing the particles to assemble under the influence of the field and then pipetting streptavidin solution into the droplet to try to form linkages. The first approach had small, irregular clusters of particles forming, an indication of some linkages or aggregation occurring while the second approach yielded very large irregular structures. After these results, it was clear that the first approach was more practical for linkages, as adding an extra volume of fluid to the existing droplet caused large gradients in velocity which were very disruptive, although both were attempted for DEP assembly. Although the biotin-avidin linkage has been demonstrated successfully for linking a number of nanoparticles, it was found to be unsuitable when attempting to take advantage of electrokinetic effects for assembly based on this work [114, 126].

4.3.5 Gelation using Pluronic F-127 and PVA

After the failures of using either UV-crosslinking or biotin-avidin linkages to stabilize structures, the use of pluronic F-127 as a gelation agent was tried. This system undergoes reverse thermal gelation, meaning that it will gel as temperature increases due to aggregation of micelles, and at weight fractions of approximately 30% this transition will occur at room temperature [115]. Since the gelation will occur naturally as the droplet evaporates, this approach was deemed ideal for increasing the medium viscosity for minimizing meniscus driven flow effects during evaporation, “freezing” a structure in place upon gel formation. After gelation, pluronic could be removed by use of UV-ozone (4 to 5 hour treatment) without

effect on the assembled structure (as assessed by optical microscopy). Removal of the surfactant via annealing (8 hours in an oven at 400°C, with a 10°/min ramp up and down) was also investigated, although found to be more disruptive for structures compared to UV-ozone treatment.

The optimum F-127 concentration is system specific, in that a minimum gel height is needed to completely encapsulate the structure but addition of more pluronic will change the medium viscosity and interfacial parameters so the size of structure can change with surfactant concentration. After performing DEP experiments ranging from 2 to 20 V and 0.3 to 5 MHz in varying solids concentration suspensions of silica (0.06 to 8.6 wt%), it was found that a pluronic concentration of between 3 to 4 wt% initially was sufficient in order to maintain the overall geometric structure of an assembly. 5 - 20 μ L droplets were pipetted, with no real effect of droplet volume on the assembly process observed when using pluronic to gel. SEM images of representative assemblies of 1.5 μ m silica are shown in Figures 4.13, 4.14 and 4.15, which show the overall assembly, a zoomed view of assemblies on a 45° tilt and a representative snapshot of the assembly microstructure respectively. As mentioned, optical microscopy images of assemblies before and after gelation were fairly indistinguishable (see Figure 4.5).

As can be seen from the displayed figures, a number of interesting overall assembly geometries are possible even at a single operating frequency just by changing either solids concentration or applied voltage. The use of pluronic as a gelation agent to freeze structures was very effective, as is evidenced by optical microscopy pictures and SEM images. However, the disadvantage of using pluronic is also evidenced from these images. While the assembly obtained an overall geometric shape and this shape was retained during the medium evaporation, the use of such a large surfactant concentration in the medium inhibited the disorder-order transition and no crystalline lattices were formed in any of the performed experiments. Lowering the concentration of pluronic would also mean that the size of structure which could be protected during the evaporation would be decreased and

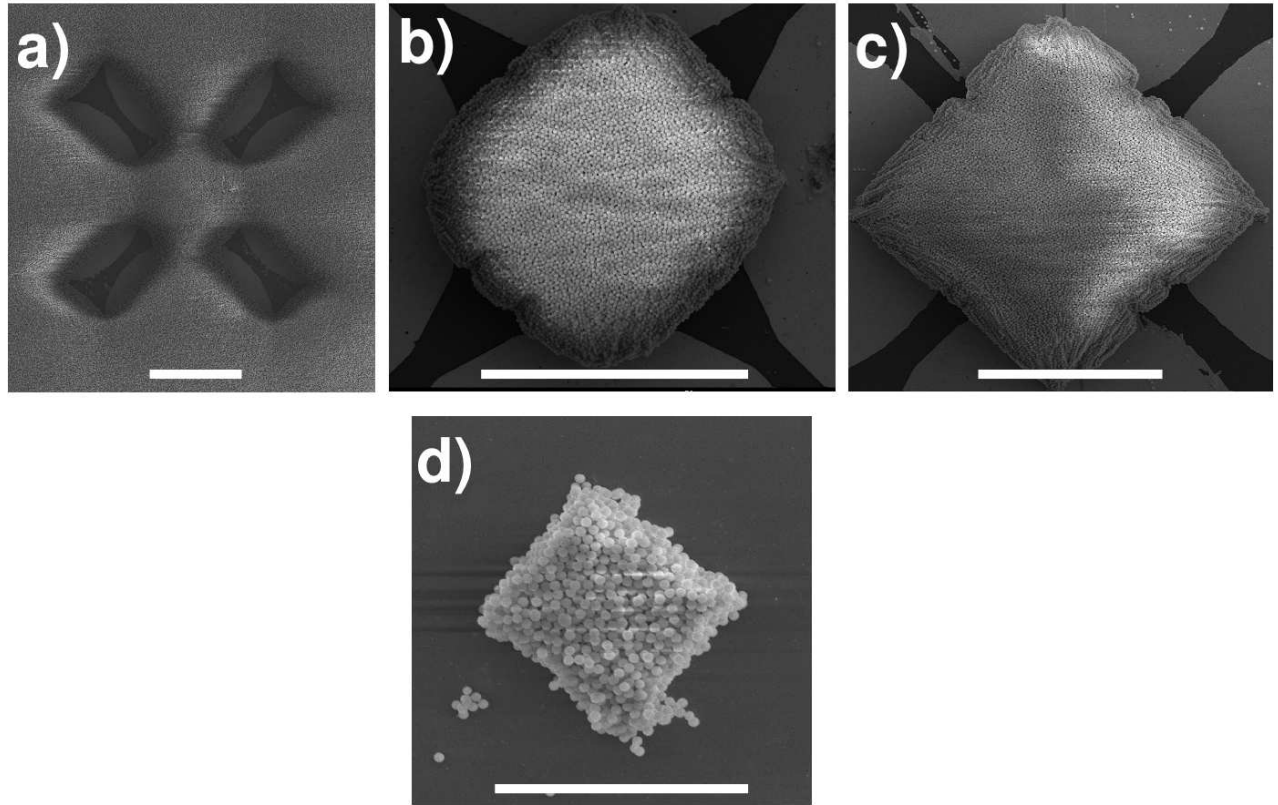


Figure 4.13: SEM images of DEP Assembly of $1.5\mu\text{m}$ Silica in aq. pluronic F-127 (4wt%) a) 5V, 8.6wt% solids b) 10V, 8.6wt% solids c) 20V, 8.6wt% solids and d) 20V, 0.06wt% solids [scalebar is $100\mu\text{m}$]

based on zeta potential measurements, there is a strong indication that even extremely low pluronic concentrations will have a very large effect on the colloidal forces involved in the crystallization process (decreased magnitude of zeta potential/electrophoretic mobility by a factor of 4 at 0.1wt% pluronic).

To attempt to remedy the surfactant adsorption on the surface of silica particles and its possible inhibition of forming structures possessing a larger degree of colloidal ordering, the use of sodium hydroxide in aqueous solutions of pluronic was considered. Concentrations of NaOH on the order of 10^{-3}M have been shown in previous experiments to reduce the degree of adsorption of pluronic on silica drastically and consequently this was done to see

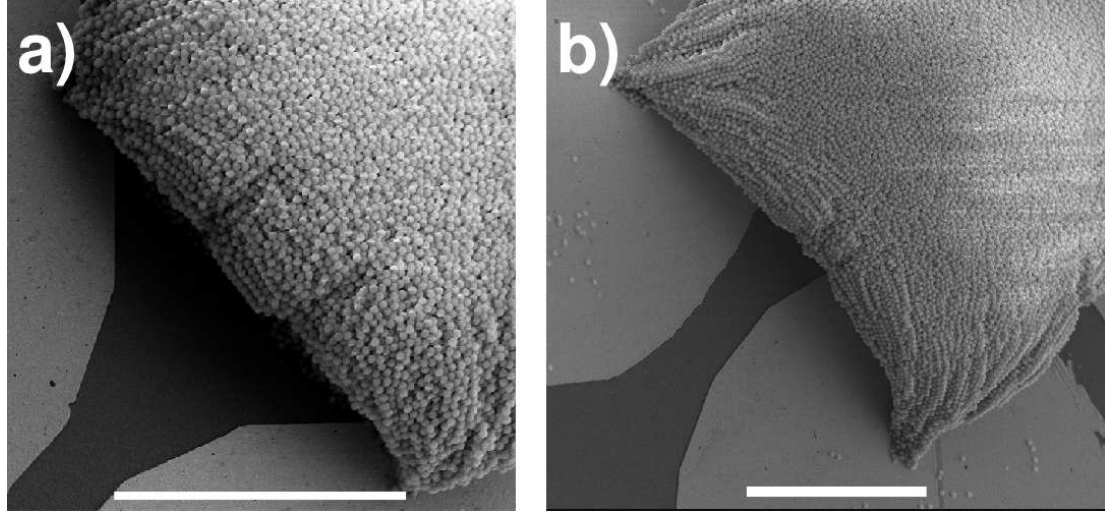


Figure 4.14: Zoomed SEM images of DEP Assembly of $1.5\mu\text{m}$ Silica in aq. pluronic F-127 (4wt%)

a) 10V, 8.6wt% solids and b) 20V, 8.6wt% solids [scalebar is $50\mu\text{m}$]

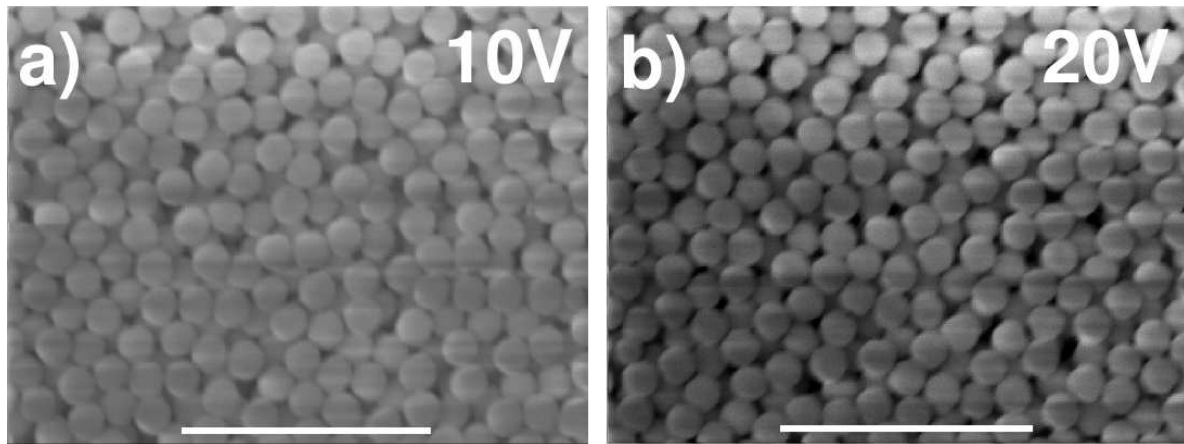


Figure 4.15: Microstructures for DEP Assembly of $1.5\mu\text{m}$ Silica in aq. pluronic F-127 (4wt%)

a) 10V, 8.6wt% solids and b) 20V, 8.6wt% solids [scalebar is $10\mu\text{m}$]

what effect it would have on the resulting assembled structures [127]. Both UV-ozone and annealing were considered with and without salt for silica assembly of 0.1% (by vol.) silica in 4 wt% aq. pluronic with and without $1 \times 10^{-3}\text{M}$ NaOH. The resulting structures after drying and medium removal are shown in Figure 4.16.

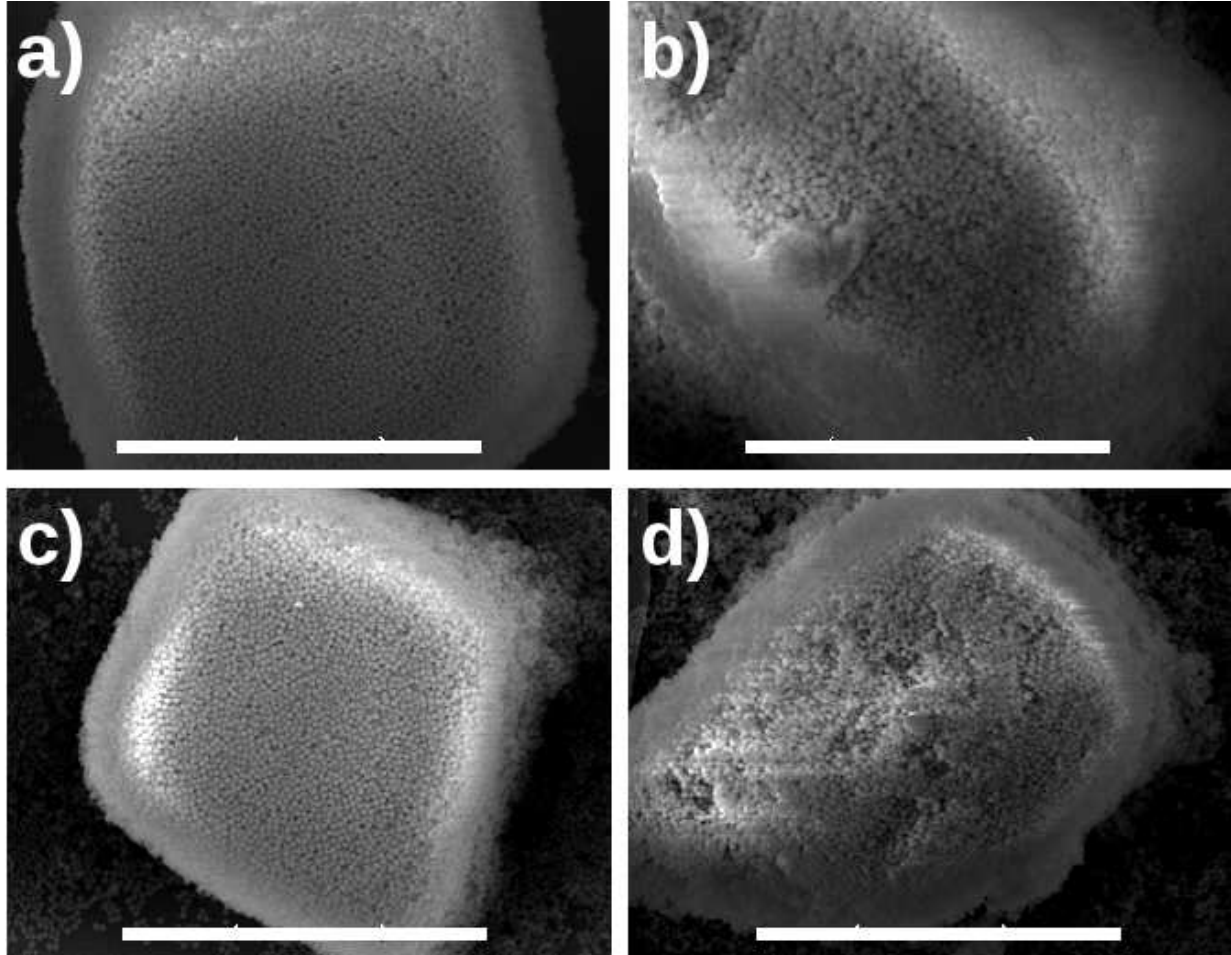


Figure 4.16: DEP Assembly of $1.5\mu\text{m}$ silica in aq. pluronic F-127 at 15V, 1MHz
 a) UV-ozone, no NaOH, b) UV-ozone, 10^{-3}M NaOH, c) Thermal Annealing, no NaOH, d) Thermal Annealing, 10^{-3}M NaOH [scalebar is $50\mu\text{m}$]

As can be seen from Figure 4.16, UV-ozone was less damaging to the overall structure, there was no noticeable deviation before gelation to final SEM imaging while for heat treatment removal of the film there was a shift. Further optimization of the heat treatment procedure could possibly eliminate this but the simplicity of using UV-ozone outweighed any further investigation. Using sodium hydroxide in solution did not lead to any shift in the colloidal ordering of the structure, in fact it led to the creation of more randomly shaped structures (even before gelation). Based on the observed experimental results, it is concluded

that the following happened: increasing the salt concentration increased the electrical conductivity of the medium significantly, to the point where electrothermal flows were significant. These flows were significant in comparison with the magnitude of dielectrophoretic forces and increased as water evaporated during the assembly process, which continually increased the effective concentration of ions in the system, leading to larger temperature gradients and still larger fluid flows. Due to the sharp dependence on the evaporation profile, the resulting structures were fairly random when compared with each other, owing to small differences in initial pipetted volume or ambient humidity having a larger impact on the evaporation rate/ion concentration versus time. Working at more dilute NaOH concentrations initially did not appear to improve the quality of the resulting assemblies or eliminate any randomness, which is similar to the result found from using KCl with polystyrene colloids shown previously. Work done without added NaOH however was quite reproducible, with very small deviations (order of 1-2 particles thickness) discerned from SEM images, although the pluronic solution does possess a low conductivity resulting from ionic impurities in the surfactant ($\sigma_m \sim 5\text{mS/m}$).

Overall, pluronic is an exceptionally effective means of gelling/freezing an assembled structure in place while having minimal disruption compared with the case of assembly in pluronic-free liquid. Starting from a desired low pluronic concentration, an electric field is applied and assembly occurs. Evaporation of droplets proceeds on a much slower time frame or can be eliminated using a covered-well. As the medium evaporates, the pluronic concentration in solution rises until it eventually surpasses the critical micellization concentration and the suspension will gel. The ability to retain structures of various sizes can be tuned by changing the initial pluronic concentration, through temperature control or direct control of evaporation rate. Removing pluronic films to obtain an assembly can be readily accomplished using UV-ozone treatment, although for the case of polymeric colloids this may not be a viable option due to potential UV-ozone degradation of particles. Based on cleaning studies attempting to remove PS and PMMA spheres from the surface of chips, the

degradation time of polymer colloids is much greater than that of pluronic F-127. Therefore this method may be potentially effective even when considering the case of polymeric colloids, but this has not yet been tested experimentally.

PVA immobilization was attempted using a similar methodology to that of pluronic F-127. Immobilization proved far less effective at similar or higher weight fractions of PVA in water (or DMSO) compared pluronic. One possible explanation for this was the high electrical conductivity of PVA solutions, leading to disruptive electrothermal fluid flows, but treatment using ion exchange resins did not eliminate these difficulties. PVA has been successfully used for immobilizing two-dimensional structures in combination with avidin-biotin linkages so it is possible that combining PVA immobilization with some other stabilization technique would be effective, however this was not explored during this work [128].

4.3.6 Stabilization by Photopolymerization

As pluronic F127 was successful at stabilizing structures but inhibited formation of an ordered phase in assemblies, the use of other polymeric monomers that would allow for ordered assemblies to occur was investigated. In previous experimental work, it has been possible to immobilize large colloidal crystal arrays within a hydrogel formed from photocrosslinking PEGMA/PEGDMA or ETPTA [129–134]. These colloidal crystal arrays demonstrate photonic properties which can be shifted with additional treatment (swelling agents, thermal treatment, etc.). Consequently, the use of these compounds for immobilizing the assemblies in this work was explored.

1 μ m silica was suspended in a water-PEGMA-PEGDMA mixture at various concentrations of PEGMA/PEGDMA in water, ranging from 5wt% PEGMA in water to closer to 40wt%. Aggregation of silica suspensions was an issue and PMMA, which is hydrophobic versus the hydrophilic silica used in this work, also showed some aggregation issues. Ion exchange was attempted for crystallization purposes, but lead to rapid aggregation of suspensions possibly due to loss of stabilizing electrostatic repulsion forces. Silica-DMSO and

PMMA-DMSO systems were also used for photopolymerization experiments. In all prepared suspensions, stabilizing a final structure proved challenging and only a partial structure was retained upon final completion of the UV polymerization. In cases where aggregation was minimized, the initial assembled structure resembled that found in aqueous suspensions or that of aqueous pluronic suspensions for a given voltage. After photopolymerization, this was not the case. A possible explanation for this is the intensity of the polymerization front (and loss of dielectric contrast between medium and particle with polymerization) was sufficient to significantly distort any assembly. Specifically, the direct force of the polymerization front, temperature gradients associated with the front inducing fluid flows and the chaotic nature of the front itself causing electric field gradients could have all combined to lead to the observed distortion in the assembly [135]. These types of effects would be mitigated in colloidal crystal arrays as they are much larger assemblies (immobilized crystals in hydrogels up to cm^2 in area) and for using gravity as the primary motive force for driving colloid motion. UV-ozone treatment of films was not practical, annealing was required. As mentioned in the previous discussion on pluronic F-127 gelation, annealing is more disruptive versus UV-ozone or at least was at the treatment conditions used. However, in this case significant damage to assemblies was done before heat treatment.

When using ETPTA, mixed with either water or DMSO, an emulsion seemed to form in the presence of particles. This is possibly a pickering emulsion, although it may just be that adding particles increased the optical contrast in the system and made it easier to visually identify the “oil” phase of the emulsion. This emulsion made stabilizing particles (silica or PMMA) difficult but depending on the amount of ETPTA, suspensions could be stable for up to 30 minutes. Stabilization using ETPTA was unsuccessful, as for PEGMA/PEGDMA. The reasoning behind this is likely similar to that postulated for PEGMA/PEGDMA, with the added effect that the “oil” phase of the emulsion has a very similar permittivity to that of silica or PMMA and therefore will experience a similar dielectrophoretic force moving it towards the center of the electrodes. Upon reaching this center, the “oil” phase is now the

medium which trapped particles are suspended in and given the lack of dielectric contrast, particles would diffuse away and any assembled structure would be destroyed. This was visually observed by optical microscopy for ETPTA-water and ETPTA-DMSO systems, with a representative SEM of ETPTA stabilization experiments at 20V, 1MHz for $1\mu\text{m}$ silica in DMSO provided in Figure 4.17. Once again, for larger colloidal crystal arrays assembled by gravity/sedimentation, this phenomena would not be relevant. Heat treatment was required to remove ETPTA for SEM imaging, as was the case for PEGMA/PEGDMA, and again the disruption/lack of structure occurred prior to heat treatment.

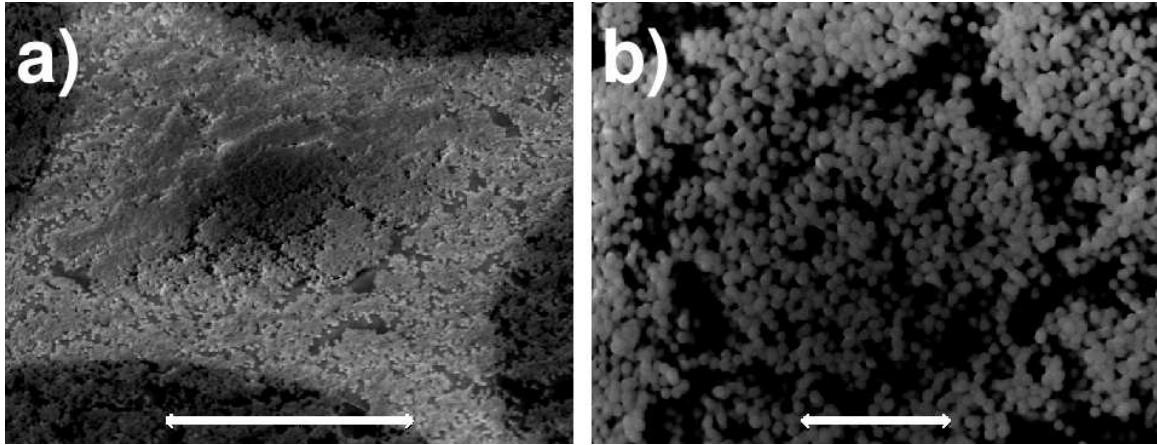


Figure 4.17: SEM of DEP Assembly of $1\mu\text{m}$ silica in 95/5 (v/v) DMSO/ETPTA at 20V, 1MHz

a) 60° tilt Overview [scalebar is $50\mu\text{m}$, b) Top-Down Zoomed View of Local Microstructure [scalebar is $10\mu\text{m}$]

4.4 Conclusions

The use of non-uniform electric fields to shape assemblies of colloidal particles was explored using quadrupolar planar microelectrodes. The AC electrokinetic (dielectrophoretic and dielectrophoretic + electroosmotic) assembly of colloidal silica and latex (primarily PMMA) in

various media was studied. Dielectrophoretic (field-induced dipole) and electroosmotic (field-double layer) forces acted to transport particles towards the electrode center, while mutual dielectrophoretic (induced dipole-induced dipole) forces led to colloids forming chains and these chains interacting with each other to form larger structures. A wide variety of shapes and sizes of assemblies were possible to generate using a single microelectrode geometry by tuning the voltage, frequency, medium/particle permittivity contrast, particle concentration and droplet volume.

For silica in water and silica in water-pluronic, very large structures were easily fabricated using moderate voltages (5 to 20V). Symmetric structures up to $150\mu\text{m}$ in cross-section were created using $1.5\mu\text{m}$ silica at moderate initial solids content (8.6wt.%/4.4vol.% solids). The shape of these structures could be tuned from being an “inverse” structure at 5V, composed of four particle-free “wells” near the minimum gap spacing between electrodes to a large curved “diamond” structure at 20V. Assemblies using a near-refractive index matching medium (DMSO) showed clear shifts in shape and size with changing voltage, as well as frequency. By introducing electroosmotic flows to the system the assemblies took on a more compacted, diamond shape compared to the more rounded, larger DEP assemblies. In both cases, the refractive index matched assemblies showed clearly the presence of particle chains and these chains aligning together to form larger structures. These chains and groups of aligned chains are clear from optical microscopy images, particularly when examining the edges of assembled structures. The overall order of structures could not be determined from optical microscopy images available. Upon medium evaporation, structures would either be completely or partially collapsed by the force of the moving meniscus and loss of dielectrophoretic trapping force.

The destruction of assemblies by medium evaporation necessitated investigation of methods of stabilizing or immobilizing assemblies *in-situ*. A number of approaches were studied, including: biotin-avidin linkages, UV crosslinking of cinnamoyl chloride functionalized silica, gelation with pluronic F-127, gelation with PVA, photopolymerization of PEGMA/PEGDMA,

photopolymerization of ETPTA and chemical crosslinking with epichlorohydrin. Gelation with pluronic F-127 was the most effective method found in this work for maintaining overall assembly shape and structure, with no significant deviation observed between optical microscopy images before and after medium gelation. Pluronic films could be removed via UV-ozone treatment or heat treatment, with the latter being more disruptive to assembly structure than the former at the (arbitrarily) chosen heating rate parameters. The use of base, sodium hydroxide specifically, to reduce the amount of pluronic adsorption on silica to attempt to achieve a more ordered structure was attempted but found to lead to strong electrothermal flows which increased in intensity as the medium evaporated and led to medium destruction. Photopolymerization with either PEGMA/PEGDMA or ETPTA is a popular technique for immobilizing colloidal crystal arrays, but this approach failed to maintain the assemblies in this work. This failure was attributed to electrothermal flows arising from temperature gradients at the polymerization front, as well as destabilization of suspensions and a loss of dielectric contrast between particle and medium. Crosslinking with epichlorohydrin is a more promising technique that eliminates the difficulties encountered with photopolymerization. Epichlorohydrin is highly soluble in both DMSO and water and is required in small quantities to be able to fix colloidal crystals in place. Additionally, epichlorohydrin directly crosslinks particles, meaning that UV-ozone, heat or some other treatment method to remove a hydrogel or polymer film is not required. The downside is the need to work with polymeric colloids (PS) or colloids with some acrylate surface functionality, PMMA-co-AA as in this work. The challenges of medium stabilization go beyond the need for SEM analysis, for photonic materials it is desirable to have air as the alternative medium in a periodic structure for larger permittivity contrast. To produce inverse colloidal crystals, polymeric colloids will have to be stabilized, impregnated with some filler material and then removed (solvent or heat treatment). These types of crystals can then be used for surface enhanced raman spectroscopy, as scaffolds for tissue engineering platforms and so on. Solving the stabilization problem for colloidal assemblies on this scale is not a trivial problem and can

be quite system specific currently, so developing a general tool set for maintaining assemblies after medium evaporation and manipulating them is of great importance.

Chapter 5: AC Electrokinetic Templating of Colloidal Particle Assemblies: Effect of Electrohydrodynamic Flows

Abstract

The use of spatially non-uniform electric fields for the contact-free colloidal particle assembly into ordered structures of various length scales is a research area of great interest. It has already been shown that even microelectrode arrays of relatively simple design are capable of driving the electrokinetic assembly of micro- and nanoparticles inside tunable electric field templates. In the present work, numerical simulations are undertaken in order to advance our understanding of the physical mechanisms that govern this colloidal assembly process and their relation to the electric field characteristics and colloidal system properties. More specifically, the electric-field driven assembly of colloidal particles in a quadrupolar planar microelectrode array with a $100\mu\text{m}$ gap was studied numerically by means of a continuum thermodynamic approach with numerical solution provided by the finite element method. Two-dimensional assembly at the surface of the microelectrodes was considered to simplify the numerical complexity of the problem. The assembly of colloidal silica ($d_p = 0.32\mu\text{m}$ and $2\mu\text{m}$) in DMSO, a near index matching fluid, at initial volume fractions of 0.1% and 1% solids was examined over a range of voltages and the equilibrium ($\vec{u}_f = 0$) and non-equilibrium ($\vec{u}_f \neq 0$) cases were compared to determine whether fluid motion had an effect on the shape and size of assemblies. It was found that the non-equilibrium case was substantially different compared to the equilibrium case, in both size and shape of the assembled structure. This dependence was related to the relative magnitudes of the electric-field driven convective motion of particles versus the fluid velocity, which was non-negligible at all studied parameters. In all but the lowest voltages and initial volume fractions of particles the fluid velocity was larger than the dielectrophoretic velocity, which has important implications

for predicting assemblies. Fluid velocity magnitudes on the order of mm/s were predicted for $0.32\mu\text{m}$ particles at 1% initial solids content, and the induced fluid velocity was found to be larger at the same voltage/initial volume fraction as the particle size decreased, owing to a larger contribution from entropic forces. Fluid rolls near the center of the microelectrode system were found which were consistent with previously experimentally observed flows. Experimental observations of an attempted equivalent to the simulations also showed that even small fluid droplets with a spreading liquid had significant z-component based effects. Despite their limitations, the 2d simulations employed herein proved capable of providing a qualitative prediction of the experimentally observed particle assembly profiles.

5.1 Introduction

The assembly of colloidal particles into ordered structures of larger characteristic dimensions (for example, on micro or larger scale) is an active topic of research for the creation of novel materials or materials with enhanced functionality, such as photonic bandgap crystals (PBG), high sensitivity sensors or microelectronics [1]. Numerous techniques exist in order to facilitate the creation of ordered colloidal structures, ranging from self-assembly, template-assisted assembly (topological/geometric assisted assembly) and external field assisted assembly (gravitational, electric or magnetic fields) [11, 12, 136]. These techniques vary in complexity and in scale of assembly, that is in the final characteristic dimension of the usable device/material. Self-assembled monolayers can be used in order to direct the placement of colloidal and other micro/nanoscale materials to specific substrate locations, such as carbon nanotubes or gold nanoparticles [12]. Template-assisted assembly can be considered as complementary to all the other listed techniques. Electric and magnetic fields offer a wider variety of control forces rather than relying primarily on gravity and can be integrated with template-assisted assembly. These types of fields are typically generated using planar microelectrodes made by microfabrication techniques (i.e. small characteristic

dimensions) to generate very high field intensities [16–18].

Specifically, the use of dielectrophoresis (force on a particle due to induced dipole in a spatially non-uniform electric field) to construct structures of varying size, order and geometry from micron and nano-sized building blocks is of significant research interest. This is due to the large degree of control parameters available for determining the final assembled structure, such as applied voltage, frequency, choice of medium and particle electrical property contrast and overall electrode geometry [16–18]. Docoslis and Alexandridis first demonstrated the use of dielectrophoresis for the assembly of three-dimensional colloidal structures, using $100\mu\text{m}$ gap quadrupolar electrodes to assemble silica and latex colloids [20]. Abe et al. examined the use of $400\mu\text{m}$ gap hyperbolic electrodes for assembly of large polystyrene (PS) colloids ($2\text{--}10\mu\text{m}$) and were able to achieve single or multiple layer structures by applying an AC and DC field simultaneously [107]. Lumsdon and Scott and Lumsdon et al. formed reversible 2d colloidal crystals of monodisperse polystyrene using applied electric fields generated by coplanar electrodes, with the assemblies diffracting light parallel, perpendicular or both to the assembly depending on the assembly time [19, 74]. Reversible 2d colloidal crystals fabricated by electric fields have also been shown by numerous authors [93, 108–110]. Similarly, binary PS colloidal crystals and aggregates have been formed using application of DC and AC sources respectively across a simple coplanar electrode structures [137, 138]. Large-scale colloidal crystals $200\mu\text{m}$ in size have been formed without significant grain-boundaries by successive application and relaxation of an applied electric field in a hexapolar electrode system [111]. More recently, three-dimensional structures of varying complexity have been demonstrated using dielectrophoresis and induced-charge electroosmotic flows [112]. For a comprehensive overview of the use of dielectrophoresis for colloidal assembly, and for colloidal assembly in general, the articles of Velev and Bhatt and Velev and Gupta are recommended [71, 113].

In terms of simulations, most of the work to date in describing the assembly/patterning of colloids with dielectrophoresis has focused on the force on an isolated particle to determine

trajectories, assuming no interparticle electric field interactions and generally relying on the point-dipole or series expansion of multipoles to account for particle perturbation of the local electric field [16, 98, 139, 140]. Some more involved numerical methods, such as using distributed Lagrange multipliers (DLM) have also been used, but also often rely on simplified electrical interaction equations and have been limited to date to solving the case with a small number of particles [31, 104, 139]. More recently, Juarez et al. showed that inverse Monte Carlo (MC) based simulations could be used to reconstruct colloidal density profiles in non-uniform electric fields, specifically 2d assembly in finger electrodes and 3d assembly in quadrupolar electrodes [141, 142]. This approach is not predictive, the experimental radial distribution functions of an assembled colloidal structure were measured via confocal microscopy and used for updating a series of MC steps to obtain a fitted frequency correction factor. However, this approach was able to reconstruct, very accurately, assemblies of large colloidal particles ($1.5\mu\text{m}$ for the 3d case) under the action of applied non-uniform electric fields, as well as crystallinity. The question of how well this approach will be able to capture other phenomena of interest, such as distortions to the electric field by particles, change in the dipole-coefficient due to multiparticle effects, etc. is yet to be explored, although overall it does represent a very interesting framework. The effect of persistent fluid flows was not considered in this work, as the authors were interested in an equilibrium solution. For smaller particles, which will experience higher relative diffusional fluxes as well as smaller electric field induced convective motion, the contribution of fluid flows may not be negligible. The effect of fluid flow in non-uniform electric field driven colloidal assembly has generally not been particularly discussed in literature to date and is generally assumed to be negligible compared to field-dipole and dipole-dipole interactions on particles, or assumed dominated by an externally driven-flow field [143]. Given the difference in characteristic time-scales for diffusion and convective (electric field, gravity, etc.) driven motion, the influence of fluid flow on the resulting structure may not be negligible, that is potentially different structures may be arrived at by, for example, allowing particles to settle and then applying an electric field.

In the equilibrium case, no difference (other than any potential numerical approximations) would be expected for allowing particles to settle compared to applying the field directly, as the chemical potential gradient of the system is zero for the equilibrium case.

In this paper, the simulation of electric-field induced colloidal pattern formation by quadrupolar electrodes was considered, specifically for the case of silica particles ($d_P = 0.32\mu\text{m}$ and $2\mu\text{m}$) in DMSO, a near index-matching fluid. As a theoretical basis, the continuum thermodynamic approach for describing the free energy of a colloidal suspension subjected to an electric field developed by Khusid and Acrivos was chosen [144, 145]. With this approach, the free energy, as well as electric field and physical transport properties of the suspension, are treated as functions of volume fraction. This framework accounts for interparticle interactions, is more numerically tractable in the sense of solving a single PDE for volume fraction instead of multiple ODEs for individual particles and has been successfully applied to predict the formation of electric field driven volume fraction fronts [143, 146]. The primary aim of this work was to examine the influence of fluid flow resulting from particle motion on electric-field induced assembly of monodisperse colloids into structures of various shapes/sizes, specifically to look at the “equilibrium” or quiescent fluid flow case ($\vec{u}_f = 0$) versus the “non-equilibrium” or non-quiescent fluid flow case ($\vec{u}_f \neq 0$). As mentioned, the effect of any potential fluid flows in this type of system have been generally either neglected or not considered in previous simulation work to date and therefore quantifying any impact on electric-field induced assemblies is quite important. Including the influence of fluid flow is particularly straightforward in this framework, as the fluid is treated as an incompressible liquid with volume fraction dependent viscosity and density that experiences a volumetric force directly proportional to the gradient of chemical potential. Simulations of the influence of particle size, voltage and initial volume fraction on the predictions of the shape and size of the resulting colloidal assembly were performed with comparison between the equilibrium and non-equilibrium case. Some validation by comparison to experimental data in the form of optical microscopy images was also attempted.

5.2 Theoretical Background

The framework developed by Khusid and Acrivos has been used by these same authors in later work to describe electric field induced formation of volume fraction fronts quite successfully as a predictive model with no fitting parameters [143, 146]. To describe the motion of particles, the chemical potential of the suspension is developed by adopting a hard-sphere approach, where entropic contributions to chemical potential are given by classical hard sphere results and the electrical contributions are derived from a cell model (which corresponds to Maxwell-Wagner type polarization)[144]. The attractive part of the potential is assumed to be dominated by electric-field induced interactions. In this work a similar approach is used, with some modification to account for additional volume fraction-dependent effects (diffusion coefficient), for describing the assembly process of monodisperse silica colloids with a non-uniform electric field generated by quadrupolar microelectrodes with a gap spacing of $100\text{ }\mu\text{m}$. We also considered that the fluid flows resulting from particle motion are not necessarily negligible at the conditions studied for this framework, with the idea of testing this assumption through comparison of the equilibrium and non-equilibrium cases. The time-averaged chemical potential (μ_p) and osmotic pressure (Π_p) of a colloidal suspension under the influence of an external electric field at high frequencies are given by eqns. 5.1 and 5.3 respectively [146]

$$\mu_p = \frac{k_B T}{v_p} \frac{df_0}{dc} - \frac{\varepsilon_0}{2} \left(\frac{d\varepsilon_s}{dc} \right) \langle |\vec{E}|^2 \rangle \quad (5.1)$$

$$f_0 = c \ln \frac{c}{e} + c \int_0^c \frac{Z(c) - 1}{c} dc \quad (5.2)$$

$$\Pi_p = \frac{k_B T}{v_p} c Z + \frac{\varepsilon_0}{2} \left[\varepsilon_s - c \left(\frac{d\varepsilon_s}{dc} \right) \right] \langle |\vec{E}|^2 \rangle \quad (5.3)$$

where $k_B T$ is thermal energy, c is particle volume fraction, Z is the suspension compressibility factor, ε_s is the real part of suspension permittivity and $\left(\frac{d\varepsilon_s}{dc}\right)$ is the derivative of the real part of suspension permittivity with respect to particle volume fraction. f_0 represents the entropic contributions to the free energy of the system and is determined via an equation of state. The imaginary component of complex permittivity is negligibly small compared with the real part at the frequencies of interest in this work (MHz range), and this high frequency will minimize the influence of conductivity on the polarizability of the particle. The suspension compressibility factor can be calculated using the Carnahan-Starling equation, with the diverging volume fraction chosen as that of a random close-packed suspension, eqn. 5.4, and the suspension permittivity from the Maxwell-Wagner expression, eqn. 5.5 [146]:

$$Z = \begin{cases} \frac{1 + c + c^2 - c^3}{(1 - c)^3} & 0 < c \leq 0.5 \\ \frac{1.85}{0.64 - c} & 0.5 < c \leq 0.64 \end{cases} \quad (5.4)$$

$$\varepsilon_s = \varepsilon_m \left[\frac{1 + 2c\beta}{1 - c\beta} \right] \quad \beta = \frac{\varepsilon_p - \varepsilon_m}{\varepsilon_p + 2\varepsilon_m} \quad (5.5)$$

where in eqn. 5.5, ε_i is the permittivity of the suspension, medium or particle (subscript s , m or p respectively) and β is the real part of the Clausius-Mossotti factor. More complicated models accounting for volume fraction-dependent effects on polarization could be used, such as the model proposed by Sihvola and Kong (1988), but Maxwell-Wagner type polarization was assumed for simplicity, as the interest in this work was in testing the influence of fluid flows resulting from the chemical potential gradients arising in the system [147].

Along the coexistence curve for the single phase region of the suspension versus a two-phase region induced by the electric field effects, the value of chemical potential and osmotic pressure of each phase are equal. The volume fraction of particles in each phase is denoted

by c_1 and c_2 , where 1 refers to the low solids volume fraction phase and 2 to the high solids volume fraction phase respectively, as shown in eqn. 5.6 [144]:

$$\mu_p(c_1) = \mu_p(c_2) \quad \text{and} \quad \Pi_p(c_1) = \Pi_p(c_2) \quad (5.6)$$

For electric-field induced aggregation the value of the spinodal composition, that is the metastable limit of the system, can also be useful for illustrating pattern formation. The spinodal composition is found from solutions to eqn. 5.7:

$$Z + c \left(\frac{dZ}{dc} \right) - c \left(\frac{v_p}{k_B T} \frac{\varepsilon_0}{2} \right) \left(\frac{d^2 \varepsilon_s}{dc^2} \right) \langle |\vec{E}|^2 \rangle = 0 \quad (5.7)$$

The solution of eqns. 5.6 and 5.7 allow for the phase diagram (coexistence and spinodal curves) of volume fraction versus applied field strength to be determined for a given particle-medium combination and the critical point common to both indicates the minimum value of electric field strength required to drive particle aggregation.

The electric field profile of the suspension can be determined using Gauss' law, with the permittivity described by eqn. 5.5:

$$\nabla \cdot [\varepsilon_s(c) \nabla \phi] = 0 \quad \text{and} \quad \vec{E} = -\nabla \phi \quad (5.8)$$

The particle volume fraction profile evolves according to eqn. 5.9

$$\frac{\partial c}{\partial t} + \nabla \cdot [c \vec{u}_f + \vec{j}_p] = 0 \quad \text{and} \quad \vec{j}_p = \frac{c(1-c)^2}{6\pi r_p \eta_s(c)} [-\nabla \mu_p] \quad (5.9)$$

where \vec{u}_f is the fluid velocity and \vec{j}_p represents particle flux.

Eqn. 5.9 can be re-written in terms of the electrical and entropic (diffusional) contributions, specifically as:

$$\frac{\partial c}{\partial t} + \nabla \cdot [-D \nabla c + (\vec{u}_f + \vec{u}_{elec})c] = 0 \quad (5.10)$$

where the diffusivity, D , and electric-field induced velocity, \vec{u}_{elec} , are given by eqns. 5.11 and 5.12,

$$D = \frac{k_B T (1-c)^2}{6\pi r_p \eta_s(c)} \frac{d(cZ)}{dc} \quad (5.11)$$

$$\vec{u}_{elec} = \frac{(1-c)^2 v_p \varepsilon_0}{6\pi r_p \eta_s(c)} \frac{1}{2} \nabla \left[\left(\frac{d\varepsilon_s}{dc} \right) \langle |\vec{E}|^2 \rangle \right] \quad (5.12)$$

The factor $(1-c)^2$ is referred to as the hindrance function and combined with the particle volume fraction dependent viscosity, is taken to account for all hydrodynamic interactions of particles in the suspension. The suspension viscosity is treated using the Leighton-Acrivos equation.[146]:

$$\eta_s(c) = \eta_m (1 - c/c_{max})^{-2.5c_{max}} \quad (5.13)$$

Finally, a momentum balance on the fluid yields:

$$\rho_s \left(\frac{\partial \vec{u}_f}{\partial t} + \vec{u}_f \cdot \nabla \vec{u}_f \right) = -\nabla p + \nabla \cdot [\nabla \vec{u}_f + \nabla \vec{u}_f^T] - c \nabla \mu_p \quad \text{and} \quad \nabla \cdot \vec{u}_f = 0 \quad (5.14)$$

The Navier-Stokes form of the momentum balance was chosen initially as although the expected Reynolds number is quite low, inertial effects were not necessarily negligible due to the large gradients that can potentially arise in this system. Subsequent simulations showed in fact that the inertial term was negligible and Stokes' flow can be assumed. Solution of eqns. 5.8, 5.9 and 5.14 allows for the time-evolution profile of particle volume fraction within the system to be determined. Examination of the force term in eqn. 5.14 shows that in the limit of dilute suspensions ($c \rightarrow 0$) the fluid velocity becomes zero and the steady-state solution will be equal to the equilibrium solution.

5.3 Materials and Methods

5.3.1 Simulation Details

Numerical solution of the volume fraction, velocity and electric field profiles was achieved through solving the time-dependent PDEs described previously using FEM techniques in Comsol Multiphysics (Burlington, MA, USA). A 2d representation of the electrode geometry was drawn, with the system solved using a one-eighth symmetry in terms of the mirror image about the 45° line extending from the origin, as is illustrated in Figure 5.1. Quadrilateral elements were used for improving resolution of the nonlinearities present in the system of PDEs, which arise due to volume fraction-dependence of physical properties of the suspension. as well as to improve time-stepping stability [148]. The electric field solution was obtained through solving for potential, with the potential treated using quadratic Lagrange elements. For the fluid velocity, the Navier-Stokes equations were solved using quadratic Lagrange elements for the velocity components and linear elements for pressure, while the volume fraction utilized linear Lagrange elements to handle the sharp gradients/discontinuities in volume fraction and for better stability in terms of time-stepping. Numerical stabilization of the particle volume fraction profile was achieved through the use of artificial diffusion, in the form of an $O(h^2)$ isotropic stabilization. Artificial diffusion was required for solution of this convection-dominated PDE, particularly in the case of larger particle sizes/higher applied voltages, to avoid spurious oscillations and non-physical results [149]. Mesh-independence tests were performed to insure decoupling of the solution with mesh quality and additionally mass conservation in the suspension versus time was also considered and found to be negligible (less than 1e-10 percent relative deviation from initial to final integration time for conditions studied).

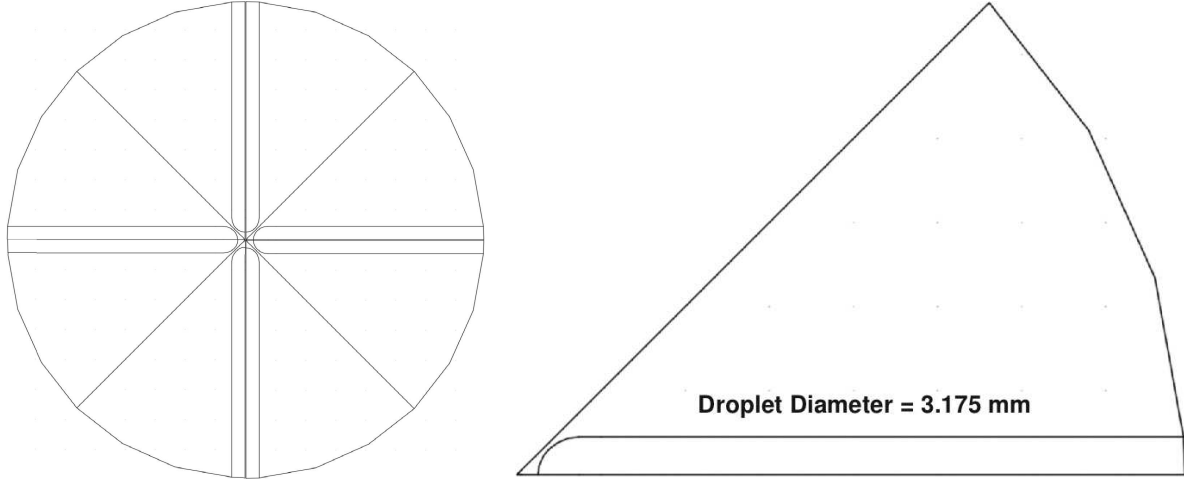


Figure 5.1: Simulation Geometry
 Left: Top-Down System View Divided into Eighths, Right: Expanded One-Eighth View

5.3.2 Experimental Details

Aqueous suspensions of silica particles ($d_p = 0.32\mu\text{m}$, $1\mu\text{m}$ and $2\mu\text{m}$) were purchased from Bangs Laboratories (Fishers, IN). These suspensions were directly diluted to desired volume fractions using DMSO (Sigma Aldrich, Canada) and contained small amounts of water ($<2\text{ vol}\%$ maximum). DMSO is a near-index matching solvent for silica, which will allow for minimizing the van der Waals interactions, and also will result in negligible acid-base (polar) interactions between particles as determined by calculations using XDLVO theory [119, 150]. DMSO also is a spreading liquid, meaning it is a very good candidate as a suspending fluid for silica particles due to the thin liquid, flat liquid films which will spread on the electrode surface which will minimize settling effects and any surface tension driven flows. Use of DMSO, a high boiling point solvent, allowed for a very thin, non-evaporating film of liquid to be placed on a chip ($500\mu\text{m}$ thick silicon with a $0.5\mu\text{m}$ layer of SiO_2 separating the substrate from the microelectrodes). The suspension is not perfectly index matched in order to allow for sufficient contrast for observation by optical microscopy. As DMSO is a spreading liquid on silica surfaces, a $1/8''$ (3.175 mm) diameter circular well was constructed using a

double-sided press to seal adhesive with parafilm on top. This circular edge acted to constrain any droplet on the chip. $0.5\mu\text{L}$ aliquots of suspension were pipetted for each experimental run. Non-uniform AC electric fields were generated by using gold microelectrodes (200nm thick) fabricated by photolithography on a SiO_2 surface ($0.5\mu\text{m}$ thick) deposited on top of a silicon wafer as previously mentioned. The frequency of all experiments was chosen as 1MHz, to eliminate the conductivity effects on particle polarization. The tip-to-tip distance between opposite electrodes (ℓ_c) was $100\mu\text{m}$. Power to the microelectrodes was supplied by a signal generator (BK Precision 4040A). Microelectrodes were connected to the source in an alternating fashion (180° phase difference between adjacent electrodes). The value of the applied voltage (V , peak-to-peak) and applied frequency (f), were monitored by an oscilloscope (Tektronix 1002B). A top-down optical microscopy image of the electrodes is provided in Figure 5.2. Optical microscopy was performed using an Olympus BHM microscope, with a digital camera for image capture, to observe the suspension behavior upon application of an electric field.

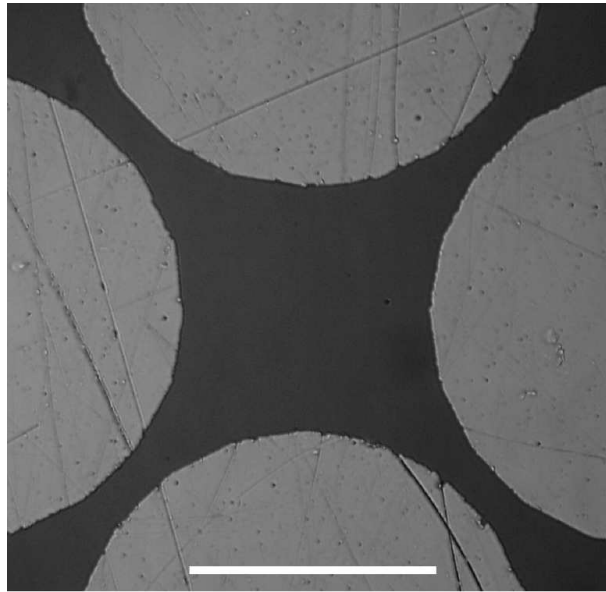


Figure 5.2: Top-Down View of $100\mu\text{m}$ gap spacing hyperbolic microelectrode chip
[Scalebar is $100\mu\text{m}$]

5.4 Results and discussion

To determine the effectiveness of using the Khusid-Acrivos framework for predicting shape and size of electric field induced structures, a number of simulation conditions were chosen and compared with experimental counterparts. The behavior of silica particles of $0.32\mu\text{m}$ and $2\mu\text{m}$ diameter at an initial (uniform) suspension of 0.1 and 1% particles by volume respectively were simulated at various voltages, ranging from 5 to 20V (peak to peak) for $0.32\mu\text{m}$ and 0.5 to 5V for $2\mu\text{m}$, by solving for volume fraction, velocity and electric field profiles simultaneously versus time for 2 hours ($0.32\mu\text{m}$) and 10 minutes ($2\mu\text{m}$). $2\mu\text{m}$ and $0.32\mu\text{m}$ were chosen as particle sizes in order to examine the influences of entropic and electrical contributions on the final assembly profile (volume fraction of particles), as well as on the dielectrophoretic and fluid velocity profiles in the system. Higher voltages for $2\mu\text{m}$ simulations were not considered due to experimental results showing that multilayer structures clearly arose well before 20V. Based on order of magnitude estimates for transit and aggregation time of particles under the influence of electric fields and at the field strengths chosen, 2 hours for $0.32\mu\text{m}$ and 10 minutes for $2\mu\text{m}$ represents a more than sufficient time for the system to be at \sim steady-state [144]. This was confirmed by observing that the final shape of the simulated volume fraction profile ceased to change well before the final simulation time was reached, as well as through optical microscopy observations of experimental equivalents where possible. Both the quiescent (equilibrium) and non-quiescent (non-equilibrium) cases were solved at each voltage, initial volume fraction and particle size in order to determine what impact the fluid flows resulting from electrical and diffusional driven particle fluxes have on the steady-state particle volume fraction (c) profile.

Visualization of the resulting volume fraction profiles was focused on a $100\mu\text{m} \times 100\mu\text{m}$ box at the center between electrodes, shown in Figure 5.3 as region A, while fluid and dielectrophoretic velocity profiles are visualized on a one-quarter cutout of the entire plane in Figure 5.3 bounded by the dotted-line. A representative electric field profile at $t=0$, i.e.

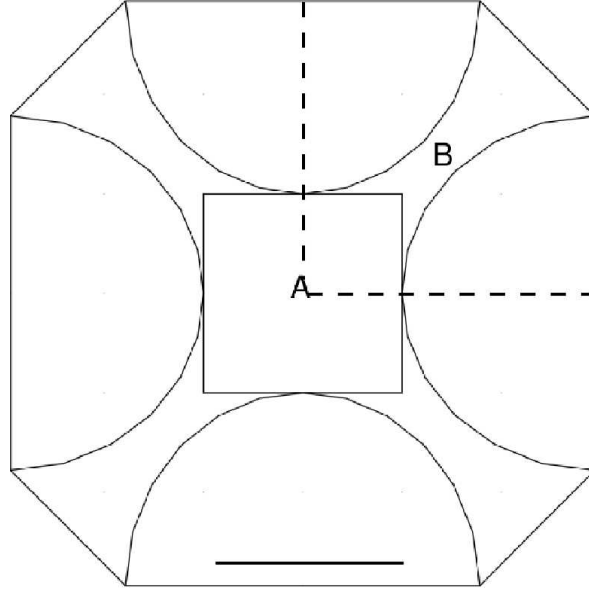


Figure 5.3: Visualization Planes for Simulation
[scalebar is $100\mu\text{m}$]

uniform volume fraction, with 20V applied peak to peak is shown in Figure 5.4. At uniform volume fraction, the suspension permittivity is constant throughout the system and eq. 5.8 becomes the linear Laplace equation. The electric field maximum occurs at the smallest gap spacing between adjacent electrodes, which is approximately at the location labeled B in Fig. 5.3. The maximum electric field intensity in the system is approximately constant versus time at the volume fractions studied, as particles are pushed away from region B meaning the suspension permittivity is essentially constant in the gap between electrodes. For $0.32\mu\text{m}$ particles, the simulated volume fraction profiles after 7200s are shown in Fig. 5.5 ($c_0 = 0.1$ vol. %) and Fig. 5.6 ($c_0 = 1$ vol. %) for both the equilibrium and non-equilibrium cases at 5, 10, 15 and 20V. As can be seen from comparing the equilibrium to non-equilibrium cases, at both initial volume fractions there is an impact on the final volume fraction profile obtained. For $c_0 = 0.1$ vol. %, as voltage increases the shape of the evolved structures for both equilibrium and non-equilibrium becomes similar, with the non-equilibrium case assemblies being slightly larger (for example, at the 20V case, $\sim 24\mu\text{m}$ vs. $\sim 20\mu\text{m}$). Additionally, the

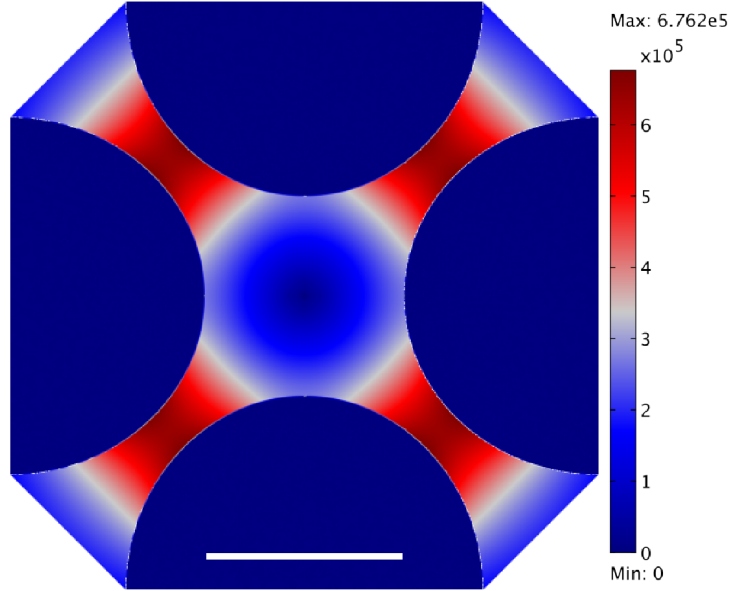


Figure 5.4: Electric Field Strength at $V_{\text{applied}} = 20V$ peak-to-peak at $t=0$
[scalebar is $100\mu\text{m}$]

equilibrium case simulations achieve a more “diamond” shape at earlier voltages, while the non-equilibrium case remains more rounded until 15V, Fig. 5.5f). The maximum volume fraction in the system is also higher in the equilibrium case vs. the non-equilibrium until the system reaches 20V. For the $c_0 = 1$ vol. % case there is a more dramatic impact on the assembly profile, as can be seen from comparing equilibrium to non-equilibrium cases in Fig. 5.6. Comparing the equilibrium and non-equilibrium case at $c_0 = 1$ vol. %, the former yields a much larger predicted assembly which tends from circular shape at lower voltages to a more rounded diamond at higher voltages, while the latter is far smaller in size and maximum volume fraction as well as progressing from more inwardly-rounded diamond/hyperbola-like shapes to a diamond as voltage is increased. At the higher initial volume fraction in the system, there is somewhat counter-intuitively a smaller steady-state assembly and lower maximum volume fraction versus the $c_0 = 0.1$ vol. % case when the influence of fluid flow is considered. However, examination of the electrical and fluid velocities for $0.32\mu\text{m}$ particles at the given volume fractions and voltages helps to explain this effect.

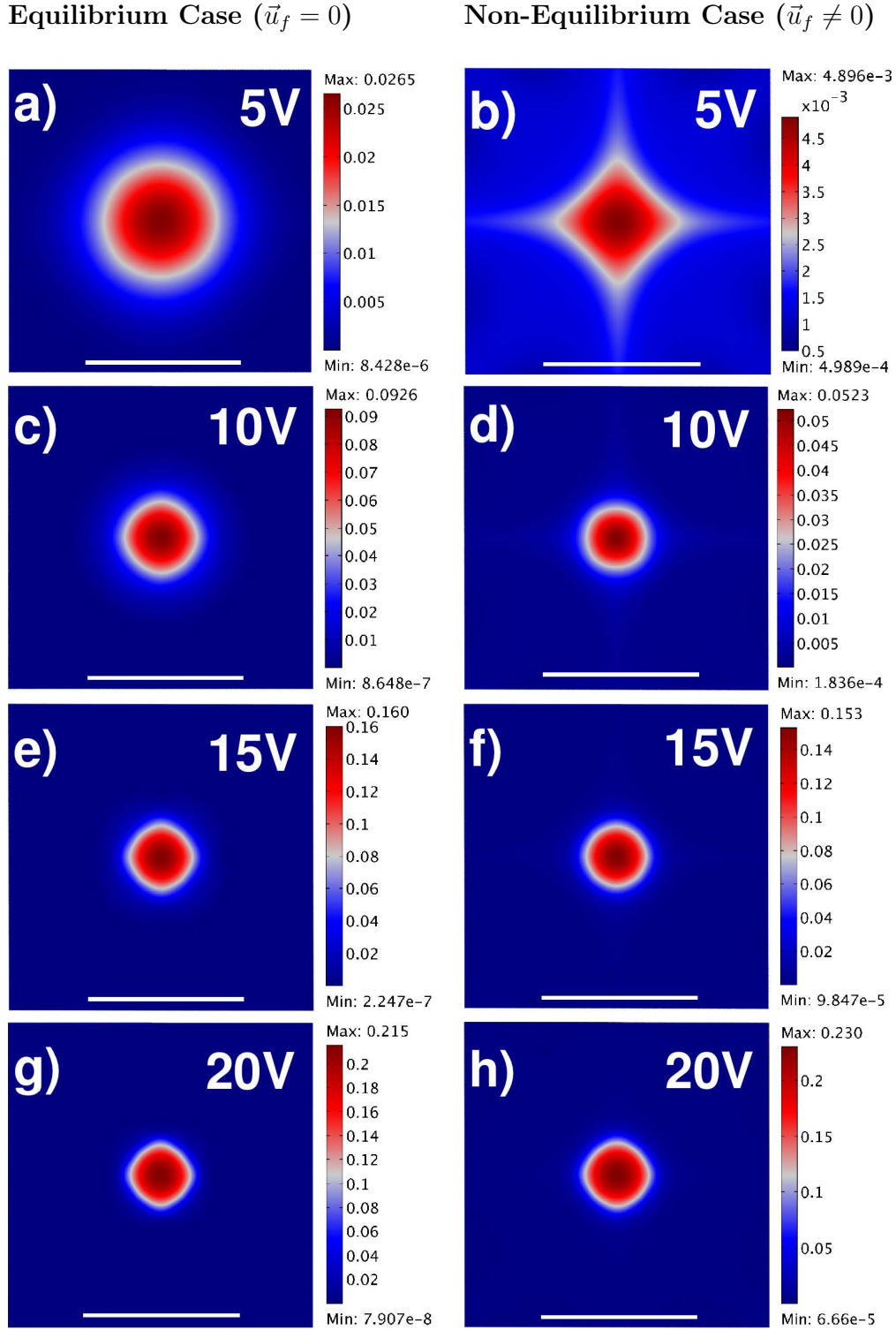


Figure 5.5: Particle Volume Fractions with and without fluid flow for $d_p = 0.32\mu\text{m}$ in DMSO, $c_0 = 0.1$ vol. %

a) 5V equilibrium case, b) 5V with fluid flow, c) 10V equilibrium case, d) 10V with fluid flow, e) 15V equilibrium case, f) 15V with fluid flow, g) 20V equilibrium case, h) 20V with fluid flow, note differences in volume fraction scale between equilibrium and non-equilibrium cases [scalebar is $50\mu\text{m}$]

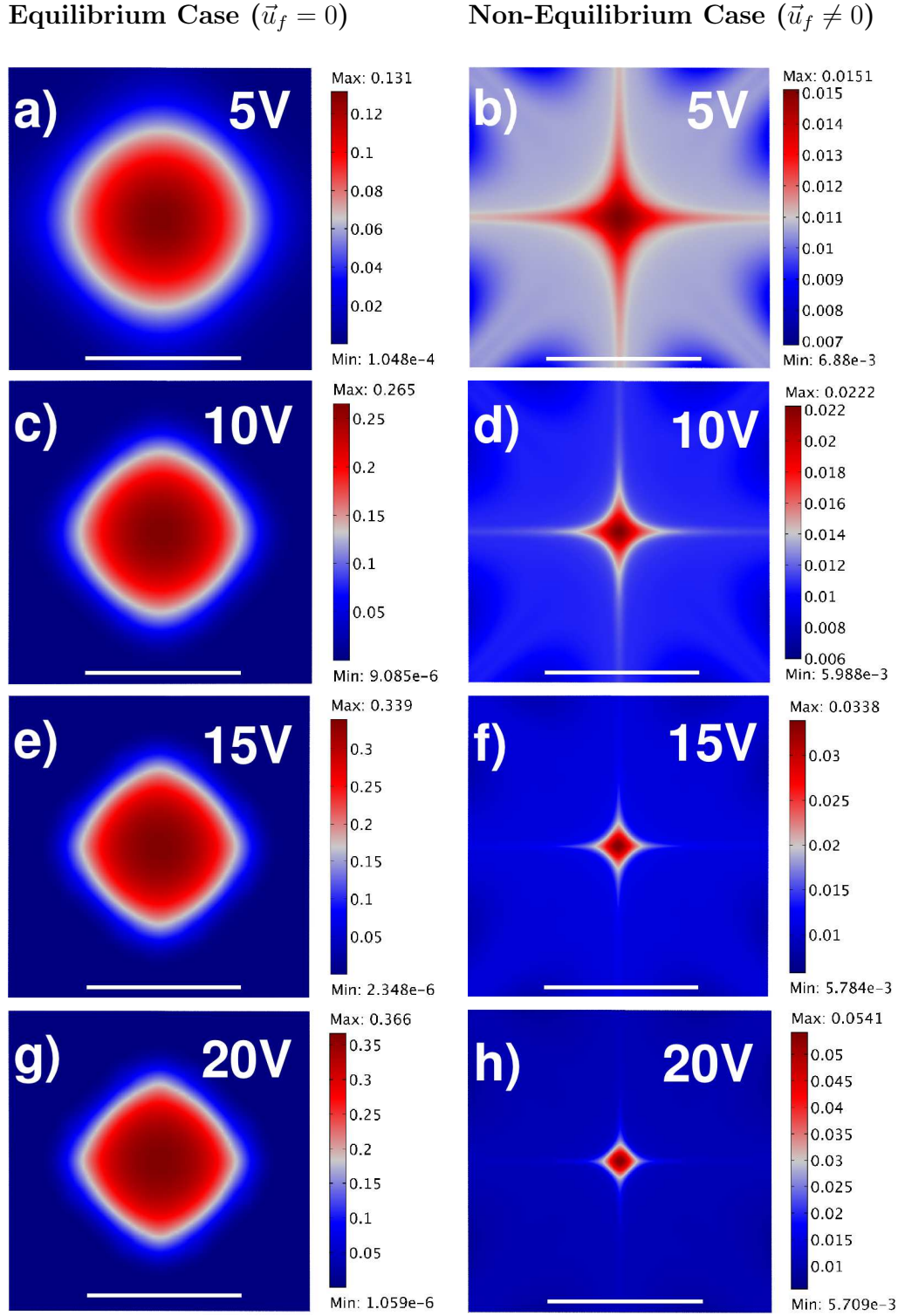


Figure 5.6: Particle Volume Fractions with and without fluid flow of $d_P = 0.32 \mu\text{m}$ silica in DMSO, $c_0 = 1$ vol. %

a) 5V equilibrium case, b) 5V with fluid flow, c) 10V equilibrium case, d) 10V with fluid flow, e) 15V equilibrium case, f) 15V with fluid flow, g) 20V equilibrium case, h) 20V with fluid flow, note differences in volume fraction scale between equilibrium and non-equilibrium cases [scalebar is $50 \mu\text{m}$]

Figure 5.7 depicts the dielectrophoretic and fluid velocity profiles for $0.32\mu\text{m}$ silica for both $c_0 = 0.1$ vol. % and 1 vol. % at 5V in a one-quarter cutout of the visualization plane, Fig. 5.3. Even at lower voltages, the fluid velocity is substantially larger compared to the dielectrophoretic velocity at both initial volume fractions and this trend continues throughout all voltages studied. The fluid velocity is several orders of magnitude larger than the dielectrophoretic velocity. As well, from examining both figures, a re-circulation zone or roll can be seen in the bottom-left corner of the figures, that is near the center of the system, significant fluid rolls are predicted. These fluid rolls are responsible for the shift in shape and size of the structures between the equilibrium and non-equilibrium cases, with this effect more pronounced at higher initial solids volume fraction as the fluid velocity increases while the dielectrophoretic velocity is slightly decreased. Increasing the initial solids volume fraction also leaves the dielectrophoretic and fluid velocity spatial profiles nearly unchanged, that is the maxima/minima occur at nearly the same locations. For $c_0 = 1$ vol.% and 5V, the fluid velocity maximum is approximately two orders of magnitude greater than the dielectrophoretic maximum, whereas it is closer to one order of magnitude at $c_0 = 0.1$ vol.%, and a similar result is obtained at higher voltages. This dominance of fluid flow and the resulting change in the assembly profile illustrates the importance of accounting for fluid flow effects for smaller particles, for which electric-field driven convection effects on particles are weaker. For $0.32\mu\text{m}$ particles at the voltages studied, the maximum fluid velocity in all simulation cases was found to be on the order of mm/s (20V, $c_0 = 1$ vol.%), but even the smallest value was on the order of $\sim 10\mu\text{m/s}$, which is significantly higher than $\sim 0.1\mu\text{m/s}$ to $1\mu\text{m/s}$ range for the dielectrophoretic velocity.

The $2\mu\text{m}$ silica case is shown in Figures 5.8 ($c_0 = 0.1$ vol. %) and 5.9 ($c_0 = 1$ vol. %) after an assembly time of 600s, for both the equilibrium and non-equilibrium cases at 0.5, 2.5 and 5V. For the 0.1 vol.% c_0 case, simulations show that fluid flow has an influence on both shape and size of assembled volume fraction profiles and that as for $0.32\mu\text{m}$ particles, this effect is more pronounced at larger initial volume fractions. Unlike $0.32\mu\text{m}$ particles,

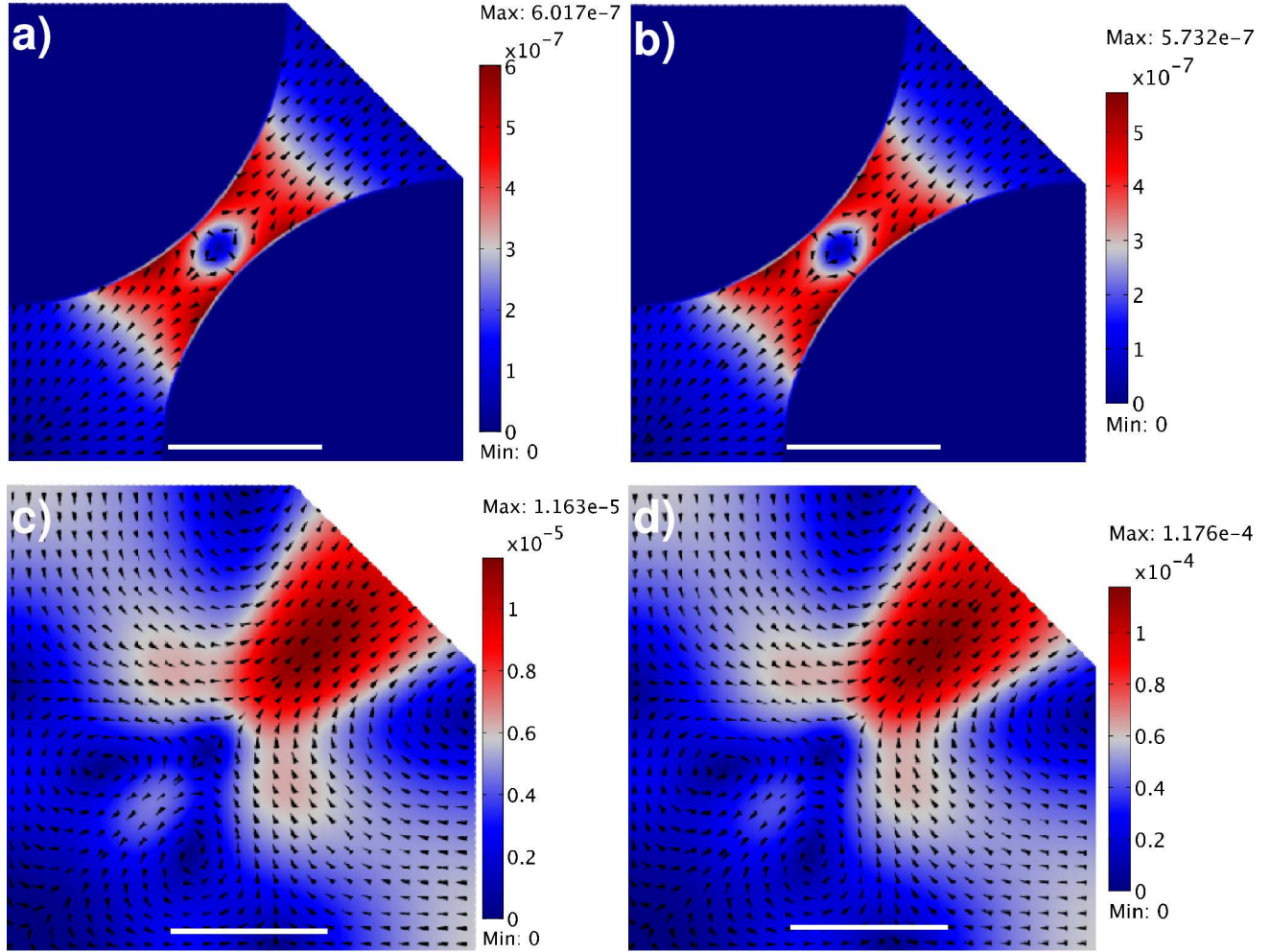


Figure 5.7: Dielectrophoretic and Fluid Velocities (m/s) for $0.32 \mu\text{m}$ silica in DMSO at 5V
a) DEP velocity, $c_0 = 0.1$ vol.%, b) DEP velocity, $c_0 = 1$ vol. %, c) Fluid velocity, $c_0 = 1$ vol. %, d) Fluid velocity, $c_0 = 1$ vol.% [scalebar is $50 \mu\text{m}$]

the non-equilibrium case for $2 \mu\text{m}$ particles also has higher volume fractions within the assembly as well as a larger assembled size versus the equilibrium case and the increase in size is also more drastic ($\sim 18 \mu\text{m}$ vs. $\sim 10 \mu\text{m}$ diameter at 5V). Increasing solids volume fraction for $2 \mu\text{m}$ particles also increases the size of the assembly and maximum volume fraction for both the equilibrium and non-equilibrium cases, which is unlike the results for $0.32 \mu\text{m}$

particles where increasing solids volume fraction led to a decrease in both size and maximum volume fraction. These results are attributed again to the interplay between fluid and dielectrophoretic convection, and to the smaller influence of diffusion for $2\mu\text{m}$ compared to $0.32\mu\text{m}$ particles. 5.10 show the dielectrophoretic and fluid velocity profiles of $2\mu\text{m}$ silica for 5V. At 0.5V, the dielectrophoretic velocity of the $c_0 = 0.1$ vol.% case is larger than that of the fluid velocity, and this holds true as the voltage is increased up to 5V. For the 1 vol.% c_0 case, the fluid velocity is larger at any voltage versus the dielectrophoretic velocity but this difference is closer to a factor of 4X, which is much less than the contrast that was observed for $0.32\mu\text{m}$ particles (closer to 100X). This reduction is due to the fluid velocity at the same voltage/initial volume fraction being lower for $2\mu\text{m}$ particles compared to $0.32\mu\text{m}$, as illustrated by comparing the 5V cases for both particles sizes, Fig. 5.7d) with 5.10d). For $2\mu\text{m}$ particles at 5V, the dielectrophoretic velocity is larger vs. fluid velocity at 0.1% while the fluid velocity becomes larger at 1 vol.% initial solids loading. $0.32\mu\text{m}$ particle simulations are attributed to have a larger fluid velocity at similar conditions compared to $2\mu\text{m}$ due to increased entropic contributions to the chemical potential (increases as particle size decreases) dominating over decreased electrical contributions. The fluid velocity for $2\mu\text{m}$ particles was on the order of $0.01\mu\text{m/s}$ to $100\mu\text{m/s}$ and the dielectrophoretic velocity $\sim 0.1\mu\text{m/s}$ to $\sim 10\mu\text{m/s}$, although over a smaller voltage range versus the studied $0.32\mu\text{m}$ conditions.

The maximum values of electrically-driven (DEP) and fluid velocity magnitudes vs. voltage at 0.1 and 1% by vol. for both $0.32\mu\text{m}$ and $2\mu\text{m}$ particles are shown in Figures 5.11 ($0.32\mu\text{m}$) and 5.12 respectively. Both fluid velocity and DEP (electrically driven) velocity follow near quadratic dependence on voltage with respect to maximum intensity, with the magnitude of DEP velocity slightly affected by volume fraction (more so for the $2\mu\text{m}$ case vs. the $0.32\mu\text{m}$) and the changes in fluid velocity magnitude nearly linearly proportional to changes in initial volume fraction. This quadratic dependence on voltage for both fluid and DEP velocities is expected based on the nature of the chemical potential and matches the

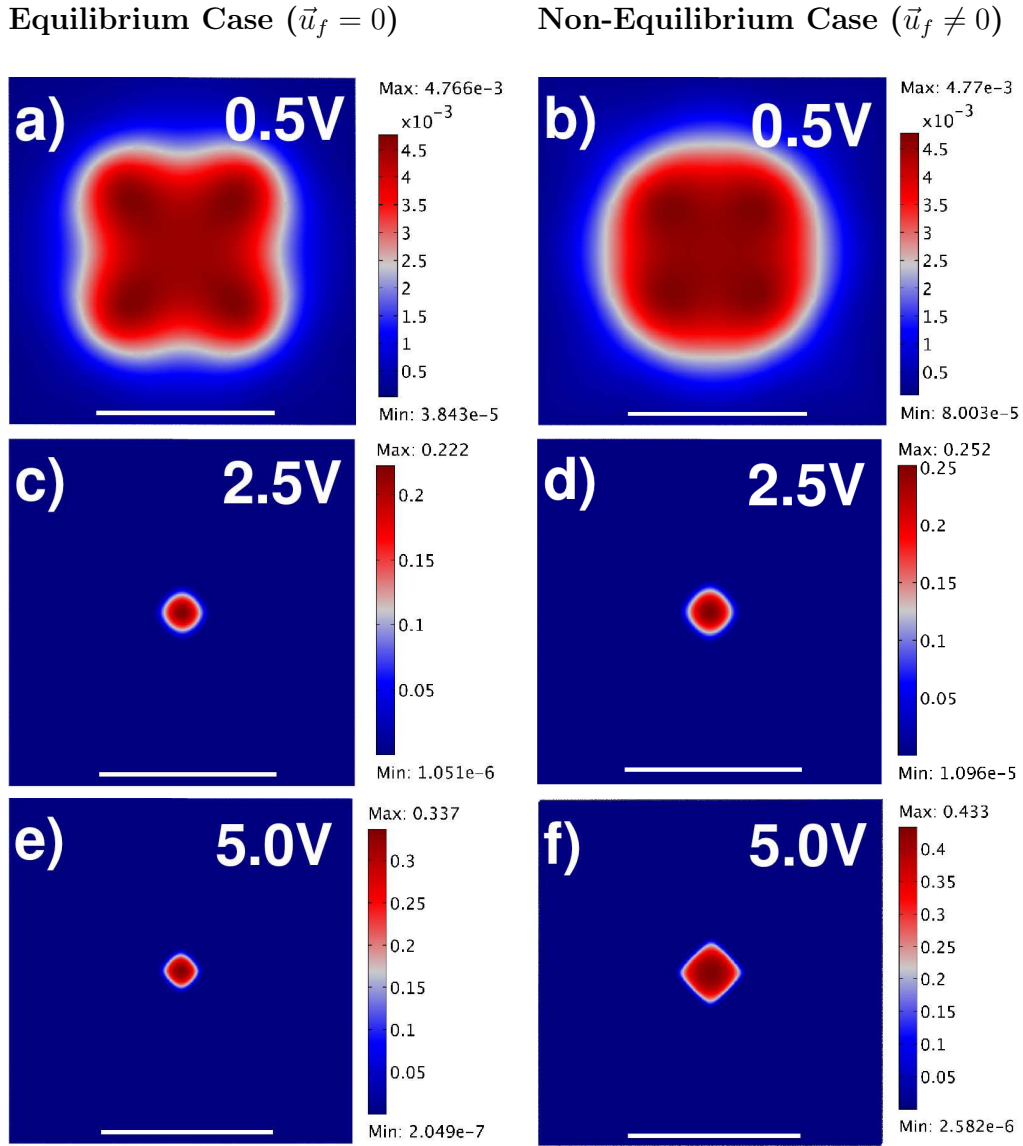


Figure 5.8: Particle Volume Fractions with and without fluid flow of $d_P = 2\mu\text{m}$ silica in DMSO, $c_0 = 0.1$ vol.%

a) 0.5V equilibrium case, b) 0.5V with fluid flow, c) 2.5V equilibrium case, d) 2.5 V with fluid flow, e) 5V equilibrium case, f) 5V with fluid flow, note differences in volume fraction scale between equilibrium and non-equilibrium cases [scalebar is $50\mu\text{m}$]

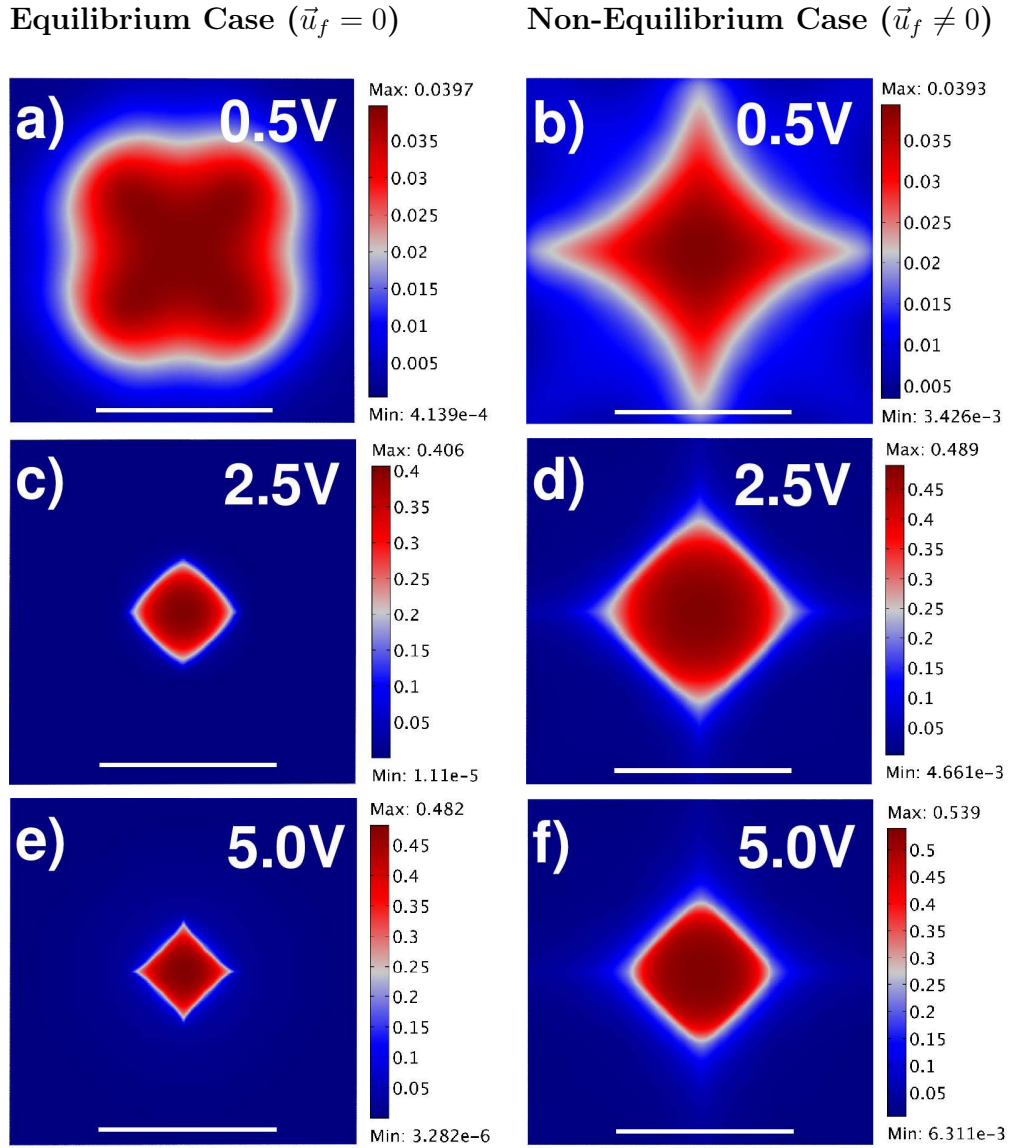


Figure 5.9: Particle Volume Fractions with and without fluid flow of $d_P = 2\mu\text{m}$ silica in DMSO, $c_0 = 1 \text{ vol.}\%$

a) 0.5V equilibrium case, b) 0.5V with fluid flow, c) 2.5V equilibrium case, d) 2.5 V with fluid flow, e) 5V equilibrium case, f) 5V with fluid flow, note differences in volume fraction scale between equilibrium and non-equilibrium cases [scalebar is $50 \mu\text{m}$]

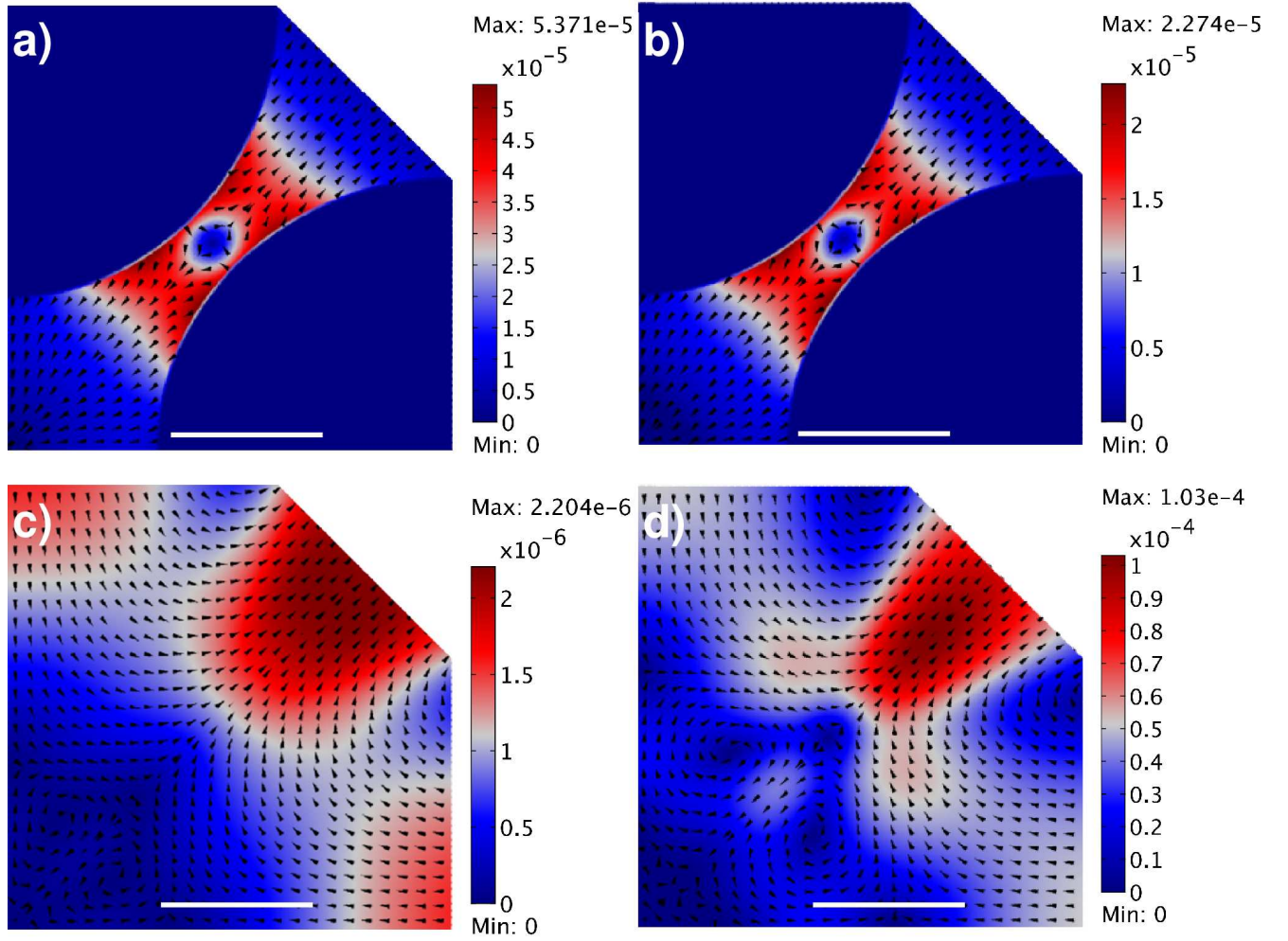


Figure 5.10: Dielectrophoretic and Fluid Velocities (m/s) for 2 μm silica in DMSO at 5V
a) DEP velocity, $c_0 = 0.1\%$, b) DEP velocity, $c_0 = 1\%$, c) Fluid velocity, $c_0 = 1\%$, d) Fluid velocity, $c_0 = 1\%$ [scalebar is 50 μm]

dilute-case/point-dipole result for the dielectrophoretic force, which depends on the gradient of the electric field intensity squared. Unlike electrothermal flows induced by Joule heating, where the voltage-dependence is near-quartic, in this case any permittivity gradients in the suspension are caused by volume fraction gradients and there is no direct dependence on applied voltage [98]. The expression for calculating the force on the fluid is exact and given the laminar nature of the flow profile is very likely to be physically accurate. The slight decrease in dielectrophoretic maximum velocity with increasing initial volume fraction is also expected, as can be seen by examining eq. 5.15 for the dielectrophoretic force on a single particle, correcting for particle volume fraction, derived previously using the chemical potential approach taken in this work [143]. This equation reduces to the classic case of the dielectrophoretic force in the limit of zero volume fraction but for non-zero volume fraction and a negative value of β (negative dielectrophoresis), increasing volume fraction will lead to a decrease in the dielectrophoretic force a particle experiences. Viscosity effects from increasing maximum volume fraction and assembly size ($2\mu\text{m}$ case) will also cause a decrease in the dielectrophoretic velocity, and additionally perturbations of the electric field near the minimum gap between electrodes/electrode edges (location of maximum DEP force) could also contribute to this change although this would only be an issue for the larger assembly sizes.. The change in fluid velocity with initial volume fraction (order of magnitude increase in initial volume fraction led to order of magnitude increase in fluid velocity) is also expected to be nearly linearly-dependent, as the force on the fluid is proportional to particle volume fraction. These trends are also present for $2\mu\text{m}$ particles, although fewer voltages were studied for that case. The volume fraction proportionality of maximum fluid velocity is still linear, although with a higher constant of proportionality. This can be attributed to the large size of the assembled structure at $c_0 = 1 \text{ vol.}\%$ and high volume fraction within the assembly significantly affecting the viscosity of the suspension over a large area, illustrated quite clearly in the 5V case in Fig. 5.10d).

$$\vec{F}_{\text{DEP}} = \frac{\varepsilon_0 v_p}{2} \left(\frac{d\varepsilon_s}{dc} \right) \nabla \langle |\vec{E}|^2 \rangle = \frac{2\pi r_p^3 \varepsilon_0 \varepsilon_m \beta}{(1 - c\beta)^2} \nabla \langle |\vec{E}|^2 \rangle \quad (5.15)$$

For $0.32\mu\text{m}$ particles at any initial volume fraction in DMSO, no clear structure could be discerned using optical microscopy during assembly, although the larger accumulation of materials near the center of the microelectrodes after medium evaporation indicated that in fact there was some degree of assembly. This is attributed to the small size of particles, low refractive index contrast and low overall volume fraction of particles in the region of interest. The $2\mu\text{m}$ particle case in DMSO was observable however, and onset of electric field induced aggregation was observed when switching between 0.25V and 0.5V, which is consistent with the predicted critical electric field strength required for aggregation as calculated with the Khusid/Acrivos framework. The experimental results for a $0.5\mu\text{L}$ droplet with $c_0 = 0.1$ vol. % in DMSO are shown in Fig.5.13, for 0.5, 2.5, 5 and 20V. As can be seen from this figure, the experimentally obtained assemblies are all larger than the simulated results for $c_0 = 0.1$ vol.%, (Fig. 5.8) and are in fact closer size-wise to the results obtained from assuming an initial volume fraction of 1% (Fig. 5.9), although this still under predicts the size of the assembled structure. Furthermore, looking at the 5V case for $2\mu\text{m}$ particles, Fig. 5.13c), it can be observed that there are in fact multiple layers of particles stacked in the assembly. Even at lower voltages, the only confirmed monolayer-sized assembly happened in the 0.5V case Fig. 5.13a), beyond this voltage the assembly would always be at least a few layers thick. The overall structure transitioned from a more square shape (2.5V) to more rounded shapes (5V-10V) and finally to a diamond (20V). These experimental results were similar to previous results obtained in our group for $1\mu\text{m}$ particles in DI water at larger volume fractions and droplet sizes, shown in Fig. 5.14, and where the structures are more clearly observable over a wider range of conditions and again match with the simulations, Fig. 5.15, in terms of overall possible shapes but not size. 2d simulations of $1\mu\text{m}$ silica particles in water showed similar behavior to that of larger DMSO particles, in that fluid

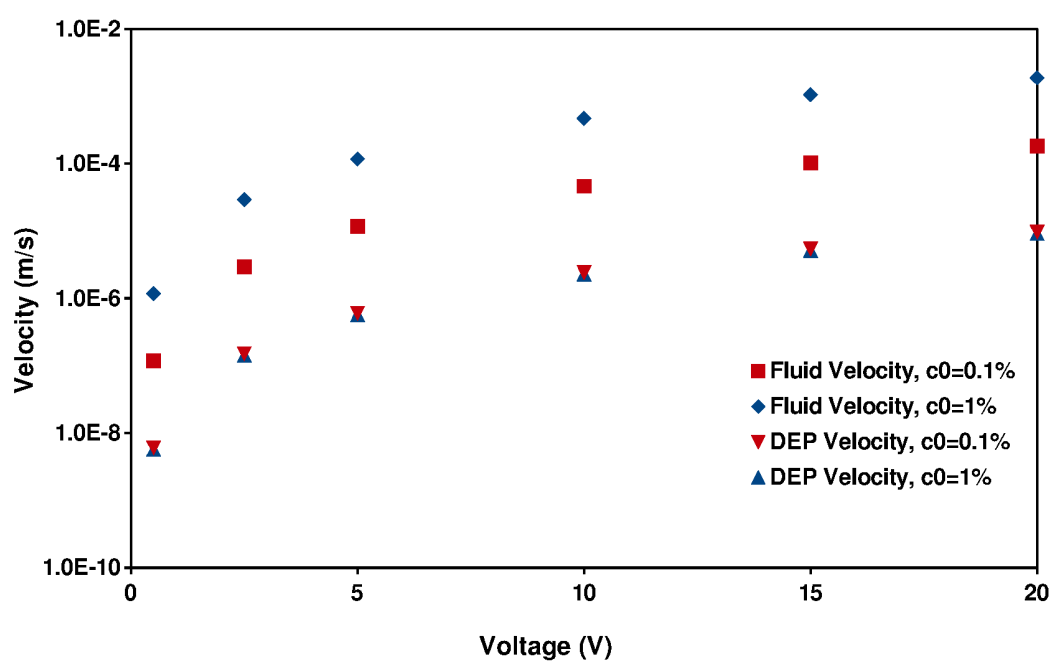


Figure 5.11: DEP and Fluid Velocities (m/s) as a function of Voltage for $0.32\mu\text{m}$ silica in DMSO

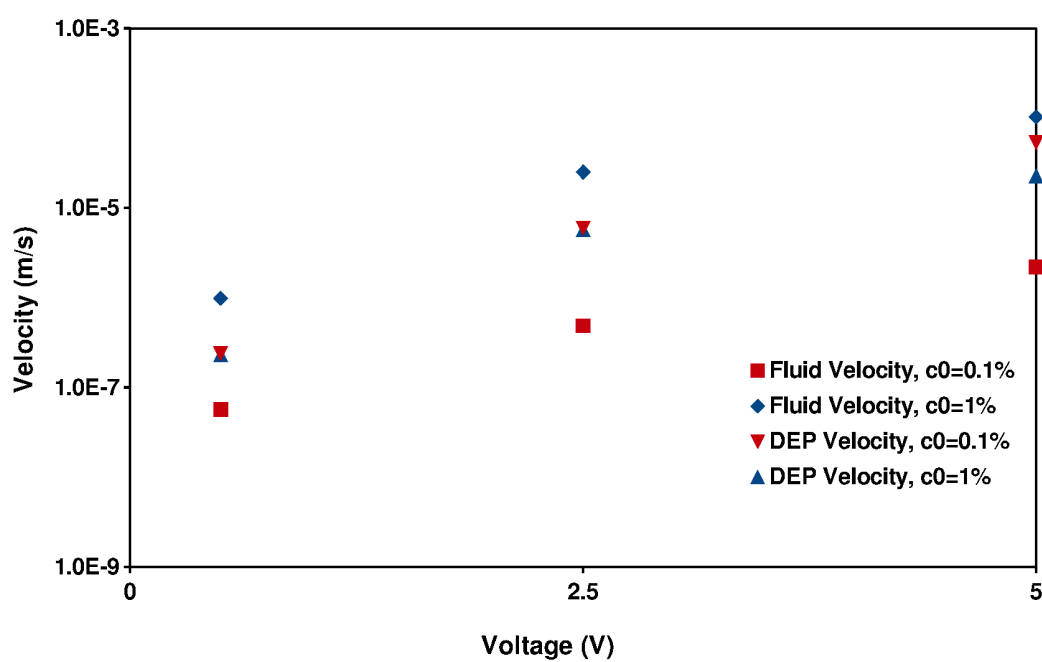


Figure 5.12: DEP and Fluid Velocities (m/s) as a function of Voltage for $2\mu\text{m}$ silica in DMSO

flows played a significant role in the steady-state c profile but were of a closer order of magnitude to the dielectrophoretic/electrically-induced velocity. The DI water suspension optical microscopy images are far clearer but also show that there are multiple particle layers even for small droplets. These results are a clear indication that sedimentation is a relevant force in the system, as well as that the z -component of the electric field force also plays a role in shaping the assembly (g_z, E_z). Both of these effects are neglected when dealing with a 2d assembly process assumed to take place on the microelectrode surface. In spite of the very low suspending liquid volume and spreading nature of DMSO this system cannot be accurately represented by a two-dimensional approximation. However, the relevance of induced fluid flows on the assembly process that were determined by these simulations is clear even from a 2d approximation. The effect of gravity would be the introduction of an additional convective force, which could potentially mitigate some of the impact on assembly shape that diffusion/fluid flow has leading to a result closer to that found for larger particles where the impact is larger on the assembly size compared to the shape.

Experimental confirmation of the fluid velocities and presence of rolls in a refractive-index matching medium are challenging as visualizing individual particles is also difficult, however, these types of rolls are consistent with previous experimental data collected by Docoslis and Alexandridis [151]. Upon activation of an applied electric field, fast swirling motions of particles can be observed for $1.5\mu\text{m}$ silica in water. Videos of these experiments are available on the authors website [151]. The need for accounting for flow effects and dealing with fully 3d systems is illustrated by the assembly results shown in Figures 5.16 - 5.18, which are optical microscopy and SEM images of $1.5\mu\text{m}$ silica particles immobilized by using a water-pluronic F-127 medium and allowing the droplet to evaporate beyond the gelation concentration after reaching a steady-state assembly. These structures, shown in Fig. 5.16 clearly perturb the electric field significantly at all applied voltages, with the exception over the very dilute case. There are multiple layers and assemblies show distortions at the edge of structures and at the center of the interelectrode channel that are likely the result of fluid

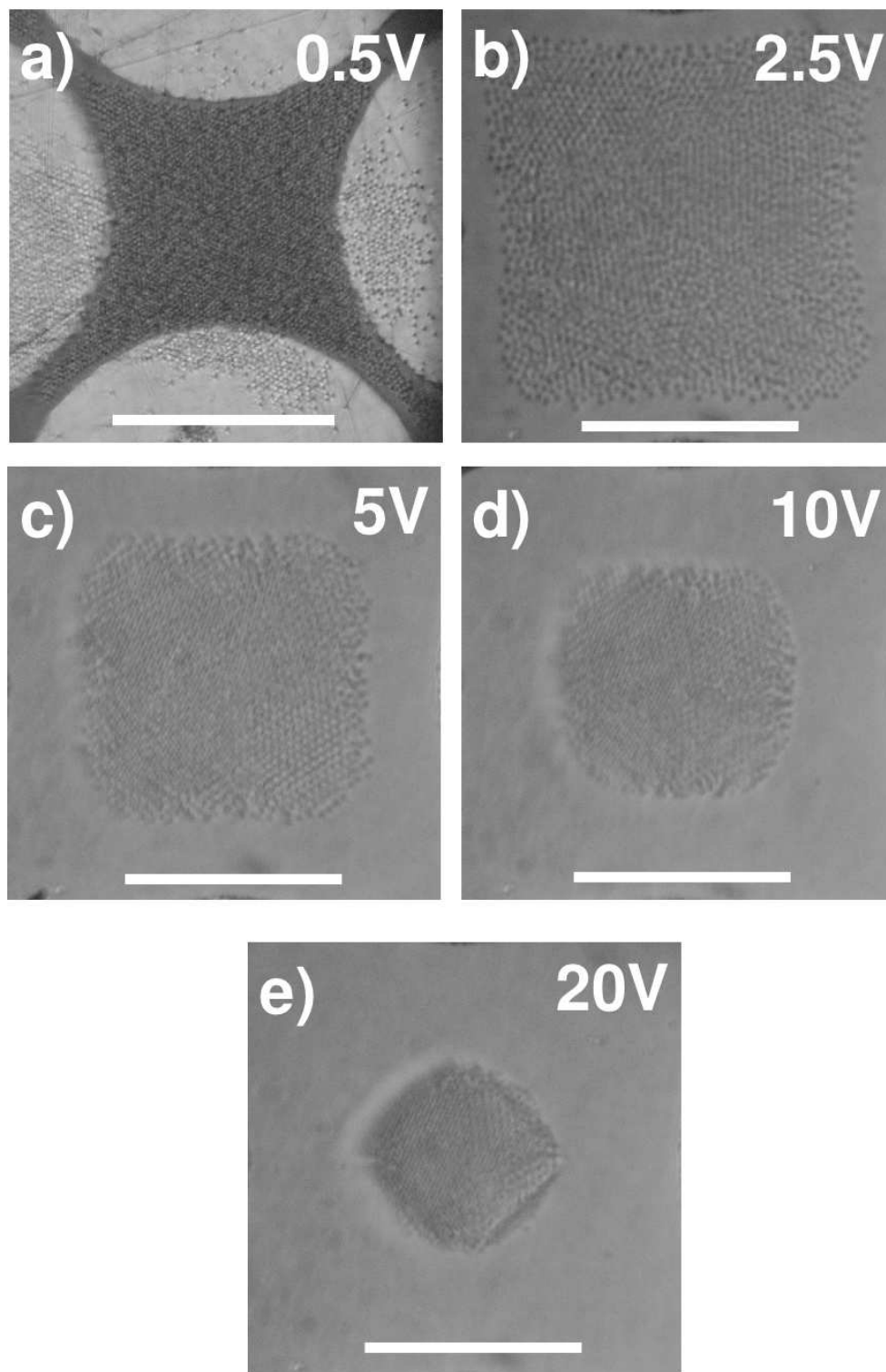


Figure 5.13: Electric Field Induced Assembly Profiles for $2\mu\text{m}$ silica in DMSO, $c_0 = 0.1$ vol.%.
a) 0.5V, b) 2.5V, c) 5V, d) 10V, e) 20V [scalebar: a) is $100\mu\text{m}$, b) through e) $50\mu\text{m}$]

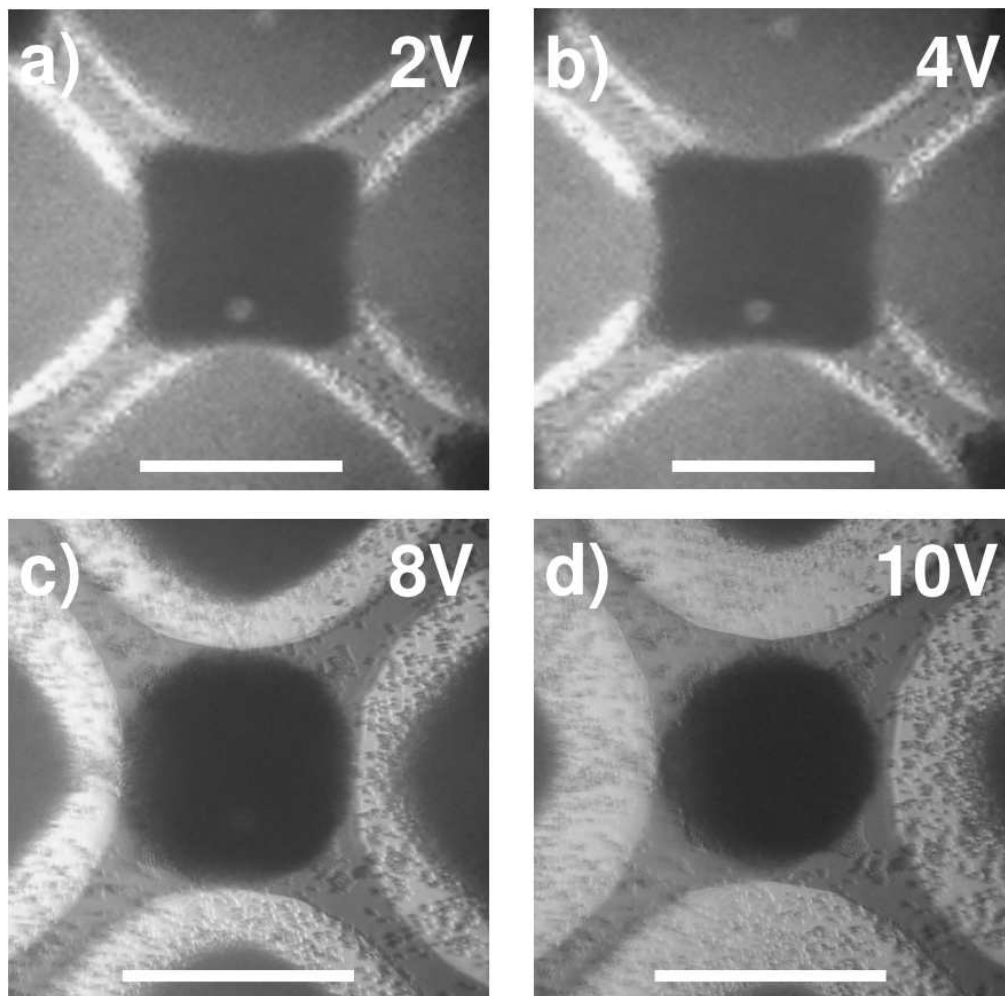


Figure 5.14: Electric Field Induced Assembly Profiles for $d_p = 1\mu\text{m}$ silica in H_2O , $c_0 = \text{vol. } 1\%$

a) 2V, b) 4V, c) 8V, d) 10 V [scalebar is $50\mu\text{m}$]

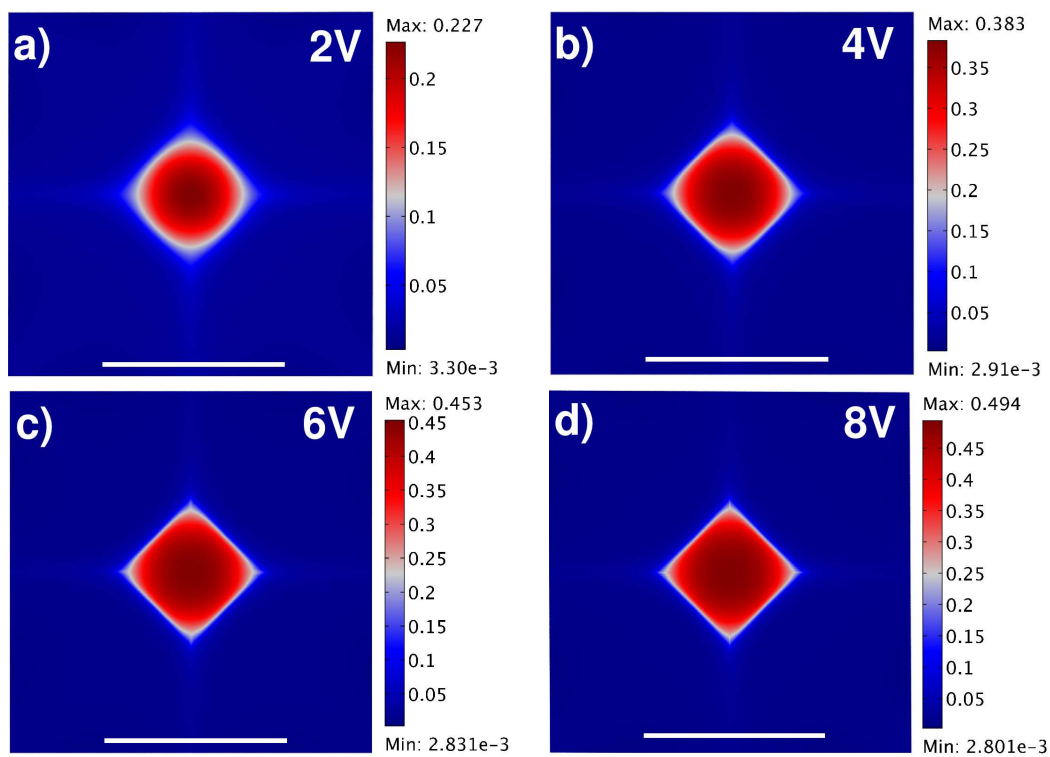


Figure 5.15: Particle Volume Fractions, Non-equilibrium Case, for $d_P = 1\mu\text{m}$ silica in H_2O , $c_0 = 1\text{ vol.}\%$

a) 2V, b) 4V, c) 6V, d) 8 V [scalebar is $50\mu\text{m}$]

flows. A two-dimensional approximation is only able to provide qualitative information on the overall shape of assemblies, but is illustrative as to the relative influence of entropic and electrical and the induced fluid flows that result from these forces.

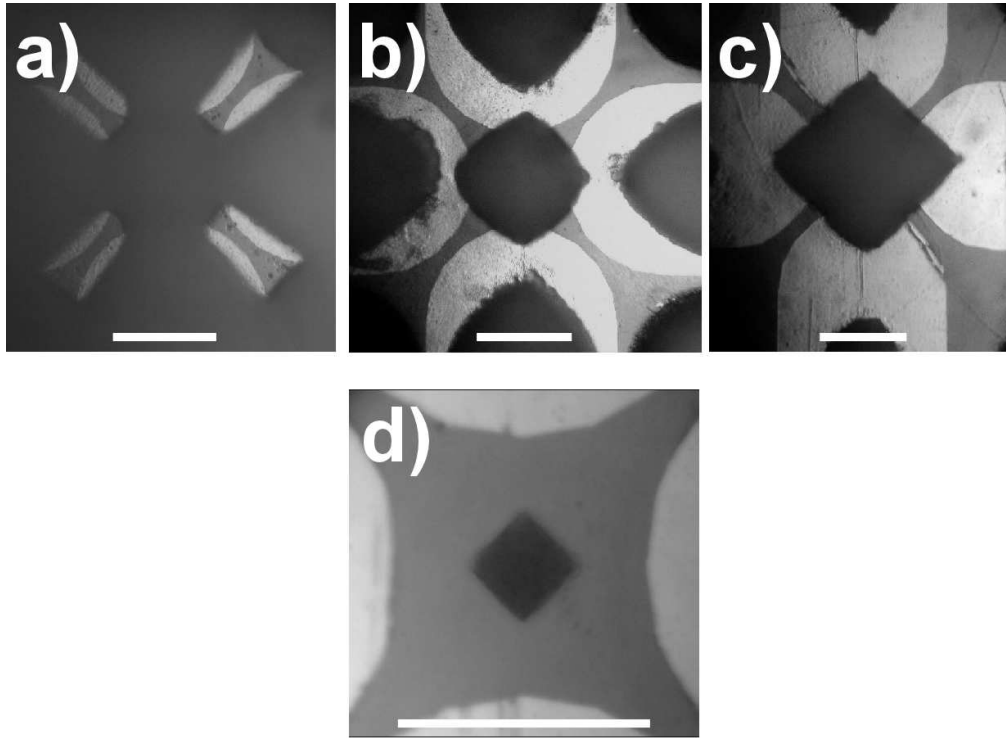


Figure 5.16: Electric Field Induced Assembly Profiles for $d_P = 1.5\mu\text{m}$ silica in H_2O -3.8vol.% Pluronic F-127

a) 5V, $c_0=4.4$ vol.% b) 10V, $c_0=4.4$ vol.% c) 20V, $c_0=4.4$ vol.% d) 20 V, $c_0=0.03$ vol.% [scalebar is $100\mu\text{m}$]

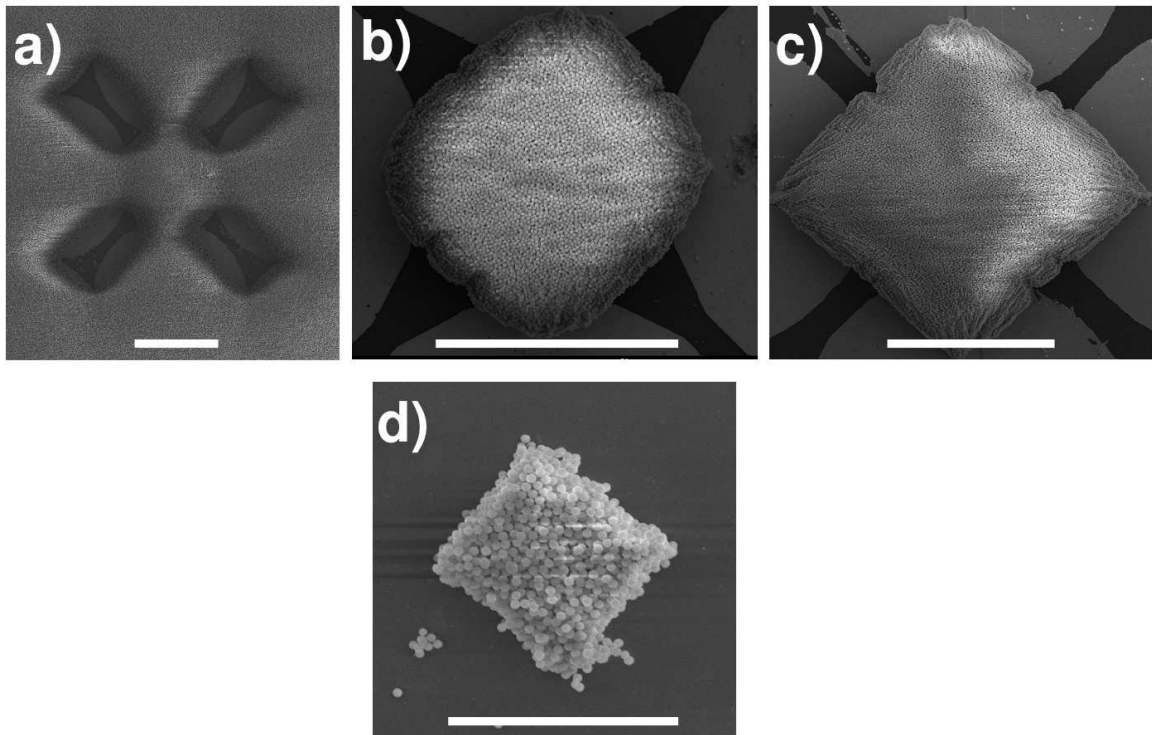


Figure 5.17: SEM Images for $d_P = 1.5\mu\text{m}$ silica in H_2O -3.8vol.% Pluronic F127
a) 5V, $c_0=4.4$ vol.% b) 10V, $c_0=4.4$ vol.% c) 20V, $c_0=4.4$ vol.% d) 20 V $c_0=0.03$ vol.% [scalebar: a) through c) $100\mu\text{m}$, d) $20\mu\text{m}$]

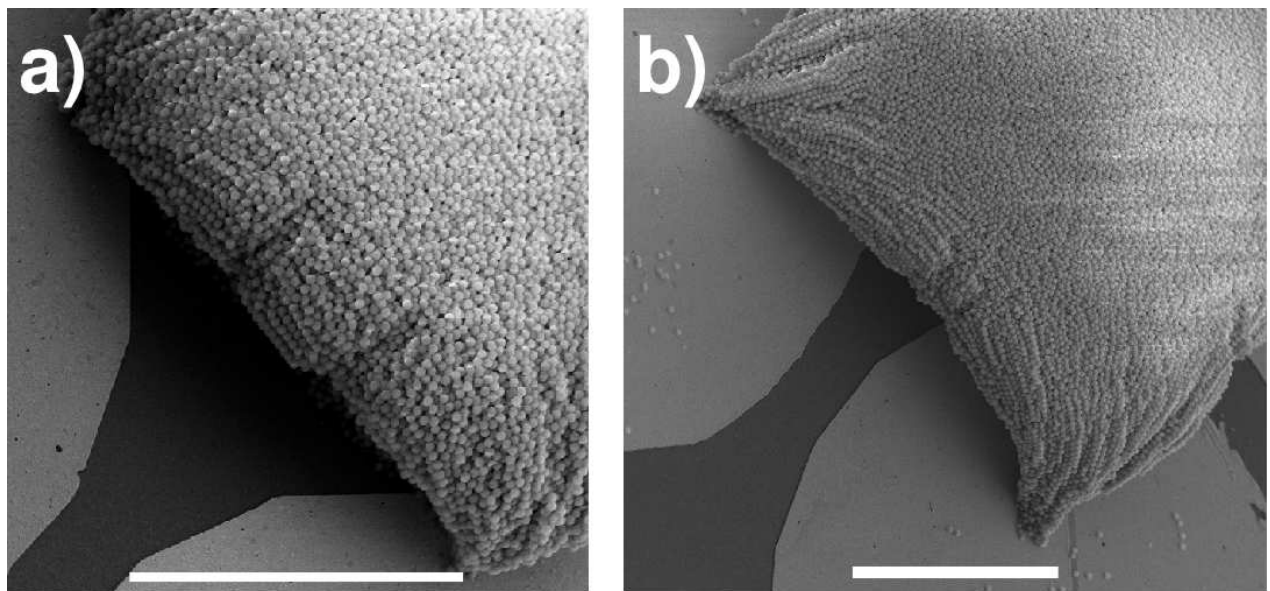


Figure 5.18: Zoomed SEM of $1.5\mu\text{m}$ silica in H_2O with 3.8vol.% Pluronic F-127
a) 10V, $c_0=4.4$ vol.% b) 20V, $c_0=4.4$ vol.% [scalebar is $50\mu\text{m}$]

5.5 Conclusions

The non-uniform electric field (dielectrophoretic) driven assembly of colloidal particles using a quadrupolar microelectrode geometry was explored by simulations based on a thermodynamic framework. In this framework forces on the particles and fluid are calculated in terms of a chemical potential gradient, where electrical (based on assuming Maxwell-Wagner polarization) and entropic (based on assuming hard-sphere contributions calculated using the Carnahan-Starling equation of state) terms are assumed to be the two primary contributions. Simulations of the behavior of two different sizes of silica particles ($0.32\mu\text{m}$ and $2\mu\text{m}$) in DMSO, a near-index matching medium, were undertaken using the finite-element based software package Comsol MultiphysicsTM. The stationary fluid or equilibrium case was compared with the non-stationary or non-equilibrium case and it was found that the non-equilibrium solution is substantively different in both shape and size. Analysis of the magnitudes and spatial profile of the dielectrophoretic and fluid velocities indicated that at all but the very lowest of initial volume fractions and voltages the fluid velocity dominates. The numerical solution indicated that the fluid velocity induced by electrical and entropic forces could be up to the order of mm/s, which is substantial for microelectrode and particle scale. The velocity profile of the fluid contained rolls or vortexes near the center of the space between microelectrodes which played an important roll in shaping the assembly. Interestingly, these flows were generated purely based on the electrical and entropic contributions of particles in an applied electric field, versus some external flows to the system. The fluid flow behavior within the system can be taken as analogous to electrothermal flows, without the need for electric field induced heating of an electrically conductive medium to generate temperature and thereby, permittivity and conductivity gradients.

It was also found based on optical microscopy observation of experiments that using both a small liquid volume and spreading liquid to create a thin liquid film were not sufficient to eliminate z -component based effects. It was observed for $2\mu\text{m}$ particles in DMSO by optical

microscopy that at low initial volume fractions multiple particle layers would form even at lower applied voltages. It was also found that $0.32\mu\text{m}$ silica particles were not observable in our system, even at the highest voltages/largest theoretical assemblies, as the refractive index contrast was too low for effective visualization. Preliminary 3d simulations, performed at uniform particle concentration/volume fraction, show that there is a significant electric-field induced fluid velocity component in the z-direction for both particle sizes studied, with the relative influence compared to the direct dielectrophoretic force diminishing as the particle size increased.

The important conclusion from this work is that the influence of fluid flow can be important over a wide range of conditions, affecting primarily size of assemblies when electrically-driven convection forces dominated (larger particles/voltages) and both the shape and size of assemblies when entropic diffusive forces dominated (smaller particles/voltages). These fluid flows have been observed by previous experiments and given the nature of microfluidic flows (very low Reynolds number), the order of magnitude of the prediction should be very accurate. This has important implications for understanding the dynamics of the assembly process, as well as for predicting the steady-state colloid profile for using dielectrophoresis to shape colloidal structures. In particular, the maximum fluid velocity in the system was found to be approximately linearly proportional to the initial volume fraction of particles for both sets of particles, with a closer to 1:1 correspondence at smaller particles and a higher ratio for larger particles which was attributed to the larger size of assembly and higher volume fractions achieved using equivalent voltages for these particles. The framework presented in this paper shows great promise for being able to enhance understanding of the interplay between entropic, electrical and fluids forces during non-uniform electric field driven assembly. Future work is planned in regards to expanding the simulation framework into three-dimensions, which will greatly increase the numerical complexity of the problem and may necessitate the use of more sophisticated numerical techniques compared to FEM for solving the time-dependent PDEs.

Chapter 6: Electric-Field Induced Phase Transitions of Dielectric Colloids

Abstract

The thermodynamic framework for predicting the electric-field induced fluid like-solid like phase transition of dielectric colloids developed by Khusid and Acrivos (1996) is extended to examine the impact of multiscattering/multiparticle effects on the resulting phase diagrams. This was accomplished using effective permittivity models suitable both over the entire composition region for hard spheres ($0 \leq c < c_{max}$) and for multiple types of solid packing structures (RCP, FCC, BCC). The Sihvola-Kong model and the self-consistent permittivity model of Sen et al. were used to generate the coexistence (slow phase transition) and spinodal (rapid phase transition) boundaries for the system and compared to assuming Maxwell-Garnett permittivity. It was found that for larger dielectric contrasts between medium and particle that the impact of accounting for multiscattering effects increased and that there was a significant shift in the resulting phase diagrams. Results obtained for model colloidal systems of silica-DMSO and silica-isopropanol showed that critical electric field strength required for phase transitions could rise by up to approximately 20% when considering multiparticle effects versus the isolated dipole case. The impact on the phase diagrams was not limited purely to the direct effect of volume fraction on permittivity and particle dipoles but also on the curvature of the volume fraction dependence. This work stresses the importance of accounting for particle effects on the polarization of colloidal suspensions, which has large implications for predicting the behavior of electrorheological fluids and other electric-field driven phenomena.

6.1 Introduction

The phenomena of electric field induced phase transitions of colloidal suspensions is a well-established field, with many interesting applications. Electric fields have been used to drive colloidal crystal formation with lattice structures not normally obtainable via other methods for templating colloidal crystals and other transitions of interest. These lattice structures include colloidal martensite (body-centered tetragonal lattice) from refractive index matched silica-DMSO-water suspensions, large scale polystyrene colloidal crystals in aqueous suspension and drive the phase transition and aligned block copolymer micelles [86, 95, 119, 152, 153]. Additionally, these types of phase transitions also govern electrorheological (ER) fluids, where the phase transition of the suspended solid phase into a more concentrated form causes a large shift in the rheological behavior (viscosity) [154]. More specifically, particles in the suspension can align into chains (1d analog of 2d colloidal crystals) and this chaining behavior can significantly impact the viscosity in a system.

To predict the phase transition, a number of different frameworks have been approached from continuum mechanics, molecular/brownian dynamics type approach to solve for the motion of individual particles to treating the pattern formation in terms of the classic Ginzburg-Landau function and solving for concentration profiles by variational principles [105, 155, 156]. Of particular interest is the thermodynamic framework first developed by Khusid and Acrivos and extended to account for interparticle interactions and a wide range of frequency-dependent behavior [144, 145, 157]. In this approach, the properties of the overall suspension, along with any electric-field induced phases, are treated in a continuum manner. Using Maxwell-type polarization, the authors were able to explore the phase behavior over a wide range of possible particle and medium combinations. With the theory developed, the authors were able to calculate the spinodal and coexistence boundaries for a given particle-medium combination, as well as conditions where aggregation is inhibited by interparticle interactions. This approach has been utilized by a number of authors for phase

transitions specifically related to ER fluids, as well as for examining suspension behavior in cases with external fluid flows and electric fields [146, 158–162]. This framework was also the basis for predicting pattern formation in non-uniform electric fields that we have used in previous work.

In this work, we propose to examine the influence of multiscattering/multiple particle effects on the overall phase transitions of dielectric particles in a non-conducting suspension. The original derivation is based on assuming that the Maxwell-Garnett model holds over the entire composition range and for any type of resulting “solid” phase structure, which is to say it assumes that the dipole coefficient of a particle in the mixture is equal to that of a single isolated dipole. This type of assumption has been shown to perform very poorly for concentrated suspensions and it is worth examining the validity of it due to the importance of being able to accurately predict electric-field driven colloidal phase transitions. To accomplish this we utilize two effective permittivity models, the model of Sihvola and Kong (1988) and Sen et al. (1981), which have been shown experimentally to describe permittivity (and conductivity) behavior over a wide range of compositions and for different types of solids-packings (face centered cubic, body centered cubic, simple cubic, random close packed, etc.) with the overall framework proposed by Khusid and Acrivos to calculate the resulting phase diagrams. The effect of permittivity model and the degree of change of dipole coefficient with particle packing are examined on the coexistence (slow phase transition/aggregation region) and spinodal (fast phase transition/aggregation region) lines for a hard sphere suspension, with the diverging region of high concentration treated as a random close-packed structure (RCP).

6.2 Theoretical Background

For a suspension of dielectric (non-conducting) particles the average electrical energy density, W_{elec} , can be derived as [145]:

$$W_{elec}(c, \langle |\vec{E}^2| \rangle) = \frac{1}{2} \varepsilon_s(c) \langle |\vec{E}^2| \rangle \quad (6.1)$$

where $\varepsilon_s(c)$ is the dielectric constant of the suspension and $\langle |\vec{E}^2| \rangle$ is the time-averaged magnitude of the electric field norm.

The Helmholtz free energy of the suspension is taken as a combination of entropic and electrical contributions:

$$F = \frac{k_B T}{v_p} f_0 V - W_{elec} V \quad (6.2)$$

where in eqn. 6.2 f_0 represents the entropic contribution to the free energy which is a function of the volume fraction, c , and is determined by:

$$f_0 = c \ln\left(\frac{c}{e}\right) + c \int_0^c \left(\frac{Z-1}{c} dc \right) \quad (6.3)$$

From the free energy, the osmotic pressure, Π , and chemical potential, μ , of the suspension can be derived:

$$\Pi = \frac{k_B T}{v_p} c Z + W_{elec} - c \left(\frac{dW_{elec}}{dc} \right) \quad (6.4)$$

$$\mu = \frac{k_B T}{v_p} \left(\frac{df_0}{dc} \right) - \left(\frac{dW_{elec}}{dc} \right) \quad (6.5)$$

Substituting eqn. 6.1 into eqns. 6.4 and 6.5 results in state equations for the suspension depending on volume fraction, c , and the time-averaged electrical field norm, $\langle |\vec{E}^2| \rangle$ [144, 145, 157]:

$$\mu = \frac{k_B T}{v_p} \frac{df_0}{dc} - \frac{1}{2} \left(\frac{d\varepsilon_s}{dc} \right) \langle |\vec{E}|^2 \rangle \quad (6.6)$$

$$\Pi = \frac{k_B T}{v_p} c Z + \left[\varepsilon_s - \frac{1}{2} c \left(\frac{d\varepsilon_s}{dc} \right) \right] \langle |\vec{E}|^2 \rangle \quad (6.7)$$

The entropic contributions can be determined from an equation of state (EOS) for hard-spheres. As with the work of Khusid and Acrivos, we choose the Carnahan-Starling EOS with the diverging region packing chosen for randomly closed packed (RCP) structures ($c_{max} = 0.64$).

$$Z = \begin{cases} \frac{1 + c + c^2 - c^3}{(1 - c)^3} & 0 < c \leq 0.5 \\ \frac{1.85}{0.64 - c} & 0.5 < c < 0.64 \end{cases} \quad (6.8)$$

The coexistence line, or two-phase region, is described by equating the chemical and osmotic pressure of each phase, as in eqn. 6.9

$$\mu(c_1) = \mu(c_2) \quad \text{and} \quad \Pi(c_1) = \Pi(c_2) \quad (6.9)$$

The spinodal line, or region beyond which a random suspension of particles becomes unstable, is determined from setting the derivative of osmotic pressure with respect to volume fraction equal to zero. This represents the series of (c, E) points where the free energy shifts from convex to concave [157]. Expanding out this derivative in terms of the previously defined terms yields eqn. 6.10:

$$Z + c \left(\frac{dZ}{dc} \right) - \frac{1}{2} c \left(\frac{v_p}{k_B T} \right) \left(\frac{d^2 \varepsilon_s}{dc^2} \right) \langle |\vec{E}|^2 \rangle = 0 \quad (6.10)$$

The critical point, common to both the spinodal and coexistence curves, is determined by the inflection point of Π with respect to volume fraction, meaning the critical concentration (c_{cr}) and field strength ($\langle |\vec{E}_{cr}|^2 \rangle$) can be determined from the solution of eqns. 6.10 and 6.11:

$$2\left(\frac{dZ}{dc}\right) + c\frac{d^2Z}{dc^2} - \frac{1}{2}\left(\frac{v_p}{k_BT}\right)\left[\left(\frac{d^2\varepsilon_s}{dc^2}\right) + c\left(\frac{d^3\varepsilon_s}{dc^3}\right)\right]\langle|\vec{E}|^2\rangle = 0 \quad (6.11)$$

In their previous work, Khusid and Acrivos considered the suspension permittivity to be described by the Maxwell-Garnett equation directly or derived an equivalent result using a cell model, with the expression shown in eqn. 6.12.

$$\varepsilon_s = \varepsilon_m + \frac{3c(\varepsilon_p - \varepsilon_m)\varepsilon_m}{\varepsilon_p + 2\varepsilon_m - c(\varepsilon_p - \varepsilon_m)} \quad (6.12)$$

By using this expression, the authors were able to explore the effect of numerous combinations of particle, ε_p , and medium permittivity, ε_m , on the coexistence and spinodal lines of the suspension. The results are non-dimensional, that is could be scaled in terms of critical applied field, and only depend on the dielectric contrast between medium and particle (Clausius-Mossotti factor). However, using Maxwell or Maxwell-Garnet type polarization treats the dipole coefficient of particles as being independent of particle concentration (volume fraction) meaning the dipole coefficient of the mixture is that of an isolated particle. This is a tenuous assumption for higher volume fractions and for a system where there are potentially phase changes (“fluid” to “solid”). It has been shown that the dipole approximation can be accurate even for spheres in contact when $2/5 < \varepsilon_p/\varepsilon_m < 4$, however this implies using a particle-medium combination with an extremely small permittivity difference which is not necessarily the case for many systems of interest such as silica-DMSO or silica-water [163]. Fortunately, a number of alternative expressions for suspension permittivity exist which account for these effects. For our work we chose the semi-empirical model derived by Sihvola and Kong, eqn. 6.13, as well as the model of Sen et al., eqn. 6.14, both of which have been used previously for correlating permittivity (and conductivity) at high solid volume fractions with various solid packing structures for monodisperse and polydisperse suspensions [147, 164–166].

$$\varepsilon_s = \varepsilon_m + \frac{3c(\varepsilon_p - \varepsilon_m)[\varepsilon_m + a(\varepsilon_s - \varepsilon_m)]}{3\varepsilon_m + 3a(\varepsilon_s - \varepsilon_m) + (1 - c)(\varepsilon_p - \varepsilon_m)} \quad (6.13)$$

$$\left(\frac{\varepsilon_p - \varepsilon_s}{\varepsilon_p - \varepsilon_m} \right) \left(\frac{\varepsilon_m}{\varepsilon_s} \right)^{(1/3)} = 1 - c \quad (6.14)$$

The Sihvola-Kong formulation introduces an empirical parameter, a , representing concentration effects on the dipole coefficient, allowing for multibody/particle effects to be accounted for. Choosing the value of a as zero reduces the Sihvola-Kong model to Maxwell-Garnett type mixing, while for random close packed structures over a wide range of volume fractions it has been found that a value of $a = 0.2$ describes experimental data well [165, 166]. For other cubic lattice types (FCC, BCC), measured permittivity values fall somewhere between $a = 0.2$ and being described by the Sen et al. model. For increasing values of hard sphere packing fraction (c), the dielectric behavior for RCP structures also approaches that described by eqn. 6.14. The Sen et al. model is a self-consistent effective permittivity model and has been demonstrated experimentally to form the lower limit of permittivity versus volume fraction behavior for any type of emergent solid packing [165]. More complicated expressions involving multiple calculated or fitted parameters have been derived and used to very accurately describe the concentration dependence of suspension permittivity for FCC, BCC and other lattice structures, but for our purposes solving for the permittivity case falling between Maxwell-Garnett and Sen et al. is sufficient for examining the validity of the isolated dipole approximation compared with accounting for multiscattering effects on overall electric field driven aggregation behavior.

6.3 Results and discussion

6.3.1 Suspension Permittivity and Derivatives

In order to examine the influence of high volume fraction polarization effects on the resulting phase diagrams of electric-field induced aggregation, two model colloidal systems were considered. The first is silica-DMSO, which is a near-refractive index matched suspension suitable for colloidal crystallization. Refractive index matching eliminates attractive van der Waals interactions between particles, which can promote crystallization/phase change in either the presence or absence of an applied electric field and has been used for silica-DMSO and silica-DMSO/DMF and silica-DMSO/H₂O suspensions under the influence of an applied electric field to induce phase transitions [112, 119, 152, 167]. The resulting solid structure type has been identified as a body-centered tetragonal (BCT) crystal, but for our purposes we are interested primarily in demonstrating the influence of high volume fraction/solid structure effects versus specific lattice structure and will treat the suspension as a hard sphere suspension with the diverging region being that of a random close packed structure. Based on previous experimental work for cubic lattice types, the permittivity model of Sen et al. or Sihvola-Kong with a parameter between 0.2 and 0.3 is able to describe the observed behavior over the entire physical concentration range [165, 166]. To use the equations listed in the previous section for phase equilibrium, conductivity effects must be neglected. DMSO is well known to be an approximately non-conducting liquid over a wide frequency range ($\sigma_{elec} = 3 \times 10^{-3} \text{ mS/m}$), while for silica at 1MHz we can neglect any conductivity effects on the overall polarizability [20, 168]. At higher frequencies (MHz and above), the dielectric constant (relative permittivity) of silica can be taken as approximately 4.5 [20]. For the second system, silica-isopropanol (iPrOH) was considered in order to examine the impact of dielectric contrast between particle and medium on the resulting phase diagrams calculated assuming either Sihvola-Kong or Sen et al. permittivity behavior. Isopropanol has a smaller dielectric constant compared to DMSO and therefore has a smaller dielectric

contrast with silica and is also an insulating liquid ($\sigma_{elec} = 3 \times 10^{-4} \text{ mS/m}$) [169]. The relative permittivity of DMSO was taken as 46.8, while the value for isopropanol used was approximately 18 [170–172]. Given these particle and suspending liquid combinations the real part of the Clausius-Mossotti factor, $\beta = (\varepsilon_p - \varepsilon_m)/(\varepsilon_p + 2\varepsilon_m)$, can be determined as -0.43 and -0.33 respectively.

To explore the entire range of physically possible behavior for permittivity versus volume fraction, as well as comparison with using the Maxwell-Garnett approximation, the model of Sihvola and Kong was used with the adjustable parameter, a , having values of 0, 0.1, 0.2 and 0.3 as well as the model of Sen et al. As previously discussed, Sen et al. should form the lower limit to permittivity versus volume fraction curves and Maxwell-Garnett the upper limit so the entire range of physical behavior for the system is captured. Plots of permittivity versus volume fraction for silica-DMSO are given in Fig. 6.1 and for isopropanol Fig. 6.2 for the entire physical volume fraction range ($0 \leq c < 0.64$). As can be seen from these plots, the permittivity values are bounded between Maxwell-Garnett type behavior ($a = 0$) and values predicted using the model of Sen et al. which is the expected result. The absolute contrast between permittivity values is lesser in the case of silica-isopropanol versus silica-DMSO, which is also to be expected, and indeed the overall deviation between different models is much smaller in the case of isopropanol compared to DMSO [165]. However, the relevance of multiscattering/higher volume fraction effects on polarization are not limited purely to the value of the permittivity but to its curvature/rate of change with respect to c . Going back to eqns. 6.9, 6.10 and 6.11 for calculating the coexistence line, spinodal line and critical point respectively it can be seen that these equations depend not just on suspension permittivity but also on the first, second and third order derivatives with respect to volume fraction. In their original derivation based on Maxwell type polarization, Khusid and Acrivos noted that the signs of the permittivity derivatives plays a large role in determining the stability and behavior of electric-field induced phase transitions.

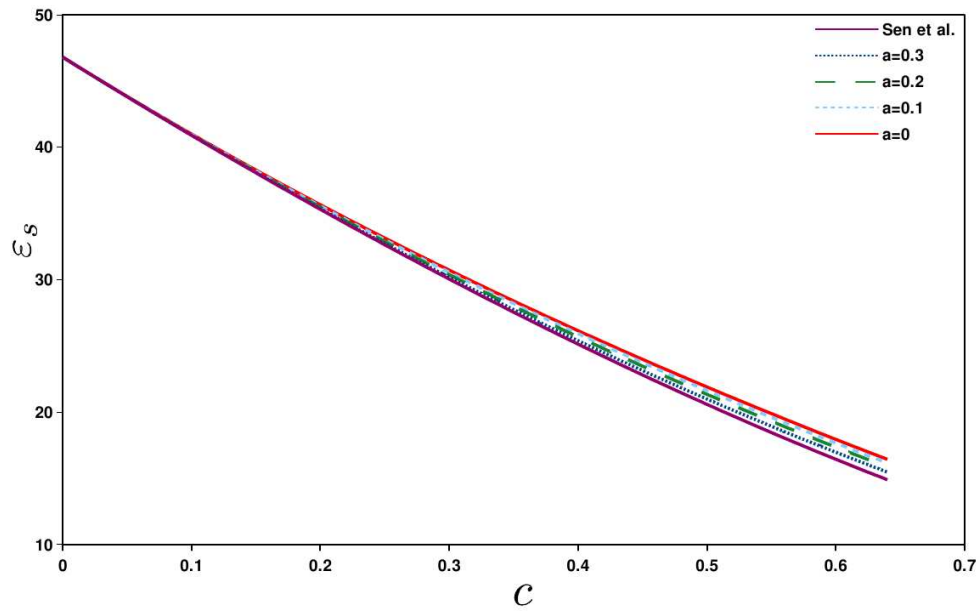


Figure 6.1: Suspension Permittivity versus Volume Fraction for Silica-DMSO

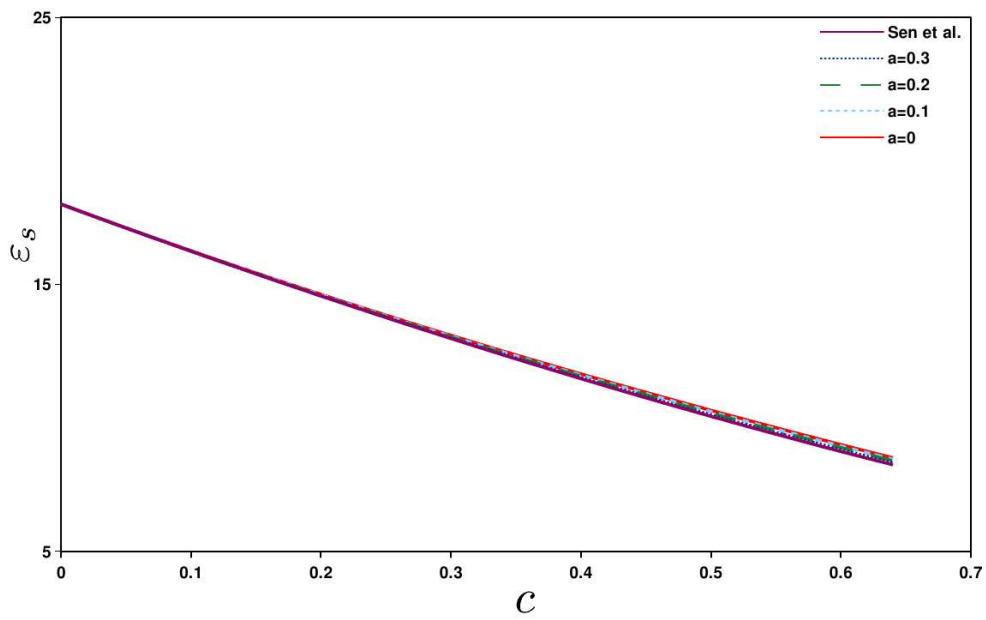


Figure 6.2: Suspension Permittivity versus Volume Fraction for Silica-iPrOH

The plots of $d\varepsilon_s/dc$ versus c for silica-DMSO and silica-iPrOH for the Sihvola-Kong and Sen et al. permittivity models are shown in Figures 6.3 and 6.4. For the entire composition range the values are negative for all chosen permittivity models, which is to be expected as each permittivity model predicts a monotonically decreasing permittivity for the case where the medium permittivity is greater than that of particle permittivity. The smallest magnitude versus particle volume fraction (upper most curves in Figures 6.3 and 6.4) represents Maxwell-Garnett type polarization, while the largest magnitude (lowest curves in Figures 6.3 and 6.4) is given by the model of Sen et al. The curves shift downwards with increasing value of the a parameter to account for volume-fraction related polarization effects. From examining eqns. 6.6 and 6.7, $d\varepsilon_s/dc$ impacts the osmotic pressure and chemical potential of the suspension directly, and the suspension permittivity will effect osmotic pressure. Changing the a parameter from 0 to 0.3 and Sen et al. shifts both the permittivity and first derivative of permittivity curves downwards, which will have competing effects on the magnitude of the osmotic pressure as decreasing suspension permittivity decreases osmotic pressure ($\downarrow \varepsilon_s, \downarrow \Pi$) and decreasing the first derivative of suspension permittivity increases osmotic pressure ($\downarrow d\varepsilon_s/dc, \uparrow \Pi$). These changes will also shift the chemical potential curve upwards, as decreasing the first derivative of suspension permittivity will increase the chemical potential ($\downarrow d\varepsilon_s/dc, \uparrow \mu$). For the spinodal transition to exist over the entire range of volume fractions, $d^2W/dc^2 > 0$, which is guaranteed explicitly by the nature of the Maxwell-Garnett permittivity model. In the case of Sihvola-Kong and Sen et al., for DMSO and iPrOH this also holds, although the trend with respect to volume fraction is inverted, as is illustrated in Figures 6.5 and 6.6 respectively. That is, for Maxwell-Garnett $d^2\varepsilon_s/dc^2$ monotonically decreases over the entire range of c , while for increasing values of a this trend ceases to hold. In the case of $a = 0.1$ the second derivative decreases over the entire range of c but the concavity is changed compared to $a = 0$, for $a = 0.2$ initially the second derivative increases slightly before decreasing and this is also the case for $a = 0.3$ while for Sen et al. $d^2\varepsilon_s/dc^2$ monotonically increases in value. The value of $d^2\varepsilon_s/dc^2$ for both DMSO and

iPrOH, and therefore d^2W/dc^2 . were positive over the entire range of compositions for all permittivity models studied, but the behavior versus c was still quite different compared with assuming Maxwell-Garnett type polarization. This shift in behavior will also effect the location of the critical point, as will the behavior of the third derivative. The third derivatives for silica-DMSO and silica-iPrOH are shown in Figures 6.7 and 6.8 respectively. The behavior of $d^3\varepsilon_s/dc^3$ varies considerably with the choice of permittivity model, from being a negative function which monotonically increases over the entire composition range for Maxwell-Garnett ($a = 0$), to being an almost constant negative value for $a = 0.1$, starting as a positive value and decreasing monotonically over the entire composition range for $a = 0.2$ and 0.3 while for the model of Sen et al. the third derivative is a positive, monotonically increasing function. This holds for both silica-DMSO and silica-iPrOH, although the shift in silica-iPrOH is relatively less than that of silica-DMSO, which holds for all derivatives. All of these results indicate that a shift in the coexistence and spinodal lines, and the critical point common to the onset of aggregation, should occur with accounting for c effects on ε_s .

6.3.2 Critical Point for Silica-DMSO and Silica-iPrOH

As a first measure of the influence of particle/multiscattering effects on permittivity and the subsequent impact on electric-field induced phase transitions, we examined how the critical point for these suspensions shifted with the different permittivity models as well as for different particle sizes. Previously, we have examined the use of the Khusid and Acrivos framework to predict the electric-field induced assembly of colloidal particles into larger structures of various shapes and sizes (Ch. 5), with the suspension permittivity described by Maxwell-Garnett polarization as in the original framework [144, 145, 157]. In that work, silica particles of $0.32\mu\text{m}$ and $2\mu\text{m}$ in DMSO were taken as the system of interest and the permittivity behavior of the system was assumed to be described by the Maxwell-Garnett model. This approximation was done in the interest of examining the influence of any fluid flows which arise due to gradients in chemical potential. However, it is now of interest for us

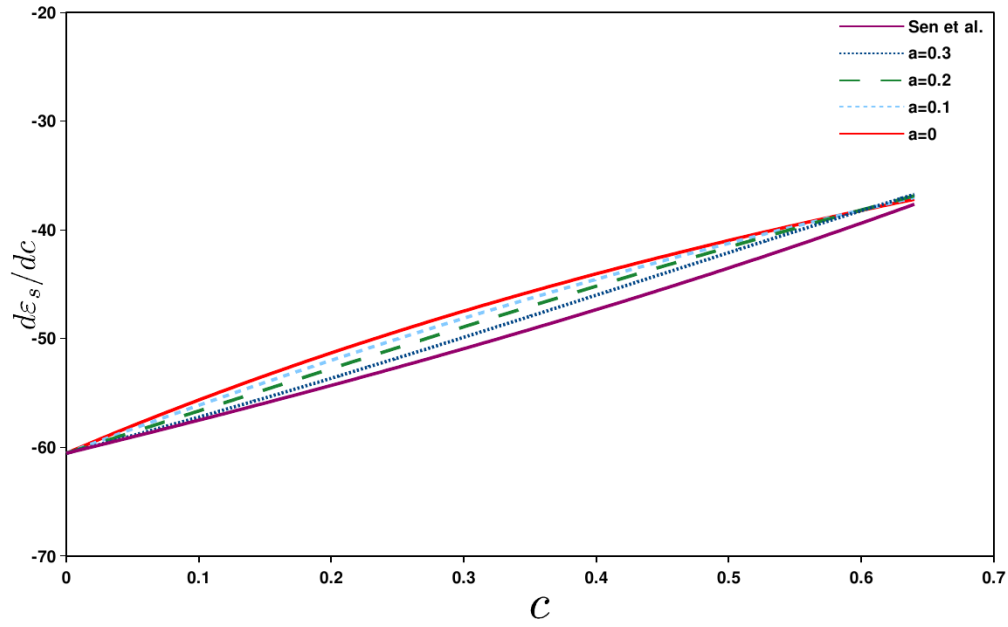


Figure 6.3: First Derivative of Suspension Permittivity with respect to Volume Fraction vs. Volume Fraction for Silica-DMSO

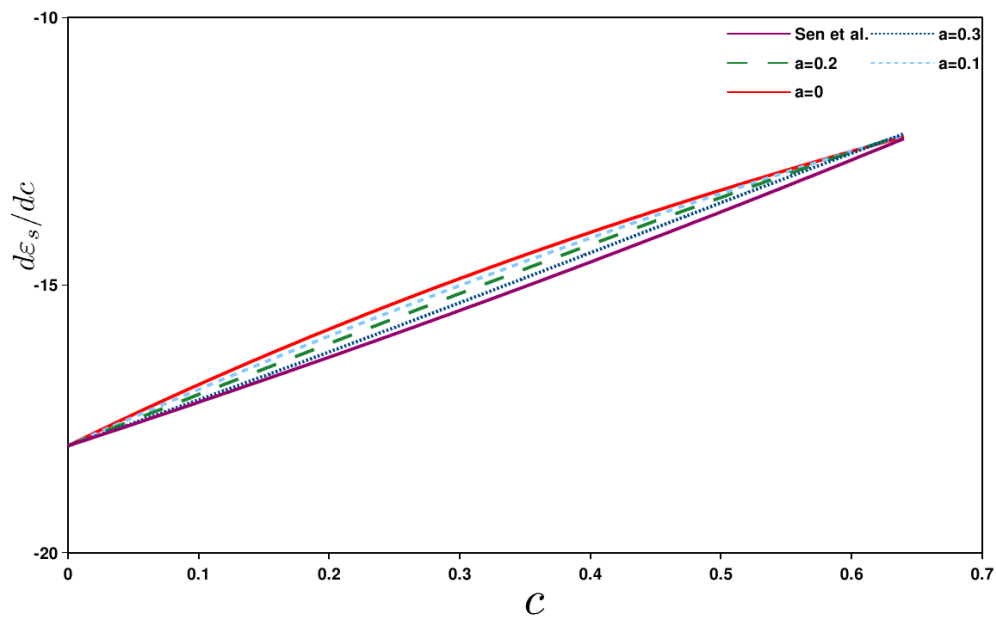


Figure 6.4: First Derivative of Suspension Permittivity with respect to Volume Fraction vs. Volume Fraction for Silica-iPrOH

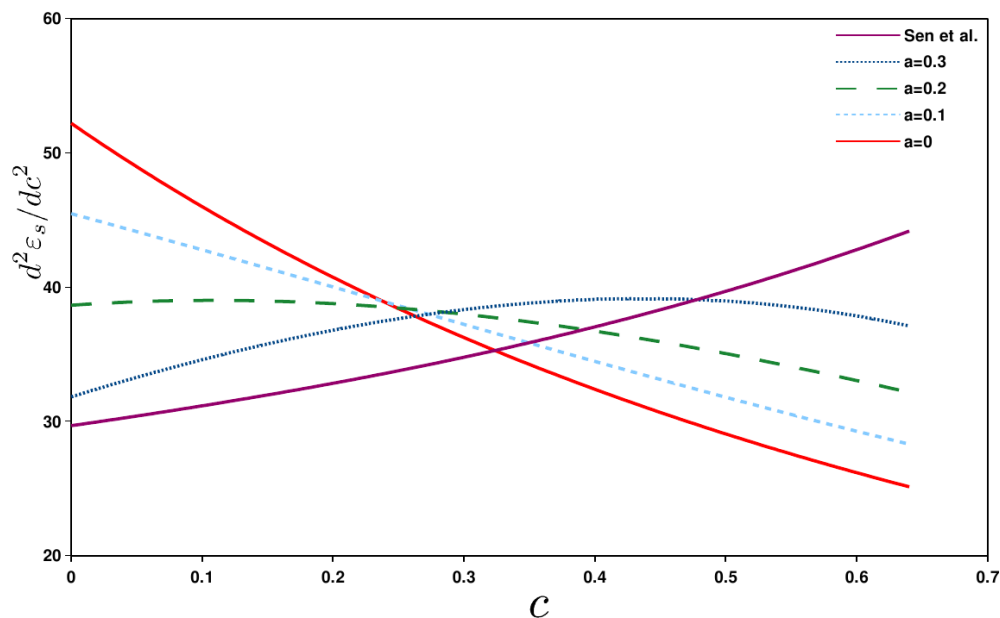


Figure 6.5: Second Derivative of Suspension Permittivity with respect to Volume Fraction vs. Volume Fraction for Silica-DMSO

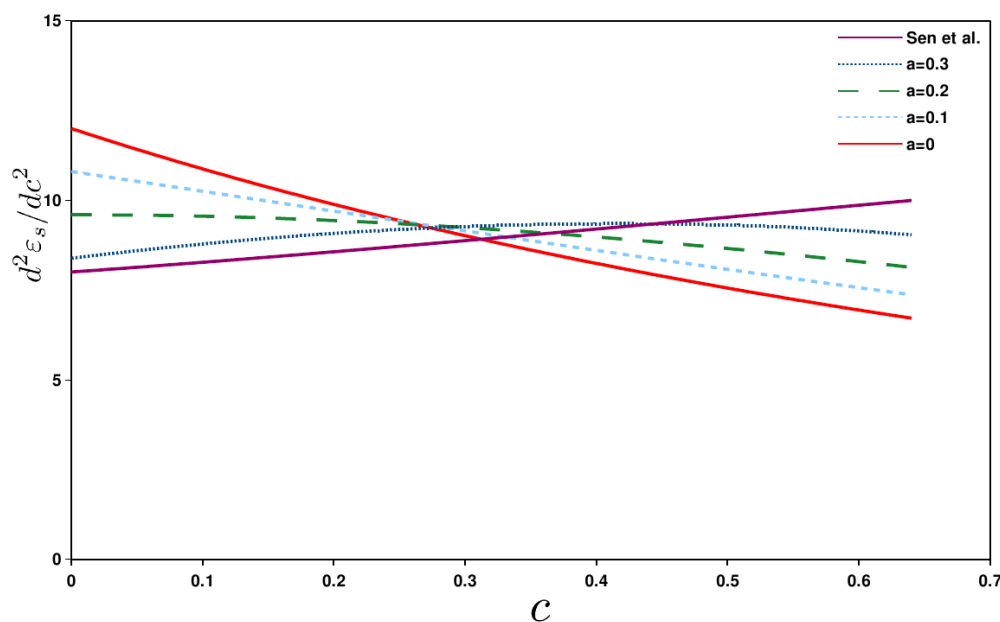


Figure 6.6: Second Derivative of Suspension Permittivity with respect to Volume Fraction vs. Volume Fraction for Silica-iPrOH

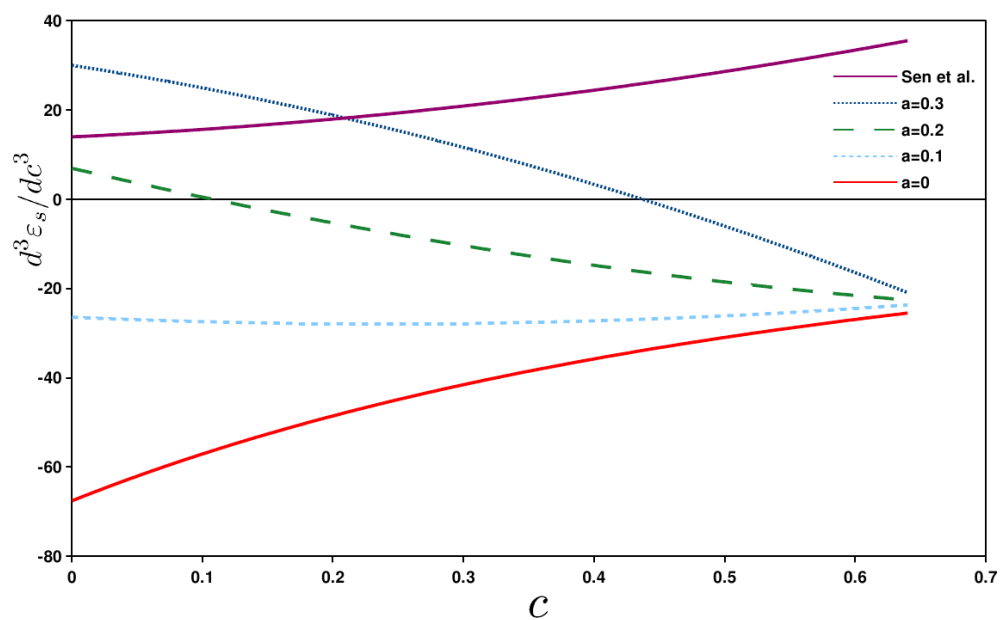


Figure 6.7: Third Derivative of Suspension Permittivity with respect to Volume Fraction vs. Volume Fraction for Silica-DMSO

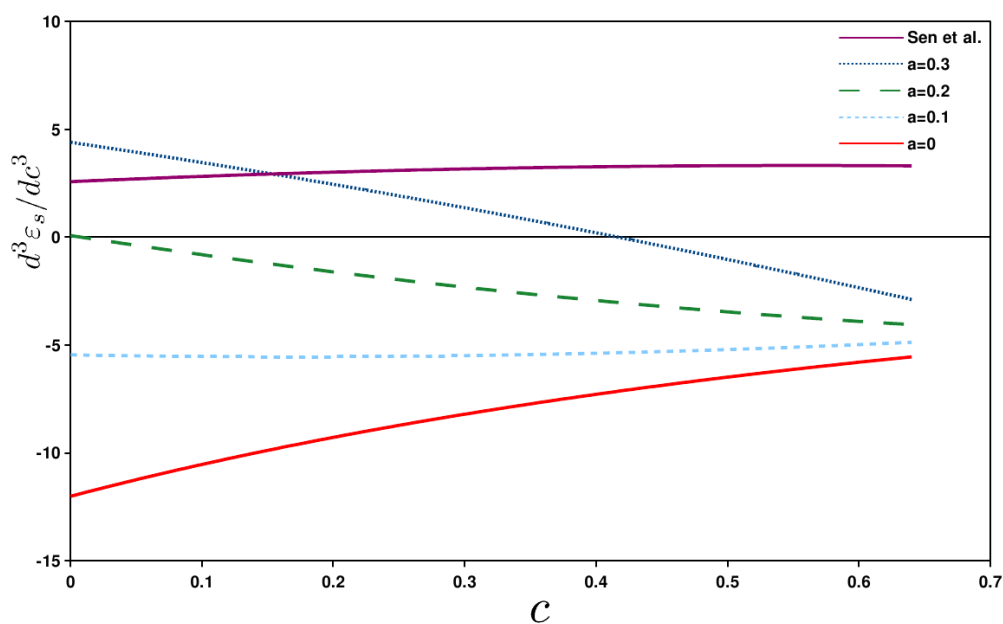


Figure 6.8: Third Derivative of Suspension Permittivity with respect to Volume Fraction vs. Volume Fraction for Silica-iPrOH

to explore the validity of that hypothesis at least in terms of examining the influence on phase transitions. The critical point, c_{cr} and E_{cr} for silica-DMSO and silica-iPrOH suspensions with particle diameters of $0.32\mu\text{m}$ and $2\mu\text{m}$ were determined for each of the permittivity models described previously by solving eqns. 6.10 and 6.11 to determine the inflection point of the spinodal line. The results for each system, permittivity model and particle size are shown in Table 6.1.

	d_p (μm)	$\varepsilon_s(c)$	c_{cr}	E_{cr} (V/m)
Silica-DMSO	0.32	$a = 0$	0.1121	1.59×10^5
		$a = 0.1$	0.1201	1.64×10^5
		$a = 0.2$	0.1299	1.70×10^5
		$a = 0.3$	0.1424	1.78×10^5
		Sen et al.	0.1401	1.89×10^5
	2.00	$a = 0$	0.1121	1.02×10^4
		$a = 0.1$	0.1201	1.05×10^4
		$a = 0.2$	0.1299	1.09×10^4
		$a = 0.3$	0.1424	1.14×10^4
		Sen et al.	0.1401	1.21×10^4
Silica-iPrOH	0.32	$a = 0$	0.1157	3.26×10^5
		$a = 0.1$	0.1217	3.34×10^5
		$a = 0.2$	0.1286	3.44×10^5
		$a = 0.3$	0.1368	3.56×10^5
		Sen et al.	0.1367	3.67×10^5
	2.00	$a = 0$	0.1157	2.09×10^4
		$a = 0.1$	0.1217	2.14×10^4
		$a = 0.2$	0.1286	2.20×10^4
		$a = 0.3$	0.1368	2.28×10^4
		Sen et al.	0.1367	2.35×10^4

Table 6.1: c_{cr} and E_{cr} for Silica-DMSO and Silica-iPrOH

As was expected from the generated permittivity and permittivity derivative data for these systems, there is indeed a large impact of the polarization model on both the critical volume fraction and critical electric field strength. For DMSO the critical volume fraction shifts from 0.1121 to 0.1424 with changing from Maxwell-Garnett to Sihvola-Kong with

$a = 0.3$, with the value for using the permittivity equation of Sen et al. being 0.1401. The critical volume fraction does not change with particle size, which was the case for the previous work of Khusid and Acrivos using the Maxwell-Garnett model (c_{cr} was only a function of β). For isopropanol, the c_{cr} also increases with increasing value of the Sihvola-Kong parameter but the Sen et al. result is much closer to that of $a = 0.3$ compared to the case of DMSO (0.1367 vs. 0.1368). The critical electric field strength increases with increasing value of a while Sen et al. has the largest value for all systems studied. This increase in the electric field strength required for the onset of phase transition is to be expected with accounting for multiscattering effects, as these will lessen the overall interparticle force. The critical field strength at the same particle size is higher for silica-iPrOH versus silica-DMSO, which is also expected as the permittivity of silica-iPrOH is lower than that of silica-DMSO. Of interest is that for $a = 0.3$ and the Sen et al. model, the critical volume fraction is higher for $a = 0.3$ while the critical field strength is higher for Sen et al. This can be explained from examining the second derivatives (Figures 6.5 and 6.6) and third derivatives (Figures 6.7 and 6.8) between these two models. For the second derivatives, the values are positive for both permittivity models and the case of $a = 0.3$ is larger than that of Sen et al. for compositions up to approximately 0.5 (DMSO) and 0.45 (iPrOH). In the case of the third derivative, for Sen et al. the function is positive over the entire composition range and also larger than the value for $a = 0.3$ which starts off as a lower positive value and eventually becomes negative. Since eqn. 6.10 depends on the second derivative of permittivity and eqn. 6.11 depends on both the second and third derivative, the interplay between these values gives rise to the interesting shift in critical volume fraction. The impact is smaller for isopropanol compared to DMSO, as the derivative values for Sen et al. and Sihvola-Kong $a = 0.3$ are closer in that case.

6.3.3 Coexistence and Spinodal Lines for Silica-DMSO and Silica-iPrOH

To continue the study of the influence of composition related polarization effects, the coexistence and spinodal lines for silica-DMSO and silica-iPrOH were constructed for $0.32\mu\text{m}$ and $2\mu\text{m}$ diameter particles. The spinodal line is determined through solution of eqn. 6.10, for electric field intensities ranging from near to the critical field strength (E_{cr}) to field intensities much higher than the critical value. More specifically, the spinodal compositions in the range of dimensionless electric field strength (E/E_{cr}) from 1 to 7 were calculated by solving eqn. 6.10 for each permittivity model. After obtaining these values, the spinodal compositions were used as an initial guess for solving for the coexistence line, eqn. 6.9, at the same range of dimensionless field strengths. The resulting phase diagrams are shown for silica-DMSO in Fig. 6.9, where volume fraction has been normalized against the critical volume fraction (c/c_{cr}). As can be seen from examining this figure, the Maxwell-Garnett polarization model occupies a larger dimensionless space compared with other permittivity models and the spacing between the spinodal and coexistence line is also larger. With increasing values of the Sihvola-Kong parameter, the spinodal and coexistence lines shift to the left and the distance between them decreases. The spinodal and coexistence lines for Sen et al. are to the right of $a = 0.3$, which results from the large difference in critical volume fraction between Sen et al. and $a = 0.3$, where Sen et al. has a lower value, shifting the normalized curve to the right. Additionally, there is a slight kink/discontinuity which arises when the volume fraction becomes higher than 0.5 corresponding to the particle entering the diverging region of compressibility (Z and its derivatives are continuous at $c = 0.5$). For silica-isopropanol, the result is similar but with a few important differences, as seen in Fig. 6.10. Once again, the Maxwell-Garnett model result occupies the largest amount of dimensionless space and this region decreases with increasing values of the Sihvola-Kong parameter. Sen et al. is still to the right of $a = 0.3$ but in this case, the results are much closer together. In particular, the

coexistence lines are virtually overlapping each other. This is due to the critical composition for Sen et al. being virtually identical to that obtained by assuming the suspension follows the Sihvola-Kong model with $a = 0.3$, which as explained previously results from the lower permittivity contrast between silica and isopropanol compared to silica and DMSO.

These results indicate the importance of moving beyond using the Maxwell-Garnett framework and accounting for both concentrated suspension and structural effects on permittivity behavior. However, use of the electrical energy expression that is the basis for calculating the spinodal and coexistence behavior of suspensions in this work (eqn. 6.1) is limited to the case of dielectric colloids in a non-conducting suspension. Extending for conductivity effects would allow for a larger class of suspensions to be treated in this framework, with a wider variety of behavior.

It has been observed for so-called ‘leaky-dielectric’ suspensions, that is for suspensions with both a dielectric and conductive component, that the sign of the 2nd derivative of the real part of permittivity can change as volume fraction increases. This change can actually lead to conducting suspensions to be unable to aggregate under certain conditions [157]. For purely dielectric particles in our work and for the results previously obtained using Maxwell-type polarization, this phenomena is not possible. An extension to account for weak conductivity effects is possible by utilizing the Brillouin equation, which can be derived from macroscopic continuum electrodynamics, but only applies for a weakly lossy material and when the time-variations of the field are of a far longer time scale compared to the relaxation of the suspension. This limits use of the Brillouin equation to weakly conducting suspensions at very low frequencies, $\omega t_s \ll 1$ where t_s is the dielectric relaxation time, although it does reduce to the electrical energy of a non-conducting suspension, eqn. 6.1, if no frequency dependence is assumed. This means the results from this work and from an extension using the Brillouin equation could be potentially combined to use for the very low frequency and high frequency case. Khusid and Acrivos extended their theory to account for conductivity effects using both a statistical mechanics approach based on

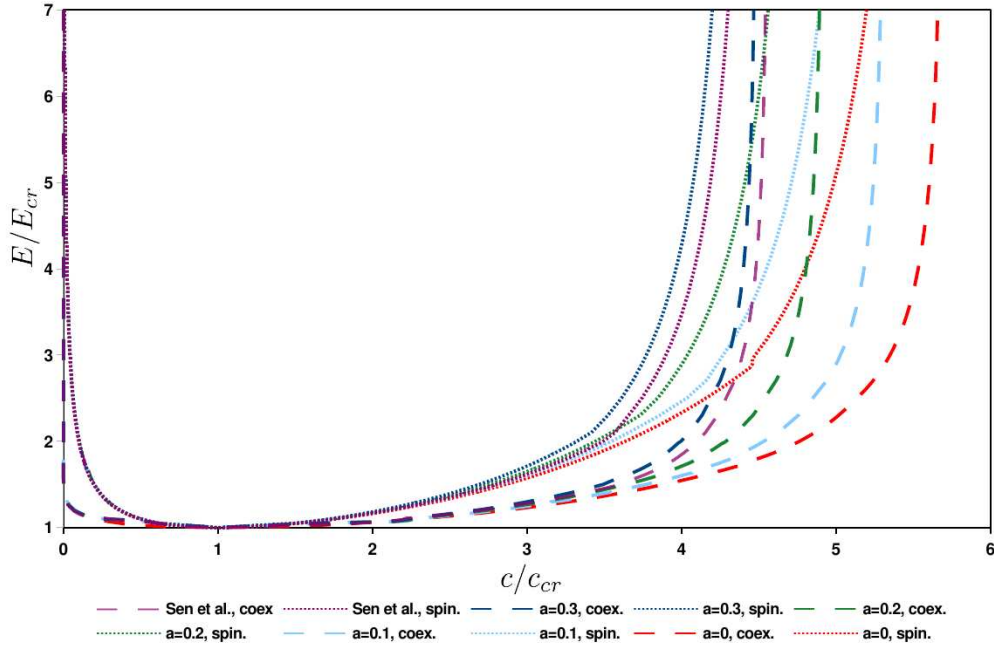


Figure 6.9: Dimensionless Coexistence and Spinodal Lines for Silica-DMSO

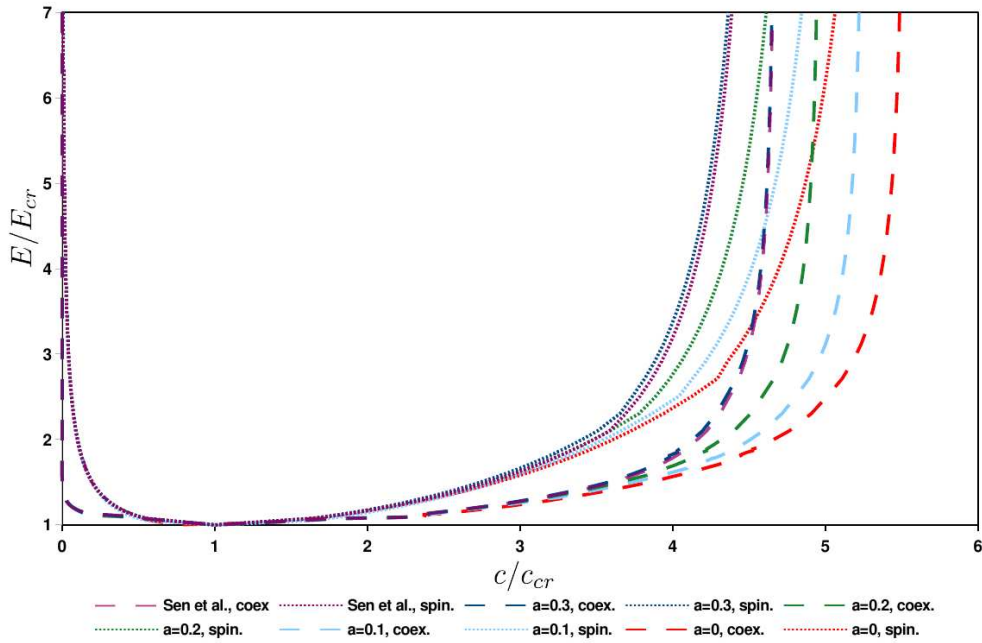


Figure 6.10: Dimensionless Coexistence and Spinodal Lines for Silica-iPrOH

assuming a cell-type model and were able to describe systems over the range of frequency behavior presuming that dielectric and conductive properties for the particle and medium combination are known. However, in the limit of a non-conducting suspension, the equation they derived based on this cell-type approach for electrical energy density yields that of eqn. 6.1 with suspension permittivity described by the Maxwell-Garnett model. From this work, we can conclude that the Maxwell-Garnett approximation yields very different results compared with accounting for multiparticle effects and structural changes in the solid-phase, so finding a way to extend this framework to account for conductivity effects would be quite valuable. Additionally it indicates that use of the Maxwell-Garnett approximation for simulating pattern formation using electric fields, as we have previously done, is limited to situations where the maximum concentration in the system is less than approximately 0.3, which restricts its applicability and usefulness as a quantitative model. Incorporating these expressions in a cell-model framework is not necessarily tractable. However, a similar result to the cell-model was derived by the previous authors using a statistical mechanics approach based on assuming a random microstructure and this may be a more useful approach to using existing permittivity models which have shown good predictive ability for hard sphere suspensions over a wide range of compositions and solid-phase structure types [157].

6.4 Conclusions

Electric-field induced phase transitions of dielectric colloids were predicted using an extension of a thermodynamic framework previously developed by Khusid and Acrivos. This framework treats the free energy of a suspension as having two primary contributions, entropic and electric. Entropic contributions are treated in a hard-sphere manner, with the suspension compressibility assumed to follow the Carnahan-Starling equation of state. Electrical contributions are accounted for using the average electrical energy of a non-conducting suspension from continuum electrodynamics. The influence of multiscattering (volume fraction) effects

on the resulting coexistence and spinodal lines of non-conducting suspensions was examined through use of two effective permittivity models, the Sihvola-Kong formulation and the self-consistent permittivity model of Sen et al. The Sihvola-Kong model is a semi-empirical model which contains an adjustable parameter, a , to account for volume fraction effects on the dipole coefficient allowing the model to shift from the isolated dipole approximation ($a = 0$) while the self-consistent permittivity model of Sen et al. is a predictive model. It has been demonstrated from experimental dielectric (and conductivity) measurements that these models are capable of describing the behavior of mixtures of various solids packing types and lattice structures (RCP, FCC, BCC) over the entire composition region for hard spheres. It has also been shown that the Maxwell-Garnett and Sen et al. model form an upper and lower bound respectively on the suspension permittivity of mixtures undergoing these types of phase transitions, and that a Sihvola-Kong parameter value of 0.2 describes random close packed structures from $0 \leq c < c_{max}$. Use of these models should allow for the influence of nature of the electric-field induced phase transition (lattice type) to also be explored, in terms of shift in coexistence and spinodal lines. Model colloidal systems were considered, that of silica-DMSO and silica-isopropanol, which represent non-conducting suspensions of dielectric particles in the frequency ranges of interest (MHz). The resulting coexistence and spinodal lines for these systems experienced a substantial change upon accounting for multiscattering effects, with DMSO experiencing a more dramatic change versus isopropanol owing to the larger dielectric contrast between silica and DMSO versus silica and isopropanol.

Accounting for multiparticle effects on suspension permittivity causes a significant shift in the behavior of the derivatives of permittivity with respect to volume fraction. This shift leads to large changes in the chemical potential and osmotic pressure, which leads to shifts in the coexistence and spinodal lines and the critical concentration and field strength for electric-field induced phase transitions. More specifically, increasing the value of the Sihvola-Kong parameter from 0 (Maxwell-Garnett model) leads to an increase in the critical concentration and field strength for aggregation, as well as a decrease in the overall region

of coexistence and spinodal transitions. The behavior of the different permittivity models was not completely 1:1 with their respective magnitudes in permittivity, the derivatives of these functions played a large role in determining the magnitude of coexistence and spinodal line shifts. The Sen et al. self-consistent permittivity model was found to predict a positive, monotonically increasing value for $d^3\epsilon_s/dc^3$ while the values obtained when using the Sihvola-Kong model with $a = 0.3$ are monotonically decreasing, starting off positive but becoming negative at higher volume fractions. This leads to the interesting shift in the critical concentration versus critical electric field strength between these two models, where the Sihvola-Kong predicts a higher critical concentration but a lower critical electric field strength. Similarly, $d^2\epsilon_s/dc^2$ is found to be positive and monotonically decreasing when using the Maxwell-Garnett formulation but is positive and monotonically increasing for the Sen et al. model, while it is not necessarily monotonic depending on the choice of Sihvola-Kong parameter. This affects the resulting spinodal lines, determining the boundary between slow and fast aggregation. This framework is not limited to the permittivity models chosen for this work but is generally applicable to use with any effective permittivity model, as long as the suspension is non-conducting. Extension to include conductivity effects along with volume-fraction dependence of permittivity (and conductivity) is desirable as it would be suitable for predicting properties of interest in colloidal phase transition studies, as well as electrorheology work, and this is the subject of ongoing investigations.

Chapter 7: Summary and Future Recommendations

7.1 Summary

Non-uniform electric fields represent a versatile method for assembling structures of various shape, size and order from colloidal particles. With a single microelectrode geometry, a wide range of structures can be generated by changing various parameters such as applied voltage, frequency, particle size, initial solids concentration and even droplet volume. These structures can be close-packed or more ordered colloidal structures and used in various applications, such as photonic materials or templates for forming inverse structures. In this thesis the use of non-uniform electric field forces, specifically dielectrophoresis and electroosmosis, were explored experimentally for creation of structures with a tailored shape, size and order and theoretically for describing the assembly process and resulting phase-transitions.

Three significant contributions to the existing research in this area are detailed:

1. Experimental demonstration of the formation and stabilization of three-dimensional close-packed structures from colloidal silica using non-uniform electric fields.

The use of pluronic F-127, a triblock co-polymer, allowed for preserving large structures ($100+\mu\text{m}$) which shifted in shape significantly with the applied voltage. Pluronic, which is a surfactant, also inhibited formation of structures with any degree of colloidal ordering. It was also found that near-refractive index matching of suspensions encouraged ordered-type structures, as was evident from aligned groups of particle chains visible through optical microscopy. All assemblies showed significant distortion and damage upon medium evaporation, leading to the investigation of various techniques

to maintain structures. Typically used polymers or monomers for immobilizing colloidal crystals, such as PEGMA/PEGDMA or ETPTA, were not effective at preserving the assemblies formed in this work.

2. Demonstration of the importance of electrohydrodynamic flows in colloidal assembly.

The influence of electrohydrodynamic flows on the assembly of colloidal particles into larger structures was demonstrated through the use of numerical simulations. These simulations were carried out in 2d for numerical simplicity and are based on a continuum thermodynamic framework. Electrohydrodynamic flows resulting solely from the presence of a non-uniform electric field, as opposed to resulting from temperature gradients (electrothermal flows) or field action on the electrode double layer (electroosmosis), were shown to be dominant compared to dielectrophoretic forces over a wide range of conditions. This fluid flow effect became more dominant for smaller particles, due to entropic contributions to the resulting fluid flow increasing coupled with a decrease in the magnitude of dielectrophoretic forces. Experimental validation was carried out for a number of model colloidal systems and it was shown that the 2d simulations were only able to provide qualitative predictions of shape even for small droplet volumes. The presence of fluid flows has been noted previously experimentally but had as of yet been unexplained.

3. Demonstration of the impact of multiscattering/multiparticle effects on electric-field induced phase transitions of dielectric colloids.

The same thermodynamic framework previously used for 2d simulations of the assembly process is here modified to account for multiscattering/multiparticle effects on

suspension permittivity and the impact this has on the resulting electric field driven phase transition of colloids. In order to directly make use of the electrical energy density term available from continuum electrodynamics, a dielectric (non-conducting) suspension was considered as a preliminary case. Multiparticle effects were accounted for by examining the use of two continuum permittivity models which have been shown to accurately describe high concentration regions and different types of solid packing structures, the models of Sihvola and Kong and Sen et al., and compared with the isolated dipole result of Maxwell-Garnett type polarization. It was shown that accounting for multiparticle effects had a large impact on the resulting spinodal (fast aggregation/phase change region) and coexistence (slow aggregation/phase change region) lines of the suspension. This result occurred due to shifts in both the permittivity versus solids packing fraction relationship as well as the curvature (derivatives) of this relationship. The results from this work are potentially useful in predictions of the behavior of a number of physical systems, such as electrorheological fluids, and also show that these multiparticle effects should be explored for potential impact on electric-field induced assemblies.

7.2 Future Recommendations

1. Continue to pursue stabilization using epichlorohydrin.

This was the most promising stabilization approach for preserving three-dimensional structures while allowing for ordered-structures to occur found in this work, with preliminary experiments carried out using PMMA-co-AA colloids synthesized by Dr. Niels Smeets. To pursue this methodology will require optimization of the chemistry for functionalization of acrylic acid surface groups, allowing for control the density of these groups, and find a balance between suspension stability and sufficient reactivity

for stabilization. The technique can be used with additional polymeric stabilization as is required.

2. Explore fabrication of microelectrodes on transparent substrates and pursue more advanced microscopy techniques.

The inability to directly visualize particles upon concentration into a assembly represented a significant barrier to this research, compounded by the difficulty in stabilizing assemblies. Fabricating the microelectrodes on a transparent substrate (glass) would allow for use of both transmittance and reflectance modes for conventional optical microscopy setups present in our research group, as well as allow for use of confocal microscopy. The confocal microscopy systems available were not suitable for this work, as they rely on transmitted light and our current substrates are non-transparent silicon/silicon dioxide.

3. Extension of the simulation framework demonstrated in this thesis to three-dimensional systems.

This is a crucial extension for testing the ability of this framework to provide fully predictive models for electric-field driven assembly of structures from colloidal particles. It will also not be a trivial numerical extension, the three-dimensional case has significantly higher tolerance requirements and poorer time-stepping performance. It is likely that a more complicated numerical method compared to the finite element method in Comsol will be required. The use of more advanced finite-difference based techniques, such as operator splitting, or polynomial collocation methods, such as Chebyshev polynomials, is recommended.

4. Extension of the existing phase diagram work to include conducting systems, as well as calculation of the impact of multiscattering effects on particle trajectories.

The results for purely dielectric suspensions indicated a large impact on the resulting phase diagrams (coexistence and spinodal regions) for electric-field induced phase transitions. This result should be extended to include conducting suspensions, either through accounting for weakly conducting suspensions using Brillouin's formula or extension over the entire range of frequencies using a statistical mechanics type approach. Additionally, the impact of accounting for multiscattering effects on the resulting particle concentration trajectories in a non-uniform electric field should be considered. This work has been performed by Khusid and Acrivos (1999) based on the isolated dipole approach, but the result of extending for multiparticle/multiscattering effects should be considered.

Bibliography

- [1] Y. Xia, B. Gates, Y. Yin and Y. Lu (2000). Monodispersed Colloidal Spheres: Old Materials with New Applications. *Advanced Materials*, **12**(10):693–713.
- [2] M. Agrawal, D. Fischer, S. Gupta, N. E. Zafeiropoulos, A. Pich, E. Lidorikis and M. Stamm (2010). Three-Dimensional Colloidal Crystal Arrays Exhibiting Stop Band in Near-Infrared Region. *The Journal of Physical Chemistry C*, **114**(39):16389–16394.
- [3] J. Wang, Y. Zhang, S. Wang, Y. Song and L. Jiang (2011). Bioinspired Colloidal Photonic Crystals with Controllable Wettability. *Accounts of Chemical Research*, **44**(6):405–415.
- [4] T. Kanai, D. Lee, H. C. Shum, R. K. Shah and D. A. Weitz (2010). Gel-immobilized colloidal crystal shell with enhanced thermal sensitivity at photonic wavelengths. *Advanced Materials*, **22**(44):4998–5002.
- [5] G. W. Leung, F. T. Lau, S. L. Leung and W. J. Li (2007). *2nd IEEE International Conference on Nano/Micro Engineered and Molecular Systems*, chapter Formation of Au Colloidal Crystals for Optical Sensing by DEP-Based Nano-Assembly. IEEE.
- [6] J.-H. Shin, J.-H. Kang, W.-M. Jin, J. H. Park, Y.-S. Cho and J. H. Moon (2011). Facile synthesis of TiO₂ inverse opal electrodes for dye-sensitized solar cells. *Langmuir*, **27**(2):856–60.
- [7] I. Jurewicz, P. Worajittiphon, A. A. K. King, P. J. Sellin, J. L. Keddie and A. B. Dalton (2011). Locking Carbon Nanotubes in Confined Lattice Geometries - A Route to Low Percolation in Conducting Composites. *The Journal of Physical Chemistry B*, **115**(20):6395–6400.
- [8] J. Lee, S. Shanbhag and N. A. Kotov (2006). Inverted colloidal crystals as three-dimensional microenvironments for cellular co-cultures. *Journal of Materials Chemistry*, **16**(35):3558–3564.
- [9] P. M. Tessier, O. D. Velev, A. T. Kalambur, J. F. Rabolt, A. M. Lenhoff and E. W. Kaler (2000). Assembly of Gold Nanostructured Films Templated by Colloidal Crystals and Use in Surface-Enhanced Raman Spectroscopy. *Journal of the American Chemical Society*, **122**(39):9554–9555.
- [10] J. Zhang, Z. Sun and B. Yang (2009). Self-assembly of photonic crystals from polymer colloids. *Current Opinion in Colloid & Interface Science*, **14**(2):103–114.
- [11] K. Zahn and G. Maret (1999). Two-dimensional colloidal structures responsive to external fields. *Current Opinion in Colloid & Interface Science*, **4**(1):60–65.

- [12] S. J. Koh (2007). Strategies for Controlled Placement of Nanoscale Building Blocks. *Nanoscale Research Letters*, **2**(11):519–545.
- [13] C. Guo and L. Kaufman (2007). Flow and magnetic field induced collagen alignment. *Biomaterials*, **28**(6):1105–1114.
- [14] S. Gupta, R. G. Alargova, P. K. Kilpatrick and O. D. Velev (2010). On-chip dielectrophoretic coassembly of live cells and particles into responsive biomaterials. *Langmuir*, **26**(5):3441–52.
- [15] M. Sullivan, K. Zhao, C. Harrison, R. H. Austin, M. Megens, A. Hollingsworth, W. B. Russel, Z. Cheng, T. Mason and P. M. Chaikin (2003). Control of colloids with gravity, temperature gradients, and electric fields. *Journal of Physics: Condensed Matter*, **15**(1):S11–S18.
- [16] H. Morgan and N. G. Green (2003). *AC Electrokinetics: Colloids and Nanoparticles*. Research Studies Press Ltd., Williston, VT, USA.
- [17] A. Ramos, H. Morgan, N. G. Green and A. Castellanos (1998). AC electrokinetics: a review of forces in microelectrode structures. *Journal of Physics D: Applied Physics*, **31**(18):2338.
- [18] A. Castellanos, A. Ramos, A. Gonzalez, N. G. Green and H. Morgan (2003). Electrohydrodynamics and dielectrophoresis in microsystems: scaling laws. *Journal of Physics D: Applied Physics*, **36**(20):2584–2597.
- [19] S. O. Lumsdon, E. W. Kaler, J. P. Williams and O. D. Velev (2003). Dielectrophoretic assembly of oriented and switchable two-dimensional photonic crystals. *Applied Physics Letters*, **82**(6):949.
- [20] A. Docoslis and P. Alexandridis (2002). One-, two-, and three-dimensional organization of colloidal particles using nonuniform alternating current electric fields. *Electrophoresis*, **23**(i):2174–2183.
- [21] J. H. Masliyah and S. Bhattacharjee (2006). *Electrokinetic and Colloidal Transport Phenomena*. Wiley Interscience.
- [22] L. Landau, E. Lifshitz and L. Pitaevskii (1984). *Electrodynamics of continuous media*, volume 8 of *Course of Theoretical Physics*. Pergamon Press, Oxford, U.K.; New York, U.S.A., 2nd edition.
- [23] R. B. Bird, W. E. Stewart and E. N. Lightfoot (2002). *Transport Phenomena*. John Wiley and Sons, Toronto, Canada, 2nd edition.

- [24] N. G. Green, A. Ramos and H. Morgan (2000). AC electrokinetics: a survey of sub-micrometre particle dynamics. *Journal of Physics D: Applied Physics*, **33**(6):632.
- [25] T. B. Jones (2005). *Electromechanics of Particles*. Cambridge University Press.
- [26] S. Gatica, M. Cole and D. Velegol (2005). Designing van der waals forces between nanocolloids. *Nano Letters*, **5**(1):169–173.
- [27] C. Rosales and K. M. Lim (2005). Numerical comparison between maxwell stress method and equivalent multipole approach for calculation of the dielectrophoretic force in single-cell traps. *Electrophoresis*, **26**(11):2057–2065.
- [28] T. B. Jones and M. Washizu (1996). Multipolar dielectrophoretic and electrorotation theory. *Journal of Electrostatics*, **37**(1-2):121–134.
- [29] T. Jones (2003). Basic theory of dielectrophoresis and electrorotation. *IEEE Engineering in Medicine and Biology Magazine*, **22**(6):33–42.
- [30] J. Kadaksham, P. Singh and N. Aubry (2005). Dielectrophoresis induced clustering regimes of viable yeast cells. *Electrophoresis*, **26**(19):3738–3744.
- [31] A. T. J. Kadaksham, P. Singh and N. Aubry (2006). Manipulation of particles using dielectrophoresis. *Mechanics Research Communications*, **33**(1):108–122.
- [32] Y. Lin (2006). *Numerical modelling of dielectrophoresis*. Ph.D. thesis, KTH, Stockholm, Sweden.
- [33] A. Gonzalez, A. Ramos, N. G. Green, A. Castellanos and H. Morgan (2000). Fluid flow induced by nonuniform AC electric fields in electrolytes on microelectrodes. II. A linear double-layer analysis. *Phys. Rev. E.*, **61**(4):4019.
- [34] M. Z. Bazant and Y. Ben (2006). Theoretical prediction of fast 3D AC electro-osmotic pumps. *Lab on a Chip*, **6**(11):1455–1461.
- [35] A. Ramos, H. Morgan, N. G. Green and A. Castellanos (1999). Ac electric-field-induced fluid flow in microelectrodes. *Journal of Colloid and Interface Science*, **217**(2):420–422.
- [36] M. Yairi and C. Richter (2007). Massively parallel microfluidic pump. *Sensors and Actuators A: Physical*, **137**(2):350–356.
- [37] J. A. Levitan, S. Devasenathipathy, V. Studer, Y. Ben, T. Thorsen, T. M. Squires and M. Z. Bazant (2005). Experimental observation of induced-charge electro-osmosis around a metal wire in a microchannel. *Colloids and Surfaces A: Physicochemical and Engineering Aspects*, **267**(1-3):122–132.

- [38] S. Debesset, C. Hayden, C. Dalton, J. Eijkel and A. Manz (2004). An ac electroosmotic micropump for circular chromatographic applications. *Lab on a Chip*, **4**(4):396–400.
- [39] W. Russel, D. Saville and W. Schowalter (1992). *Colloidal Dispersions*. Cambridge monographs on mechanics and applied mathematics. Cambridge University Press.
- [40] E. Climent, M. R. Maxey and G. E. Karniadakis (2004). Dynamics of Self-Assembled Chaining in Magnetorheological Fluids. *Langmuir*, **20**(2):507–513.
- [41] C. J. van Oss (2006). *Interfacial Forces in Aqueous Media*. CRC Press, 2nd edition.
- [42] C. J. van Oss, M. K. Chaudhury and R. J. Good (1987). Monopolar surfaces. *Advances in Colloid and Interface Science*, **28**:35–64.
- [43] C. J. van Oss, R. J. Good and M. K. Chaudhury (1988). Additive and nonadditive surface tension components and the interpretation of contact angles. *Langmuir*, **4**(4):884–891.
- [44] C. D. Volpe, D. Maniglio, M. Brugnara, S. Siboni and M. Morra (2004). The solid surface free energy calculation I. In defense of the multicomponent approach. *Journal of Colloid and Interface Science*, **271**(2):434–453.
- [45] P. Chowdiah, D. T. Wasan and D. Gidaspow (1981). Electrokinetic phenomena in the filtration of colloidal particles suspended in nonaqueous media. *AIChE Journal*, **27**(6):975–984.
- [46] A. Kumar, A. Acrivos, B. Khusid and D. Jacqmin (2007). Electric field-driven formation of particle concentration fronts in suspensions. *Fluid Dynamics Research*, **39**(1-3):169–192.
- [47] B. Khusid and A. Acrivos (1995). Effects of conductivity in electric-field-induced aggregation in electrorheological fluids. *Phys. Rev. E*, **52**(2):1669–1693.
- [48] B. Khusid and A. Acrivos (1996). Effect of interparticle electric interactions on dielectrophoresis in colloidal suspensions. *Phys. Rev. E*, **54**(5):5428–5435.
- [49] B. Khusid and A. Acrivos (1999). Phase diagrams of electric-field-induced aggregation in conducting colloidal suspensions. *Phys. Rev. E*, **60**(3):3015–3035.
- [50] T. Hao (2001). Electrorheological fluids. *Advanced Materials*, **13**(24):1847–1857.
- [51] B. T. Mayers, B. Gates and Y. Xia (2000). Crystallization of Mesoscopic Colloids into 3D Opaline Lattices in Packing Cells Fabricated by Replica Molding. *Advanced Materials*, **12**(21):1629–1632.

- [52] A. Fernández-Nieves (2006). Engineering colloids with optical and geometrical anisotropies: de-coupling size monodispersity and particle properties. *Soft Matter*, **2**(2):105–108.
- [53] D. Kuncicky and O. Velez (2008). Surface-guided templating of particle assemblies inside drying sessile droplets. *Langmuir*, **24**(4):1371–1380.
- [54] M. H. Kim, J.-Y. Choi, H. K. Choi, S.-M. Yoon, O. O. Park, D. K. Yi, S. J. Choi and H.-J. Shin (2008). Carbon Nanotube Network Structuring Using Two-Dimensional Colloidal Crystal Templates. *Advanced Materials*, **20**(3):457–461.
- [55] A. Stein and R. Schrodin (2001). Colloidal crystal templating of three-dimensionally ordered macroporous solids: materials for photonics and beyond. *Current Opinion in Solid State & Materials Science*, **5**(6):553–564.
- [56] S. Reculosa, B. Agricola, A. Derré, M. Couzi, E. Sellier, S. Ravaine and P. Delhaès (2006). Carbon Membranes of Controlled Thickness from Colloidal Crystals. *Advanced Materials*, **18**(13):1705–1708.
- [57] J. D. Joannopoulos, R. D. Meade and J. N. Winn (1995). *Photonic Crystals: Molding the Flow of Light*. Princeton University Press.
- [58] Y. A. Vlasov, X.-Z. Bo, J. C. Sturm and D. J. Norris (2001). On-chip natural assembly of silicon photonic bandgap crystals. *Nature*, **414**(6861):289–293.
- [59] G. I. N. Waterhouse and M. R. Waterland (2007). Opal and inverse opal photonic crystals: Fabrication and characterization. *Polyhedron*, **26**(2):356–368.
- [60] C. K. Huang, S. W. Chen and W. C. J. Wei (2006). Processing and property improvement of polymeric composites with added zno nanoparticles through microinjection molding. *Journal of Applied Polymer Science*, **102**(6):6009–6016.
- [61] S. Thian, Y. Tang, J. Fuh, Y. Wong, H. Loh, L. Lu and D. Tee (2006). Formation of Micromoulds via UV Lithography of SU8 Photoresist and Nickel Electrodeposition. *Proceedings of the Institution of Mechanical Engineers Part B- Journal of Engineering Manufacture*, **220**(2):329–333.
- [62] M. Matteucci, F. Perennes, B. Marmiroli, P. Miotti, L. Vaccari, A. Gosparini, A. Turchet and E. Di Fabrizio (2006). Compact micropumping system based on LIGA fabricated microparts. *Microelectronic Engineering*, **83**(4-9):1288–1290.
- [63] S. L. Neale, M. P. MacDonald, K. Dholakia and T. F. Krauss (2005). All-optical control of microfluidic components using form birefringence. *Nature Materials*, **4**(7):530–533.

- [64] N. A. Kotov, Y. Liu, S. Wang, C. Cumming, M. Eghtedari, G. Vargas, M. Motamedi, J. Nichols and J. Cortiella (2004). Inverted colloidal crystals as three-dimensional cell scaffolds. *Langmuir*, **20**(19):7887–7892.
- [65] F. L.-Y. Yuen, G. Zak, S. D. Waldman and A. Docoslis (2008). Morphology of fibroblasts grown on substrates formed by dielectrophoretically aligned carbon nanotubes. *Cytotechnology*, **56**(1):9–17.
- [66] G. Lu, C. Li and G. Shi (2007). Synthesis and Characterization of 3D Dendritic Gold Nanostructures and Their Use as Substrates for Surface-Enhanced Raman Scattering. *Chemistry of Materials*, **19**(14):3433–3440.
- [67] D. M. Kuncicky, B. G. Prevo and O. D. Velev (2006). Controlled assembly of sers substrates templated by colloidal crystal films. *Journal of Materials Chemistry*, **16**(13):1207–1211.
- [68] L. Lu, I. Randjelovic, R. Capek, N. Gaponik, J. Yang, H. Zhang and A. Eychmuller (2005). Controlled Fabrication of Gold-Coated 3D Ordered Colloidal Crystal Films and Their Application in Surface-Enhanced Raman Spectroscopy. *Chemistry of Materials*, **17**(23):5731–5736.
- [69] A. Ramos, H. Morgan, N. G. Green and A. Castellanos (1999). The role of electrohydrodynamic forces in the dielectrophoretic manipulation and separation of particles. *Journal of Electrostatics*, **47**(1-2):71–81.
- [70] N. G. Green, A. Ramos, A. Gonzalez, A. Castellanos and H. Morgan (2001). Electrothermally induced fluid flow on microelectrodes. *Journal of Electrostatics*, **53**(2):71–87.
- [71] O. D. Velev and K. H. Bhatt (2006). On-chip micromanipulation and assembly of colloidal particles by electric fields. *Soft Matter*, **2**(9):738–750.
- [72] K. D. Hermanson, S. O. Lumsdon, J. P. Williams, E. W. Kaler and O. D. Velev (2001). Dielectrophoretic assembly of electrically functional microwires from nanoparticle suspensions. *Science*, **294**(5544):1082–1086.
- [73] J. Tang, B. Gao, H. Geng, O. D. Velev, L. C. Qin and O. Zhou (2003). Assembly of 1d nanostructures into sub-micrometer diameter fibrils with controlled and variable length by dielectrophoresis. *Advanced Materials*, **15**(16):1352–1355.
- [74] S. O. Lumsdon and D. M. Scott (2005). Assembly of Colloidal Particles into Microwires Using an Alternating Electric Field. *Langmuir*, **21**(11):4874–4880.

- [75] S. Evoy, N. DiLello, V. Deshpande, A. Narayanan, H. Liu, M. Riegelman, B. R. Martin, B. Hailer, J. C. Bradley, W. Weiss, T. S. Mayer, Y. Gogotsi, H. H. Bau, T. E. Mallouk and S. Raman (2004). Dielectrophoretic assembly and integration of nanowire devices with functional CMOS operating circuitry. *Microelectronic Engineering*, **75**(1):31–42.
- [76] J. Li, Q. Zhang, D. Yang and J. Tian (2004). Fabrication of carbon nanotube field effect transistors by AC dielectrophoresis method. *Carbon*, **42**(11):2263–2267.
- [77] J. Sun, Z. Guo, C. Wang and N. Gu (2005). Electric Field-Induced Chaining of Au/Aniline Polymeric Particle Pairs and TEM Characterization. *ChemPhysChem*, **6**(12):2485–2488.
- [78] H.-W. Seo, C.-S. Han, D.-G. Choi, K.-S. Kim and Y.-H. Lee (2005). Controlled assembly of single SWNTs bundle using dielectrophoresis. *Microelectronic Engineering*, **81**(1):83–89.
- [79] S. J. Papadakis, Z. Gu and D. H. Gracias (2006). Dielectrophoretic assembly of reversible and irreversible metal nanowire networks and vertically aligned arrays. *Applied Physics Letters*, **88**(23):233118.
- [80] N. Ranjan, H. Vinzelberg and M. Mertig (2006). Growing one-dimensional metallic nanowires by dielectrophoresis. *Small*, **2**(12):1490–1496.
- [81] Y. J. Yuan, M. K. Andrews and B. K. Marlow (2004). Chaining and dendrite formation of gold particles. *Applied Physics Letters*, **85**:130–132.
- [82] R. Barsotti, M. D. Vahey, R. Wartena, Y.-M. Chiang, J. Voldman and F. Stellacci (2007). Assembly of metal nanoparticles into nanogaps. *Small*, **3**(3):488–499.
- [83] M. Dürr, J. Kentsch, T. Müller, T. Schnelle and M. Stelzle (2003). Microdevices for manipulation and accumulation of micro- and nanoparticles by dielectrophoresis. *Electrophoresis*, **24**(4):722–731.
- [84] N. Flores-Rodriguez and G. H. Markx (2006). Flow-through devices for the ac electrokinetic construction of microstructured materials. *Journal of Micromechanics and Microengineering*, **16**(2):349–355.
- [85] S. O. Lumsdon, E. W. Kaler, J. P. Williams and O. D. Velev (2003). Dielectrophoretic assembly of oriented and switchable two-dimensional photonic crystals. *Applied Physics Letters*, **82**(6):949–951.
- [86] S. O. Lumsdon, E. W. Kaler and O. D. Velev (2004). Two-Dimensional Crystallization of Microspheres by a Coplanar AC Electric Field. *Langmuir*, **20**(6):2108–2116.

- [87] A. Docoslis and P. Alexandridis (2002). One-, two-, and three-dimensional organization of colloidal particles using nonuniform alternating current electric fields. *Electrophoresis*, **23**(14):2174–2183.
- [88] A. Docoslis (2007). Removal of pluronic f-105 gel using electron beam. **Personal Communication**.
- [89] T. Clark, J. D. Ruiz, H. Fan, C. J. Brinker, B. I. Swanson and A. N. Parikh (2000). A New Application of UV-Ozone Treatment in the Preparation of Substrate-Supported, Mesoporous Thin Films. *Chemistry of Materials*, **12**(12):3879–3884.
- [90] E. Ozkan, S.-H. Lee, P. Liu, C. E. Tracy, F. Z. Tepehan, J. R. Pitts and S. K. Deb (2002). Electrochromic and optical properties of mesoporous tungsten oxide films. *Solid State Ionics*, **149**(1-2):139–146.
- [91] M. Abe, M. Orita, H. Yamazaki, S. Tsukamoto, Y. Teshima, T. Sakai, T. Ohkubo, N. Momozawa and H. Sakai (2004). Three-dimensional arrangements of polystyrene latex particles with a hyperbolic quadruple electrode system. *Langmuir*, **20**(12):5046–5051.
- [92] N. Khanduja, S. Selvarasah, C.-L. Chen, M. R. Dokmeci, X. Xiong, P. Makaram and A. Busnaina (2007). Three dimensional controlled assembly of gold nanoparticles using a micromachined platform. *Applied Physics Letters*, **90**(8):083105.
- [93] M. Trau, D. A. Saville and I. Aksay (1996). Field-Induced Layering of Colloidal Crystals. *Science*, **272**(5262):706–709.
- [94] M. Trau, D. A. Saville and I. Aksay (1997). Assembly of Colloidal Crystals at Electrode Interfaces. *Langmuir*, **13**(24):6375–6381.
- [95] T. Gong, D. T. Wu and D. W. M. Marr (2003). Electric Field-Reversible Three-Dimensional Colloidal Crystals. *Langmuir*, **19**(15):5967–5970.
- [96] W. D. Ristenpart, I. Aksay and D. A. Saville (2004). Assembly of colloidal aggregates by electrohydrodynamic flow: Kinetic experiments and scaling analysis. *Phys. Rev. E*, **69**(2):21405.
- [97] J. Chung, K.-H. Lee, J. Lee and R. S. Ruoff (2004). Toward Large-Scale Integration of Carbon Nanotubes. *Langmuir*, **20**(8):3011–3017.
- [98] J. A. Wood, B. Zhang, M. R. Tomkins and A. Docoslis (2007). Numerical investigation of AC electrokinetic virus trapping inside high ionic strength media. *Microfluidics and Nanofluidics*, **3**(5):547–560.

- [99] M. Tomkins, J. Wood and A. Docoslis (2008). Observation and analysis of electrokinetically driven particle trapping in planar microelectrode arrays. *Canadian Journal of Chemical Engineering*, **86**(4):609–621.
- [100] M. Sigurdson, D. Wang and C. D. Meinhart (2005). Electrothermal stirring for heterogeneous immunoassays. *Lab on a Chip*, **5**(12):1366–1373.
- [101] A. Rosenthal, B. M. Taff and J. Voldman (2006). Quantitative modeling of dielectrophoretic traps. *Lab on a Chip*, **6**(4):508–515.
- [102] F. Aldaeus, Y. Lin, J. Roeraade and G. Amberg (2005). Superpositioned dielectrophoresis for enhanced trapping efficiency. *Electrophoresis*, **26**(22):4252–4259.
- [103] T. Schnelle, T. Müller, G. Gradl, S. G. Shirley and G. Fuhr (2000). Dielectrophoretic manipulation of suspended submicron particles. *Electrophoresis*, **21**(1):66–73.
- [104] A. T. J. Kadaksham, P. Singh and N. Aubry (2004). Dielectrophoresis of nanoparticles. *Electrophoresis*, **25**(21-22):3625–3632.
- [105] M. Johnson, X. Duan, B. Riley, A. Bhattacharya and W. Luo (2004). Thermodynamic model of electric-field-induced pattern formation in binary dielectric fluids. *Phys. Rev. E.*, **69**(4):41501.
- [106] E. V. L. de Mello and O. Teixeira Da Silveira Filho (2005). Numerical study of the Cahn–Hilliard equation in one, two and three dimensions. *Physica A: Statistical Mechanics and its Applications*, **347**:429–443.
- [107] M. Abe, M. Orita, H. Yamazaki, S. Tsukamoto, Y. Teshima, T. Sakai, T. Ohkubo, N. Momozawa and H. Sakai (2004). Three-Dimensional Arrangements of Polystyrene Latex Particles with a Hyperbolic Quadruple Electrode System. *Langmuir*, **20**(12):5046–5051.
- [108] T. Gong and D. W. M. Marr (2001). Electrically switchable colloidal ordering in confined geometries. *Langmuir*, **17**(23):2301–2304.
- [109] R. Xie and X.-Y. Liu (2008). Electrically Directed On-Chip Reversible Patterning of Two-Dimensional Tunable Colloidal Structures. *Advanced Functional Materials*, **18**(5):802–809.
- [110] S. Gangwal, O. J. Cayre and O. D. Velev (2008). Dielectrophoretic assembly of metallodielectric Janus particles in AC electric fields. *Langmuir*, **24**(23):13312–20.
- [111] S. Kim, R. Asmatulu, H. L. Marcus and F. Papadimitrakopoulos (2011). Dielectrophoretic Assembly of Grain-Boundary-Free 2D Colloidal Single Crystals. *Journal of Colloid and Interface Science*, **354**(2):448–454.

- [112] A. P. Bartlett, A. K. Agarwal and A. Yethiraj (2011). Dynamic templating of colloidal patterns in three dimensions with nonuniform electric fields. *Langmuir*, **27**(8):4313–8.
- [113] O. D. Velev and S. Gupta (2009). Materials Fabricated by Micro- and Nanoparticle Assembly - The Challenging Path from Science to Engineering. *Advanced Materials*, **21**(19):1897–1905.
- [114] P. J. Costanzo, T. E. Patten and T. A. P. Seery (2006). Nanoparticle Agglutination: Acceleration of Aggregation Rates and Broadening of the Analyte Concentration Range Using Mixtures of Various-Sized Nanoparticles. *Langmuir*, **22**(6):2788–2794.
- [115] G. Wei, H. Xu, P. Ding, S. Li and J. Zheng (2002). Thermosetting gels with modulated gelation temperature for ophthalmic use: the rheological and gamma scintigraphic studies. *Journal of Controlled Release*, **83**(1):65–74.
- [116] N. Takahashi, T. Kanaya, K. Nishida and K. Kaji (2003). Effects of cononsolvency on gelation of poly(vinyl alcohol) in mixed solvents of dimethyl sulfoxide and water. *Polymer*, **44**(15):4075–4078.
- [117] N. Takahashi, T. Kanaya, K. Nishida and K. Kaji (2007). Gelation-Induced Phase Separation of Poly(vinyl alcohol) in Mixed Solvents of Dimethyl Sulfoxide and Water. *Macromolecules*, **40**(24):8750–8755.
- [118] N. Ise and I. Sogami (2005). *Structure formation in solution: ionic polymers and colloidal particles*. Springer-Verlag.
- [119] A. Yethiraj, A. Wouterse, B. Groh and A. van Blaaderen (2004). Nature of an Electric-Field-Induced Colloidal Martensitic Transition. *Physical Review Letters*, **92**(5):3–6.
- [120] A. M. Almodallal and I. Saika-Voivod (2011). Simulation of a two-dimensional model for colloids in a uniaxial electric field. *Phys. Rev. E.*, **84**(1):011402.
- [121] K.-Q. Zhang and X. Y. Liu (2009). Controlled formation of colloidal structures by an alternating electric field and its mechanisms. *The Journal of chemical physics*, **130**(18):184901.
- [122] K. von Pfeil, M. D. Graham, D. J. Klingenberg and J. F. Morris (2003). Structure evolution in electrorheological and magnetorheological suspensions from a continuum perspective. *Journal of Applied Physics*, **93**(9):5769.
- [123] M. Hagenbuchle and J. Liu (1997). Chain formation and chain dynamics in a dilute magnetorheological fluid. *Applied optics*, **36**(30):7664–7671.
- [124] L. He, Y. Hu, H. Kim, J. Ge, S. Kwon and Y. Yin (2010). Magnetic assembly of nonmagnetic particles into photonic crystal structures. *Nano letters*, **10**(11):4708–14.

- [125] Y. Nagaoka, H. Morimoto and T. Maekawa (2011). Ordered complex structures formed by paramagnetic particles via self-assembly under an ac/dc combined magnetic field. *Langmuir*, **27**(15):9160–9164.
- [126] K. Caswell, J. Wilson, U. Bunz and C. Murphy (2003). Preferential end-to-end assembly of gold nanorods by biotin-streptavidin connectors. *Journal of the American Chemical Society*, **125**(46):13914–13915.
- [127] M. Malmsten, P. Linse and T. Cosgrove (1992). Adsorption of peo-ppo-peo block copolymers at silica. *Macromolecules*, **25**(9):2474–2481.
- [128] P. P. Lele and E. M. Furst (2009). Assemble-and-stretch method for creating two- and three-dimensional structures of anisotropic particles. *Langmuir*, **25**(16):8875–8.
- [129] S. H. Foulger, P. Jiang, A. C. Lattam, D. W. Smith and J. Ballato (2001). Mechanochromic response of poly(ethylene glycol) methacrylate hydrogel encapsulated crystalline colloidal arrays. *Langmuir*, **17**(19):6023–6026.
- [130] S. H. Foulger, S. Kotha, B. Sweryda-Krawiec, T. W. Baughman, J. M. Ballato, P. Jiang and J. D. W. Smith (2000). Robust polymer colloidal crystal photonic bandgap structures. *Optics Letters*, **25**:1300–1302.
- [131] S. H. Foulger, P. Jiang, Y. Ying, A. C. Lattam, D. W. Smith and J. Ballato (2001). Photonic bandgap composites. *Advanced Materials*, **13**(24):1898–1901.
- [132] S.-H. Kim, S.-J. Jeon, G.-R. Yi, C.-J. Heo, J. H. Choi and S.-M. Yang (2008). Optofluidic assembly of colloidal photonic crystals with controlled sizes, shapes, and structures. *Advanced Materials*, **20**(9):1649–1655.
- [133] N. C. Linn, C.-H. Sun, P. Jiang and B. Jiang (2007). Self-assembled biomimetic antireflection coatings. *Applied Physics Letters*, **91**(10):101108.
- [134] S. Venkatesh, P. Jiang and B. Jiang (2007). Generalized fabrication of two-dimensional non-close-packed colloidal crystals. *Langmuir*, **23**(15):8231–8235.
- [135] J. Masere, F. Stewart, T. Meehan and J. A. Pojman (1999). Period-doubling behavior in frontal polymerization of multifunctional acrylates. *Chaos*, **9**:315–322.
- [136] M. Sullivan, K. Zhao, C. Harrison, R. H. Austin, M. Megens, A. Hollingsworth, W. B. Russel, Z. Cheng, T. Mason and P. M. Chaikin (2003). Control of colloids with gravity, temperature gradients, and electric fields. *Journal of Physics: Condensed Matter*, **15**(1):S11–S18.
- [137] P. D. Hoffman, P. S. Sarangapani and Y. Zhu (2008). Dielectrophoresis and AC-induced assembly in binary colloidal suspensions. *Langmuir*, **24**(21):12164–71.

- [138] X. Huang, J. Zhou, M. Fu, B. Li, Y. Wang, Q. Zhao, Z. Yang, Q. Xie and L. Li (2007). Binary colloidal crystals with a wide range of size ratios via template-assisted electric-field-induced assembly. *Langmuir*, **23**(17):8695–8.
- [139] N. A. Patankar, P. Singh, D. D. Joseph, R. Glowinski and T. W. Pan (2000). A new formulation of the distributed lagrange multiplier/fictitious domain method for particulate flows. *International Journal of Multiphase Flow*, **26**(9):1509–1524.
- [140] T. Schnelle, T. Müller, Gustav-Meyer-Allee, S. Fiedler and G. Fuhr (1999). The influence of higher moments on particle behaviour in dielectrophoretic field cages. *Journal of Electrostatics*, **46**(1):13–28.
- [141] J. J. Juarez, B. G. Liu, J. Cui and M. A. Bevan (2011). kT-Scale Colloidal Interactions in High Frequency Inhomogeneous AC Electric Fields. II. Concentrated Ensembles. *Langmuir*, **27**(15):9219–9226.
- [142] J. J. Juarez, S. E. Feicht and M. A. Bevan (2012). Electric field mediated assembly of three dimensional equilibrium colloidal crystals. *Soft Matter*, **8**:94–103.
- [143] A. Kumar, Z. Qiu, A. Acrivos, B. Khusid and D. Jacqmin (2004). Combined negative dielectrophoresis and phase separation in nondilute suspensions subject to a high-gradient ac electric field. *Phys. Rev. E.*, **69**(2):21402.
- [144] B. Khusid and A. Acrivos (1995). Effects of conductivity in electric-field-induced aggregation in electrorheological fluids. *Phys. Rev. E.*, **52**(2):1669–1693.
- [145] B. Khusid and A. Acrivos (1996). Effects of interparticle electric interactions on dielectrophoresis in colloidal suspensions. *Phys. Rev. E.*, **54**(5):5428–5435.
- [146] A. Kumar, A. Acrivos, B. Khusid and D. Jacqmin (2007). Electric field-driven formation of particle concentration fronts in suspensions. *Fluid Dynamics Research*, **39**(1-3):169–192.
- [147] A. Sihvola and J. Kong (1988). Effective permittivity of dielectric mixtures. *IEEE Transactions on Geoscience and Remote Sensing*, **26**(4):420–429.
- [148] M. K. Gobbert, A. Churchill, G. Wang and T. I. Seidman (2009). Comsol multiphysics for efficient solution of a transient reaction-diffusion system with fast reaction. *Proceedings of the COMSOL Conference*.
- [149] J. Volker and E. Schmeyer (2008). Finite element methods for time-dependent convection–diffusion–reaction equations with small diffusion. *Computer Methods in Applied Mechanics and Engineering*, **198**(3-4):475–494.

- [150] C. van Oss (2006). *Interfacial forces in aqueous media*. Taylor & Francis, 2nd edition.
- [151] A. Docoslis and P. Alexandridis (2002). Optical microscopy movie of the dep of silica in water. <http://www.chemeng.queensu.ca/faculty/docoslis/index.php>.
- [152] A. Yethiraj, J. H. J. Thijssen, A. Wouterse and A. van Blaaderen (2004). Large-area electric-field-induced colloidal single crystals for photonic applications. *Advanced Materials*, **16**(7):596–600.
- [153] G. Li, L. Shi, Q. Ye, W. Zhou and J. Tian (2006). Electric-field-assisted assembly and alignment of polystyrene-b-poly(acrylic acid) micelles. *Colloid & Polymer Science*, **284**(10):1179–1183.
- [154] H. J. Choi and M. S. Jhon (2009). Electrorheology of polymers and nanocomposites. *Soft Matter*, **5**(8):1562–1567.
- [155] Y. M. Shkel and D. J. Klingenberg (1999). A continuum approach to electrorheology. *Journal of Rheology*, **43**(5):1307.
- [156] A. Sanchis, M. Sancho, G. Martínez, J. L. Sebastián and S. M. noz (2004). Interparticle forces in electrorheological fluids: effects of polydispersity and shape. *Colloids and Surfaces A: Physicochemical and Engineering Aspects*, **249**(1-3):119–122.
- [157] B. Khusid and A. Acrivos (1999). Phase diagrams of electric-field-induced aggregation in conducting colloidal suspensions. *Phys. Rev. E*, **60**(3):3015–3035.
- [158] Y. L. Siu, J. T. K. Wan and K. W. Yu (2001). Interparticle force in polydisperse electrorheological fluids : Beyond the dipole approximation. *Computer Physics Communications*, **142**:446–452.
- [159] M. Parthasarathy and D. J. Klingenberg (1996). Electrorheology : mechanisms and models. *Materials Science and Engineering*, **17**:57–103.
- [160] K. Tsuda, Y. Hirose, H. Ogura and Y. Otsubo (2008). Effect of electric fields on the surface profiles of electrorheological suspensions. *Colloids and Surfaces A: Physicochemical and Engineering Aspects*, **324**(1-3):228–233.
- [161] E. McIntyre and F. E. Filisko (2010). Filtration in electrorheological suspensions related to the peclet number. *Journal of Rheology*, **54**(3):591–603.
- [162] A. Kumar, B. Khusid, Z. Qiu and A. Acrivos (2005). New Electric-Field-Driven Mesoscale Phase Transitions in Polarized Suspensions. *Physical Review Letters*, **95**(25):258301.

- [163] Q. Ye, J. Li and H. Wan (2004). The limits of validity for the dipole approximation for a dielectric mixture. *Electromagnetics*, **24**(3):143–152.
- [164] P. Sen, C. Scala and M. Cohen (1981). A self-similar model for sedimentary rocks with application to the dielectric constant of fused glass beads. *Geophysics*, **46**:781–795.
- [165] D. Robinson and S. Friedman (2005). Electrical conductivity and dielectric permittivity of sphere packings: Measurements and modelling of cubic lattices, randomly packed monosize spheres and multi-size mixtures. *Physica A: Statistical Mechanics and its Applications*, **358**(2-4):447–465.
- [166] T. E. Doyle, D. A. Robinson, S. B. Jones, K. H. Warnick and B. L. Carruth (2007). Modeling the permittivity of two-phase media containing monodisperse spheres: Effects of microstructure and multiple scattering. *Phys. Rev. B*, **76**(5):054203.
- [167] E. C. M. Vermolen, A. Kuijk, L. C. Filion, M. Hermes, J. H. J. Thijssen, M. Dijkstra and A. van Blaaderen (2009). Fabrication of large binary colloidal crystals with a nacl structure. *Proceedings of the National Academy of Science*, **106**:16063–16067.
- [168] L. Hua and C. Wanren (2004). Measurement of viscosity and electrical conductivity and a thermodynamic model. *Physics and Chemistry of Liquids*, **42**(2):195–205.
- [169] L. Hatch and W. Fenwick (1966). *Isopropyl alcohol*. Enjay Chemical Company.
- [170] U. Kaatze, C. Neumann and R. Pottel (1984). The static electric permittivity of solutions of organic molecules in dipolar solvents. *Journal of Solution Chemistry*, **13**(5):357–368.
- [171] U. Kaatze (2007). Reference liquids for the calibration of dielectric sensors and measurement instruments. *Measurement Science and Technology*, **18**(4):967–976.
- [172] C. Wohlfarth (2008). *Landolt-Börnstein IV*, chapter 17: Static Dielectric Constants of Pure Liquids and Binary Liquid Mixtures. Springer-Verlag, Berlin Heidelberg.
- [173] W. Zimmerman and B. Hewakandamby (2006). *Multiphysics Modelling with Finite Element Methods*, chapter 2 - Analyzing Evolution Equations by the Finite Element Method. World Scientific Publishing.
- [174] P. O’Neil (1995). *Advanced Engineering Mathematics*. Brooks/Cole Publishing Company, 4th edition.

Appendix A: MATLAB Codes

A.1 Clausius-Mossotti Factor Calculation

```
% values are for water and carbon black currently
%\cite{RamanSpecExplan} can be altered accordingly

% Particle
eps_vacuum = 8.854e-12; % permittivity of a vacuum, F/m
epsSolid = 5; % relative permittivity of particle
sigmaSolid = 1e5; % conductivity of particle, S/m

% Medium
eps0 = 78.4; % permittivity of medium
epsInf = 5.2; % permittivity at infinite frequency
tau = 8.28e-12; % time constant of medium
sigmaMedium = 15.5e-3; % conductivity medium
epsMedium = 78.4; % permittivity of medium

omega=2*pi*logspace(-1,9); % angular frequency

% complex permittivity of solid and medium
epsilonP = epsSolid*eps_vacuum - i*sigmaSolid./omega;
epsilonM = epsInf + (eps0-epsInf)./(1+i*(omega*tau));
epsilonM = epsilonM*eps_vacuum;

% Clausius-Mossotti factor
Ke = (epsilonP-epsilonM)./(epsilonP+2*epsilonM);

% Maxwell-Wagner time constant

tau0 = (epsSolid - epsMedium)*
eps_vacuum/(sigmaSolid - sigmaMedium);

tauMW = (epsSolid + 2*epsMedium)
*eps_vacuum/(sigmaSolid + 2*sigmaMedium);

semilogx(omega,real(Ke),'o-')
```

A.2 Phase Equilibrium Model for Zero Electric Field

```

function phaseEqModel()
clear all;
clc;
T = 298; % temperature, K

% medium parameters
epsilon = 78; % relative permittivity
z = 1; % ion valence

% particle parameters
Zeta = -62*10^-3; % zeta potential, V
dP = 330e-9; % particle diameter, m
conc = logspace(-6,-1); % conc. of ionic species, mol/L
initialPhi = zeros(1,length(conc));
initialD = ones(1,length(conc));
initialq = zeros(1,length(conc));
initialValues = [[initialPhi];[initialD];[initialq]]

options = optimset('MaxIter',10000,'MaxFunEvals',100000)

AnsDisorder = fsolve(@phaseModel,initialValues,options,
conc,epsilon,z,Zeta,dP,T,0.5);
PhiDisorder = AnsDisorder(1,:);

AnsOrder = fsolve(@phaseModel,initialValues,options,
conc,epsilon,z,Zeta,dP,T,0.55);
PhiOrder = AnsOrder(1,:);

semilogx(conc,AnsDisorder(1,:),conc,AnsOrder(1,:));
disp([conc]')

function F = phaseModel(X,conc,epsilon,z,Zeta,dP,T,
LowOrHighFactor)

rP = 1/2*dP; % particle radius
kB = 1.38*10^-23; % Boltzmann constant, J/K
N_A = 6.022*10^23; % Avogadro's number
e = 1.6*10^-19; % charge of an electron, C

```

```

epsilon0 = 8.85*10^-12; % permittivity of a vacuum, F/m
phiS = e*z*Zeta/(kB*T); % dimensionless surface potential
nB = conc*N_A/(1/1000); % number of ions in bulk, #/m^3

phi = X(1,:); % volume fraction
d_HS_dimensionless = X(2,:); % dimensionless hard sphere diameter
q_dimensionless = X(3,:); % dimensionless surface charge

% Debye parameter of particle free suspension
kappa0 = sqrt(e^2/(epsilon*epsilon0*kB*T)*(2*z^2*nB));

% charge of a single, isolated particle in medium
q0 = epsilon*epsilon0*kB*T/(e*z)*kappa0.*(2*sinh(1/2*phiS)
+4./(kappa0*rP)*tanh(1/4*phiS));

kappaSq = e^2/(epsilon*epsilon0*kB*T)*
(2*z^2*nB-3*q_dimensionless.*q0*z/(rP*e))./(1-phi);

% Debye parameter with particle effects
kappa = sqrt(kappaSq);

% alpha factor
alpha = 4*pi*epsilon*epsilon0*Zeta^2*rP^2*kappa.*
exp(2*rP*kappa)/(kB*T);

F(1,:) = kappa.*d_HS_dimensionless*dP -
alpha.*exp(-kappa.*d_HS_dimensionless*dP);
F(2,:) = phi - LowOrHighFactor*(1./d_HS_dimensionless).^3;
F(3,:) = q_dimensionless./q0 - epsilon*epsilon0*kB*T/(e*z)
*kappa.*(2*sinh(1/2*phiS)+4./(kappa*rP)*tanh(1/4*phiS));

```

A.3 Permittivity and Derivative Fits

```
function F = PermPropertyGen()
```

```

epsP = 4.5;
epsF = 78;
M = 200;

```

```

c = linspace(0,0.64,M);
c = transpose(c);
delta_c = c(2)-c(1);
epsSval = zeros(M,1);
epsGuess = epsF;
options = optimset('MaxFunEvals',5000,'MaxIter',5000,
'TolX',1e-7,'TolFun',1e-7);
% a = 0.1;
for i = 1:length(c)
epsSval(i) = fsolve(@(epsSusp) @epsSuspFind(epsSusp,c(i),0.1,epsP,epsF)
,epsGuess,options);
epsGuess = epsSval(i);
end

epsDev = epsSval - epsF;
A = [c c.^2 c.^3 c.^4 c.^5];
Atrans = transpose(A);
Parm_a_point1 = inv(Atrans*A)*Atrans*epsDev

% a = 0.2;
for i = 1:length(c)
epsSval(i) = fsolve(@(epsSusp) @epsSuspFind(epsSusp,c(i),0.2,epsP,epsF)
,epsGuess,options);
epsGuess = epsSval(i);
end

epsDev = epsSval - epsF;
A = [c c.^2 c.^3 c.^4 c.^5];
Atrans = transpose(A);
Parm_a_point2 = inv(Atrans*A)*Atrans*epsDev

% a = 0.3;
for i = 1:length(c)
epsSval(i) = fsolve(@(epsSusp) @epsSuspFind(epsSusp,c(i),0.3,epsP,epsF)
,epsGuess,options);
epsGuess = epsSval(i);
end

epsDev = epsSval - epsF;
A = [c c.^2 c.^3 c.^4 c.^5];

```

```

Atrans = transpose(A);
Parm_a_point3 = inv(Atrans*A)*Atrans*epsDev

% Sen et al.

for i = 1:length(c)
epsSval(i) = fsolve(@(epsSusp) @epsSuspFindSen(epsSusp,c(i),epsP,epsF)
,epsGuess,options);
epsGuess = epsSval(i);
end

epsDev = epsSval - epsF;
A = [c c.^2 c.^3 c.^4 c.^5];
Atrans = transpose(A);
Parm_Sen = inv(Atrans*A)*Atrans*epsDev

function F = epsSuspFind(epsSusp,c,a,epsP,epsF)
epsA= epsF+a*(epsSusp-epsF);
F_LHS = epsSusp;
F_RHS = epsF
+ 3*c*(epsP-epsF)*(epsA)/(3*epsA+(1-c)*(epsP-epsF));
F = F_LHS-F_RHS;

function F = epsSuspFindSen(epsSusp,c,epsP,epsF)

F = (epsF/epsSusp)^(1/3) - (epsP-epsF)/(epsP-epsSusp)*(1-c);

```

A.4 Coexistence and Spinodal Calculation with Electric Field

```

function phaseEqModel_a_point3()
clc;
% Constants
kB = 1.38e-23; % Boltzmann Constant, J/K
eps0 = 8.85e-12; % Vacuum Permittivity, F/m

% Physical Properties
dP = 2e-6; % diameter, m
T = 293; % Temp, K

```



```

epsF = 46.8; % rel. permittivity DMSO
epsP = 4.5; % rel. permittivity Silica
A = 1.85; % Carnahan-Starling Constant
cMax = 0.64; % Max Packing Fraction
l0 = 100e-6; % Electrode Gap Spacing
Vapplied = [0.5 2.5 5 7.5 10 12.5 15 17.5 20]/sqrt(2); % applied voltages, RMS
p = [epsF -60.53663 15.91887 5.00645 -1.88532 -0.89375];

% Derived Properties
vP = 4/3*pi*(dP/2)^3;
ReKe = (epsP-epsF)/(epsP+2*epsF);
Eapplied = Vapplied/l0;
options = optimset('MaxFunEvals',5000,'MaxIter',5000,
'TolX',1e-7,'TolFun',1e-6);
Parm = fsolve(@(Parm) @crPropCalc(Parm,epsF,eps0,
ReKe,vP,kB,T,cMax,A,p),[1 7],options);
cCr = cMax/2*(tanh(Parm(1))+1)
Ecr = 10^Parm(2)
vPover_kBT = vP/(kB*T);
LambdaCr = vP*Ecr^2/(kB*T)*d2epsdc2(cCr,p);
Eval = [linspace(1.075,2,100) linspace(2.1,7,25)];
E = Ecr*Eval;
lowX_spin = zeros(size(E));
highX_spin = zeros(size(E));
options = optimset('MaxFunEvals',5000,'MaxIter',5000,'TolX',1e-7,'TolFun',1e-6);

Xlow = -5;
Xhigh = 3;
% Spinodal compositions
for i = 1:length(E)
    i
        lowX_spin(i) = fsolve(@(X) @spinodal(X,E(i),epsF,eps0,
ReKe,A,cMax,kB,T,vP,p),Xlow,options);
        highX_spin(i) = fsolve(@(X) @spinodal(X,E(i),epsF,eps0,
ReKe,A,cMax,kB,T,vP,p),Xhigh,options);
        Xlow = lowX_spin(i);
        Xhigh = highX_spin(i);
    end

cLow_spin = cMax/2*(tanh(real(lowX_spin))+1);

```

```

cHigh_spin = cMax/2*(tanh(real(highX_spin))+1);
% Coexistence compositions
cLow_coex = zeros(size(E));
cHigh_coex = zeros(size(E));
options = optimset('MaxFunEvals',5000,'MaxIter',5000,
'TolX',1e-7,'TolFun',1e-6);
lowX_guess = lowX_spin(1);
highX_guess = highX_spin(1);
for i = 1:length(E)
    i
        X_coex = fsolve(@(X) @coexistence(X,E(i),epsF,eps0,
ReKe,A,cMax,kB,T,vP,p),[lowX_guess highX_guess],options);
        cLow_coex(i) = cMax/2*(tanh(real(X_coex(1)))+1);
        cHigh_coex(i) = cMax/2*(tanh(real(X_coex(2)))+1);
        lowX_guess = X_coex(1);
        highX_guess = X_coex(2);
    end
    cLow_coex = fliplr(cLow_coex);
    E_Low = fliplr(E);
    cLow_spin = fliplr(cLow_spin);
    Ecr
    cCr

    c_coex = [cLow_coex cCr cHigh_coex];
    c_spin = [cLow_spin cCr cHigh_spin];
    E_overall = [E_Low Ecr E];
    c_coex = transpose(c_coex);
    c_spin = transpose(c_spin);
    E_overall = transpose(E_overall);
    EoverEcr = E_overall/Ecr;
    c_coexDim = c_coex/0.64;
    c_spinDim = c_spin/0.64;

    disp([EoverEcr c_coexDim c_spinDim ])

    save phaseData_a_point3.mat c_coexDim c_spinDim EoverEcr Ecr cCr

    plot(cCr,Ecr,'ok',cLow_spin,E,'--k',cHigh_spin,
E,'--k',cLow_coex,E,'ok',cHigh_coex,E,'ok')

```

```

function F = coexistence(X,E,epsF,eps0,ReKe,A,cMax,kB,T,vP,p)

cLow = cMax/2*(tanh(real(X(1)))+1);
cHigh = cMax/2*(tanh(real(X(2)))+1);
vPover_kBT = vP/(kB*T);
lambda = 1/2*eps0*epsF*E^2*vPover_kBT;
Zlow = Zfinder(cLow,A,cMax);
Zhigh = Zfinder(cHigh,A,cMax);
df0dc_low = df0dc(cLow);
df0dc_high = df0dc(cHigh);
epsSusp_high = epsSusp(cHigh,p);
epsSusp_low = epsSusp(cLow,p);
depsdc_high = depsdc(cHigh,p);
depsdc_low = depsdc(cLow,p);
mu_int = (depsdc_high-depsdc_low)/epsF;
os_int = ((epsSusp_high-cHigh*depsdc_high)
-(epsSusp_low-cLow*depsdc_low))/epsF;

F(1) = log10(abs(df0dc_high-df0dc_low))-log10(abs(lambda*mu_int));
F(2) = log10(cHigh*Zhigh-cLow*Zlow)-log10(lambda*os_int);

function F = spinodal(X,E,epsF,eps0,ReKe,A,cMax,kB,T,vP,p)

c = cMax/2*(tanh(real(X))+1);
Z = Zfinder(c,A,cMax);
dZdc = dZdcFinder(c,A,cMax);
d2Wdc2 = eps0*d2epsdc2(c,p)*E^2/2;
vPover_kBT = vP/(kB*T);

F = log10(abs(Z+c*dZdc))-log10(abs(c*vPover_kBT*d2Wdc2));

function F = crPropCalc(Parm,epsF,eps0,ReKe,vP,kB,T,cMax,A,p)

c = cMax/2*(tanh(real(Parm(1)))+1);
E = 10^Parm(2);
Z = Zfinder(c,A,cMax);
dZdc = dZdcFinder(c,A,cMax);
d2Zdc2 = d2Zdc2Finder(c,A,cMax);
vPover_kBT = vP/(kB*T);
d2Wdc2 = eps0*d2epsdc2(c,p)*E^2/2;

```

```

d3Wdc3 = eps0*d3epsdc3(c,p)*E^2/2;

F(1) = Z + c*dZdc-c*vPover_kBT*d2Wdc2;
F(2) = 2*dZdc+c*d2Zdc2-vPover_kBT*(d2Wdc2+c*d3Wdc3);

function F = epsSusp(c,p)

F=p(1)+p(2)*c+p(3)*c^2+p(4)*c^3+p(5)*c^4+p(6)*c^5;

function F = depsdc(c,p)

F=p(2)+2*p(3)*c+3*p(4)*c^2+4*p(5)*c^3+5*p(6)*c^4;

function F = d2epsdc2(c,p)

F =2*p(3)+3*2*p(4)*c+4*3*p(5)*c^2+5*4*p(6)*c^3;

function F = d3epsdc3(c,p)

F =3*2*p(4)+4*3*2*p(5)*c+5*4*3*p(6)*c^2;

function F = Zfinder(c,A,cMax)

F = (1+c+c.^2-c.^3)./(1-c).^3.*(c>=0).*(c<0.5)
+A./(cMax-c).*(c>=0.5).*(c<0.64);

function F = dZdcFinder(c,A,cMax)

F = ((1+2*c-3*c.^2)./(1-c).^3+3*(1+c+c.^2-c.^3)./(1-c).^4).*(c>=0).*(c<0.5)
+A./(cMax-c).^2.*(c>=0.5).*(c<0.64);

function F = d2Zdc2Finder(c,A,cMax)

F = ((2-6*c)./(1-c).^3+3*(1+2*c-3*c.^2)./(1-c).^4
+3*(1+2*c-3*c.^2)./(1-c).^4
+12*(1+c+c.^2-c.^3)./(1-c).^5).*(c>=0).*(c<0.5)
+2*A./(cMax-c).^3.*(c>=0.5).*(c<0.64);

function F = df0dc(c)

```

```
df0_lowRange = log((c+1e-13)/exp(1))+1  
-2*c*(3*c-4)/(c-1)^2-3*c^2/(c-1)^2+2*c^2*(3*c-4)/(c-1)^3;  
df0_highRange = log((c+1e-13)/exp(1))+10.932+1.891*log(c+1e-13)  
-2.891*log(16-25*c)+1.891+72.268*c/(16-25*c);  
  
F = df0_lowRange*(c>=0)*(c<0.5)+df0_highRange*(c>=0.5)*(c<0.64);
```

Appendix B: Finite Element Method

The Finite Element Method (FEM) is a powerful numerical technique for solving partial differential equations (PDEs). The basic idea behind FEM is to re-state a given set of differential-algebraic equations (DAEs) from the *strong* form into the *weak* form. The strong form of a set of DAEs is the familiar set of PDEs, called the strong form since variables are required to be continuous and to have continuous derivatives to the order of the equation. The weak form is the integral form of the DAE system, the only requirement is that discontinuities have to be integrable [173].

As an example, consider a stationary PDE in three spatial dimensions on the domain Ω :

$$\nabla \cdot \vec{\Gamma}(u) = F(u) \quad (\text{B.1})$$

Now, converting this equation to the weak form (integral equation). Taking eq. (B.1), multiplying by an arbitrary function v which is defined on Ω we obtain:

$$\int_{\Omega} v \nabla \cdot \vec{\Gamma}(u) dV = \int_{\Omega} v F(u) dV \quad (\text{B.2})$$

Now, applying the divergence theorem¹:

$$\int_{\partial\Omega} v \vec{\Gamma}(u) \cdot \vec{n} dS - \int_{\Omega} \nabla v \cdot \vec{\Gamma}(u) dV = \int_{\Omega} v F(u) dV \quad (\text{B.3})$$

To deal with boundary conditions, depends on the nature of boundary, either Dirichlet or Neumann [173]:

$$u = f \text{ on } \partial\Omega \quad (\text{B.4})$$

¹ $v \nabla \cdot \vec{\Gamma}(u) = \nabla \cdot (v \vec{\Gamma}(u)) - \nabla v \cdot \vec{\Gamma}(u)$ and $\int_{\partial\Omega} (\vec{F} \cdot \vec{n}) dS = \int_{\Omega} (\nabla \cdot \vec{F}) dV$ [23, 174]

$$-\vec{n} \cdot \frac{\partial u}{\partial \vec{n}} = g \text{ on } \partial\Omega \quad (\text{B.5})$$

When a PDE is constrained by eq. (B.5), Neumann BC, the boundary term in eq. (B.3) disappears, making the Neumann boundary condition the natural boundary condition for the weak form. In order to deal with Neumann boundary conditions (which lead to a singular matrix when attempting to solve as there is no unique solution), lagrange multipliers are used to write the boundary integrals as constraints. The overall solution procedure is described below.

First, the function u is decomposed into a series of functions:

$$u = \sum_i u_i \phi_i \quad (\text{B.6})$$

In general, basis functions can be any function defined on the domain Ω . For sines and cosines, the function is approximated by a Fourier series (spectral basis). As an alternative, one could use Chebyshev polynomials and obtain an approximation based on pseudospectral basis functions. For FEM, basis functions are chosen to be local functions, i.e. they are only defined on one volume element, and are generally interpolating polynomials, such as Lagrangian or Hermitian polynomials. This is both the strength and weakness of FEM [173].

The test function, v , is generally chosen to be equivalent to basis functions for u , with this method known as the Galerkin approach ($v_i = \phi_i$). Substituting the expressions for u and v into eq. (B.3) obtains a $(k+1)N$ system of equations for U the vector of unknown u_i , with k being the order of the element interpolating polynomial and N being the number of elements. Linearizing this equation, the following result is arrived at:

$$L(U) = 0 \quad L(U_0) = -\frac{\partial L}{\partial U}(U_0)(U - U_0) \quad (\text{B.7})$$

The value of L at the linearization point U_0 , $L(U_0)$ is referred to as the load vector and the value of the negative Jacobian of L at the linearization point, $-\frac{\partial L}{\partial U}(U_0)$ is called the stiffness matrix, $K(U_0)$. This is the canonical case for FEM, with Neumann BCs. However, this setup gives a singular (non-invertable) stiffness matrix. In order to overcome this Lagrange multipliers are used. Starting from writing the BCs in terms of the basis functions [173]:

$$M(U) = 0 \quad M(U_0) = -\frac{\partial M}{\partial U}(U_0)(U - U_0) \quad (\text{B.8})$$

where $M(U) = 0$ is the system of boundary equations (not necessarily N as not all basis functions contribute to the BCs) and $N = -\frac{\partial M}{\partial U}(U_0)$.

The stiffness matrix equation, eq. (B.7) is then supplemented by adding a vector of unknown Lagrange multipliers, Λ [173]:

$$K(U_0)(U - U_0) + N(U_0)^T \Lambda = L(U_0) \quad (\text{B.9})$$

If eq. (B.8) is satisfied then eq. (B.9) will have a vector of *unique* Lagrange multipliers. This approach can be used to impose any sort of constraint which can be expressed in the weak form.

The following is a methodology for obtaining numerically accurate resolution of the PDEs involved in the simulations of Ch. 5:

1. Draw the system geometry while making use of all available symmetry planes for model reduction. Use of symmetry planes vastly reduces the computational task involved, allowing for a higher mesh resolution to be obtainable in the reduced model.
2. Generate an initial mesh with the highest element density near the areas of highest

flux, i.e. near the electrode edges and the dielectrophoretic trap. The mesh needs to be fairly fine everywhere but in particular these areas.

3. Input the desired physics coefficient terms for the electric field, fluid velocity profile and concentration profile. The work presented in this thesis has shown that although there are large gradients present, the inertial terms in the Navier-Stokes equations are indeed negligible and therefore transient Stokes-flow should be considered. The flow profile is not stationary with time, unlike the nearly static electric field profile and this should be accounted for.
4. Since this is a highly convection dominated PDE system, numerical stabilization is required to achieve physical results as well as to improve time-stepping properties. There are a number of methods available for artificial diffusion/viscosity, but implementation in Comsol is somewhat limited due to limited geometric information about the mesh being available. An $O(h^2)$ isotropic artificial diffusion worked well for stabilizing simulations in the work carried out in this thesis but more advanced numerical techniques will likely be required to extend to three-spatial dimensions and time.
5. Solve for the initial electric field profile (stationary) using the initial concentration (volume fraction) and zero fluid flow. This is a linear, symmetric PDE, as there are no permittivity gradients without concentration gradients. As such, a stationary solver that takes advantage of these symmetries should be employed (ex. PARDISO).
6. Using the calculated initial electric field profile, calculate the initial fluid flow profile. This is also a linear symmetric PDE (Stokes' flow) so a solver which takes advantage of equation symmetries should be utilized.
7. Using the calculated electric field and fluid flow profiles as the initial conditions, along with the initial volume fraction, use a time-stepping algorithm to solve for the desired

time-span. This time-span can be estimated from order of magnitude estimates, experimental observations of the system of interest, or the system can be continuously run until steady-state is achieved. Time-stepping can be a very slow process for these types of systems, the nonlinearities impose the requirement of very fine meshes for resolution but this decreases the size of stable time steps for integration.

8. After achieving the desired steady-state (or whatever time profile is desired), the mesh should be increased in resolution and the process re-run in a loop until the steady-state solution ceases to change from iteration to iteration. Monitoring the solution for changes can be done visually (observe max/min values in a quantity, value of gradients, etc.) or more formally through computing the average deviation profile by storing the solution at each iteration.

The relevant boundary conditions for the system are as follows:

Geometric Symmetry Boundaries $\longrightarrow V = \frac{V_{max} - V_{min}}{2} + V_{min}$, $\vec{n} \cdot [-D\nabla c + \vec{u}c] = 0$ and $\vec{u}_{f,normal} = 0$

Outer Droplet/Well Boundary $\longrightarrow \vec{n} \cdot \vec{E} = 0$, $\vec{n} \cdot [-D\nabla c + \vec{u}c] = 0$, $\vec{u}_f = 0$ and $p = 0$. Placing the pressure at the surface at a reference value of zero is acceptable as this it is a scalar potential value, using a value of zero is superior as a reference compared with atmospheric pressure for the numerical scaling of variables.

Electrode Surface/Edge (3d/2d) $\longrightarrow V = V_{app.}$, only holds when ω is high enough to neglect potential drop across the double layer. Continuity conditions hold for all other variables.